DUAL BAND RESONANT SLOT APERTURE COUPLED MICROSTRIP ANTENNA

FOR 5TH GENERATION USA WIRELESS COMMUNICATION SYSTEMS

by

Colin Raymond Kearley

APPROVED BY SUPERVISORY COMMITTEE:

_____

Dr. Andrew J. Blanchard, Chair

_____

Dr. Rashaunda M. Henderson

_____

Dr. Randall E. Lehmann

_____

Dr. Murat Torlak

To Olivia, my daughter

DUAL BAND RESONANT SLOT APERTURE COUPLED MICROSTIP ANTENNA FOR 5TH GENERATION WIRELESS COMMUNICATION SYSTEMS

by

COLIN RAYMOND KEARLEY, B.S.E.E

THESIS

Presented to the Faculty of

The University of Texas at Dallas

in Partial Fulfillment

of the Requirements

for the Degree of

MASTER OF SCIENCE IN

ELECITRICAL ENGINEERING

THE UNIVERSITY OF TEXAS AT DALLAS

May 2018

ACKNOWLEDGEMENTS

I am obliged to the Allen and Leddy families for their support during this project, and Laura Allen for her encouragement over the course of this journey. I am thankful to my advisor, Dr. Andrew Blanchard, for his guidance and direction. I am grateful to have been his student and to have learned so much in the field of antennas. His positive demeanor is infectious and something I hope to emulate in all I encounter. I am also thankful to Dr. Rashaunda Henderson, Dr. Randall Lehmann, and Dr. Murat Torlak for being on my graduate committee. I am indebted to Olli Raikaa, the head of R&D at Nokia Irving, for allowing pursuit of this research and use of the company simulation tools and test equipment.

April 2018

DUAL BAND RESONANT SLOT APERTURE COUPLED MICROSTRIP ANTENNA FOR 5TH GENERATION USA WIRELESS COMMUNICATION SYSTEMS

Colin Raymond Kearley, MS
The University of Texas at Dallas, 2018

Supervising Professor: Dr. Andrew J. Blanchard

Dual band antennas are an important area of research as global telecommunications companies compete to be the first to deploy fifth generation wireless communication systems. Dual band antennas enable communication in more than one operating band, which leads to reduced manufacturing costs due to the increased economies of scale that occur when one antenna is used in multiple applications.

An aperture coupled microstrip antenna is commonly used in consumer electronic products since it is easy to fabricate and easy to integrate with electronic circuits. In this composition, an investigation has been made into converting an aperture coupled microstrip antenna into a dual band aperture coupled microstrip antenna by etching slots into the radiating patch. Using this approach, an antenna and linear array both operating at 29 GHz and 39 GHz have been designed, simulated, fabricated, and tested.

TABLE OF CONTENTS

LIST OF FIGURES

LIST OF TABLES

CHAPTER 1

INTRODUCTION

Driven by the end user's desire to receive media content over the air as quickly as possible, modern telecommunication companies are constantly exploring new methods to deliver higher and higher data rates. As a result, fifth generation telecommunication systems will be deployed at millimeter wave frequencies where operational bandwidths are several orders of magnitude larger than earlier generations. This is creating a need to develop electronics for mass production at frequencies not yet utilized in consumer applications. The competitive nature of the telecommunications industry demands that products perform well, are low cost, and are very reliable. The microstrip antenna is the preferred method of implementing the required radiator since it meets these requirements.

The goal of this thesis is to investigate the feasibility of implementing a dual band microstrip antenna into the RF hardware of fifth generation Radio Access Points. Dual band antennas enable communication in more than one operating band, which leads to reduced manufacturing costs due to the increased economies of scale that occur when one antenna is utilized in multiple applications.

An aperture coupled microstrip antenna is commonly used in consumer electronics. In this composition, an investigation has been made into converting an aperture coupled microstrip antenna into a dual band aperture coupled microstrip antenna by etching slots into the radiating patch. Using this approach, an antenna and linear array operating at 29 GHz and 39 GHz has been designed, simulated, fabricated, and tested.

This thesis is organized into six chapters. This first chapter gives an overview of this thesis. Chapter two outlines the history and theory behind antennas, aperture fed antennas, resonant slot antennas, and phased arrays. Chapter three presents the design process and associated design calculations; first for a single band aperture fed antenna, secondly for a dual band aperture fed antenna, and then finally for the linear array. In chapter four the results of the electromagnetic simulator used to generate the numerical solution are presented. Chapter five discusses the fabrication process of the antenna and the laboratory measurement results. The sixth chapter closes this work with a summary of key findings and potential future work.

The appendices include the empirical development of a modified equation to calculate patch length, an equation to estimate the upper resonance frequency of the dual band aperture fed antenna, the parametric analysis, and some peripheral data on array patterns.

The simulation tools used in this work are Antenna Magus [1], AWR MO [2], and CST MWS [3]. AWR MO is an acronym for Applied Wave Research Microwave Office and CST MWS is an acronym for Computer Simulation Technology Microwave Suite. The acronyms are frequently used throughout this thesis.

CHAPTER 2

BACKGROUND THEORY

This chapter starts with the basic definition of antennas and the fundamental parameters used to quantify their performance. Next, an overview is given of microstrip patch antennas and the advantages of each type. Then, the theory on the operation of aperture coupled microstrip antenna and dual band resonant slot antenna is presented. The chapter closes with a discussion on antenna arrays.

2.1 Definition of an Antenna

An antenna as defined by the Institute of Electrical and Electronic Engineers (IEEE) is a means for radiating or receiving radio waves. Overall, the impedance of free space is 377 ohms and the antenna is a transformer that interfaces nature with the electronic hardware.

2.1.1 How Antennas Operate

A wire will radiate when there is an acceleration of electric charge. A charge moving with uniform velocity will accelerate if the wire is curved, bent, discontinuous, open, or shorted. Propagation happens because acceleration of the electric charge creates a magnetic field, which then creates an electric field, which then creates a magnetic field. This causal relationship continues out into free space. A static charge will not radiate nor will a charge moving with uniform velocity [4, p. 9].

2.1.2 Field Regions

The fields emanating from an antenna are classified into three regions: the reactive near-field, the radiating near field, and the far field. In the reactive near field, the H-field and E-field are orthogonal and out-of-phase. The reactive fields dominate. In the radiating near field, the H-field and E-field are orthogonal and as the distance from the antenna increase transition from being out-of-phase to being in-phase. The reactive fields no longer dominate. In the radiating far field, the E and H-fields are orthogonal and in-phase. The bulk of antenna analysis is done in the radiating far field since antennas are primarily applied to operate in the far-field region (i.e. long-distance communication). The far field is defined to start at $2*(D^2/\lambda)$, where D is the largest dimension of the antenna [4, p. 31]. The caveat is that D is much larger than a wavelength.

2.2 Fundamental Parameters of Antennas

This section defines the fundamental parameters of antennas, paraphrased in brevity from Balanis [4, pp. 25-80] and presented here for the readers ease of reference. This does not include the section on polarization, which has been paraphrased from Zurcher & Gardiol [5, pp. 121-123].

2.2.1 Radiation Power Density

The Poynting vector is used to describe the power density associated with an electromagnetic wave; it is the cross product of the Electric Field and the Magnetic Field.

Equation 2-1

$$W_{av} = \frac{1}{2}\mathrm{Re}[\mathbf{E} \times \mathbf{H}^*]$$

2.2.2 Radiation Intensity

Radiation intensity is defined (in any given direction) as the power radiated from an antenna per unit solid angle. It is a far-field parameter and mathematically it can be found by multiplying the square of the distance from the antenna by the radiation density (i.e. the average Poynting vector).

Equation 2-2

$$U = r^2 W_{av}$$

2.2.3 Radiation Power

It is useful to know the total power radiated by an antenna. The radiation power is mathematically defined as the surface integral of the radiation intensity over the entire sold angle of 4π.

Equation 2-3

$$P_{rad} = \oiint \boldsymbol{W}_{av} \cdot d\boldsymbol{s} = \int_0^{2\pi} \int_0^{\pi} \hat{\boldsymbol{a}}_r W_{av} \cdot \hat{\boldsymbol{a}}_r r^2 sin\theta d\theta d\varphi = \int_0^{2\pi} \int_0^{\pi} W_{av} r^2 sin\theta d\theta d\varphi$$

2.2.4 Directivity

Directivity is defined as the ratio of the radiation intensity in a given direction from the antenna to the radiation intensity averaged over all directions (i.e. an ideal isotropic radiator). Maximum directivity measures the radiation intensity in the direction of its strongest emission, versus the radiation intensity of an ideal isotropic radiator. Mathematically it is defined as:

Equation 2-4

$$D_o = 4\pi \frac{F(\theta,\varphi)|_{max}}{\int_0^{2\pi} \int_0^{\pi} F(\theta,\varphi)\, sin\theta d\theta d\varphi}$$

2.2.5 Radiation Efficiency

The antenna radiation efficiency is defined as the ratio of the power delivered to the radiation resistance Rr over the power delivered to Rr and R_L. Mathematically it is defined as:

Equation 2-5

$$e_{cd} = \frac{R_r}{R_r + R_L}$$

Where …

- R_r = radiation resistance of the antenna
- R_L = loss resistance of the antenna

2.2.6 Gain

The gain of an antenna is defined as the ratio of the radiation intensity, in any given direction, to the radiation intensity that would be obtained if the power accepted by the antenna were radiated isotopically. Antenna gain is not amplification since an antenna is a passive device. Mathematically it is defined as the product of the radiation efficiency and the directivity.

Equation 2-6

$$G_o = e_{cd} D_o = e_{cd}(dB) + D_o(dB)$$

2.2.7 Polarization Patterns

Any electric field radiating form an antenna can be decomposed into two linear components. Depending on the nature of the linear components, the polarization of the antenna can be classified as elliptical, circular, or linear.

When the two linear components are not in phase, the vector sum rotates around the direction of propagation and this is known as elliptical polarization. The rotation can either be clockwise or counter clockwise (as seen by the observer).

When the two linear components are out of phase by 90 degrees, the ellipse becomes a circle and this is known as circular polarization. Again, there is either clockwise rotation (right hand) or counter clockwise rotation (left hand). Implementing circular polarization typically drops the antenna gain by 3 dB.

When the two linear components are in phase, the ellipse becomes a straight line and this is known as linear polarization. There is no rotation in the case of linear polarization. Cross-polarization is a measure of the ratio (in dB) between the wanted signal and an unwanted signal, where the unwanted signal is orthogonal to the wanted signal.

2.2.8 Beam Width & Frequency Response

The half power beam width of an antenna is a measure of the angular separation between the -3 dB points (relative to maximum power) on either side of the main lobe. Frequency response is the characterization of how the half power beam width of the antenna changes over frequency. The half power beam width will be greatest at the center frequency of operation.

2.2.9 VSWR and Return Loss

VSWR is the maximum to minimum ratio of the standing wave in the transmission line and is calculated as follows (where R_r is the radiation resistance and depends on antenna type):

Equation 2-7

$$VSWR = \frac{1 + |\Gamma|}{1 - |\Gamma|} \ldots where \ldots \Gamma = \frac{R_{in} - Z_o}{R_{in} + Z_o} \ldots and \ldots R_{in} = \frac{R_r}{sin^2\left(\frac{kl}{2}\right)}$$

Return loss is the loss of power due to a mismatch. A good antenna will have better than 14 dB return loss over the operating bandwidth. It is calculated as follows:

Equation 2-8

$$RL = Reflected\ Power\ (\%) = 100 * |\Gamma|^2$$

Equation 2-9

$$RL = Reflected\ Power\ (dB) = 10 * log(|\Gamma|^2) = 20 * log(|\Gamma|)$$

2.2.10 Sidelobe Suppression, Front to Back Ratio, and Nulls

Figure 2-1 illustrates the meaning of main lobe, side lobe, back lobe, and nulls. Sidelobe suppression is the difference, in dB, between the main lobe and the largest sidelobe (12.5 dB in the diagram below). Front to back ratio is the difference, in dB, between the main lobe and the back lobe.

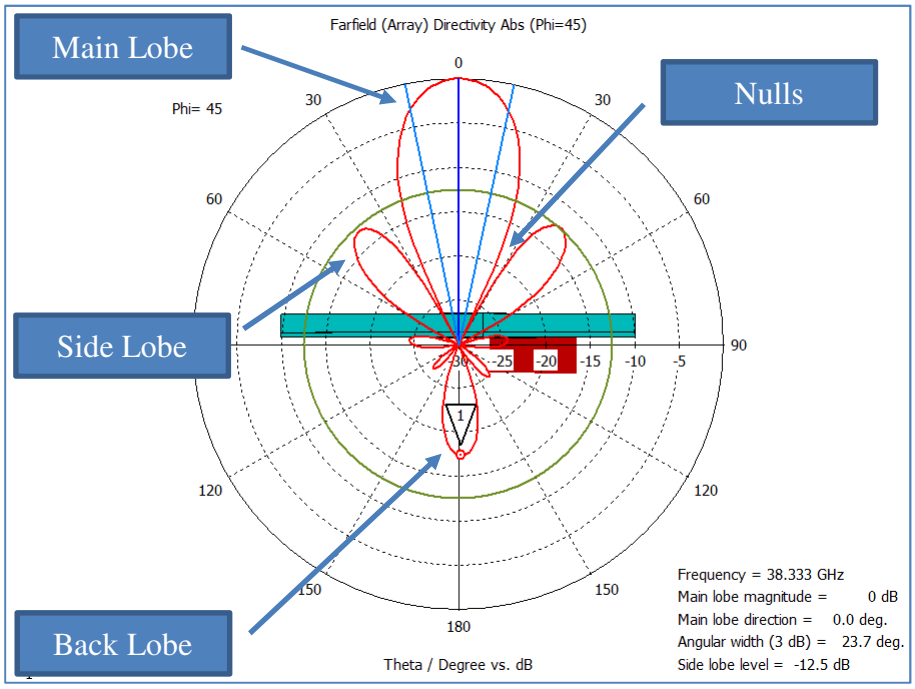

Figure 2-1: Defining Main Lobe, Side Lobe, Back Lobe and Nulls

2.3 Microstrip Antennas

Jennifer Bernhard, currently Associate Dean for Research for the College of Computer Engineering at the University of Illinois, has produced a paper on the history of microstrip antennas [6]. In her paper she points out that Dechamps is commonly given credit for inventing the microstrip antenna in 1953; although the work was a collaborative effort between Dechamps and Sichak [7]. Bancroft [8, p. 3] states microstrip antennas didn't gain traction until the 1970's, when papers released by Howel [9] and Munson [10] presented easily understood equations and useful rules of thumb that enabled wide spread application of the radiator.

2.3.1 Typical Microstrip Antenna Shapes

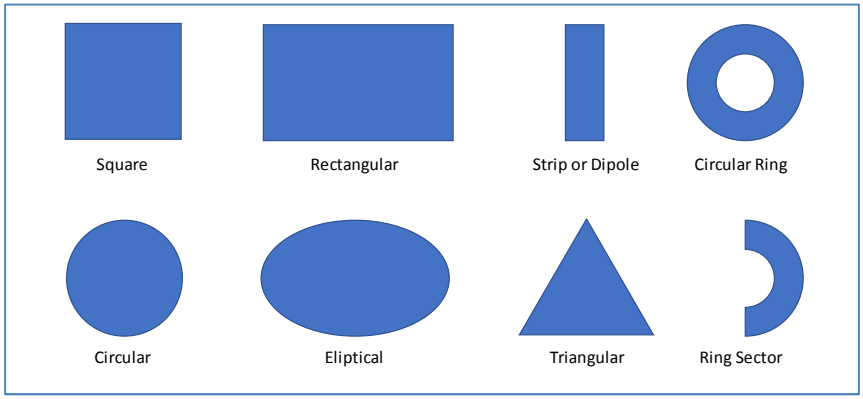

Figure 2-2: Typical Microstrip Antenna Shapes. Adapted, with permission, from Antenna Theory: Analysis and Design, John Wiley & Sons [4]

Patch antenna are typically designed using a basic geometric shape, such as a circle, square, rectangle, or strip, that is easy to both analyze and fabricate [4, p. 785]. Recently seemingly arbitrary shapes have been generated by genetic algorithms that maximize impedance

bandwidth [11]. Overall, any shape can be used so long as it generates the desired characteristics of the specified antenna.

2.3.2 Feeding Mechanisms

The most common mechanisms used to feed a patch antenna are microstrip, probe, proximity coupled, and aperture coupled; all of which are illustrated in Figure 2-3.

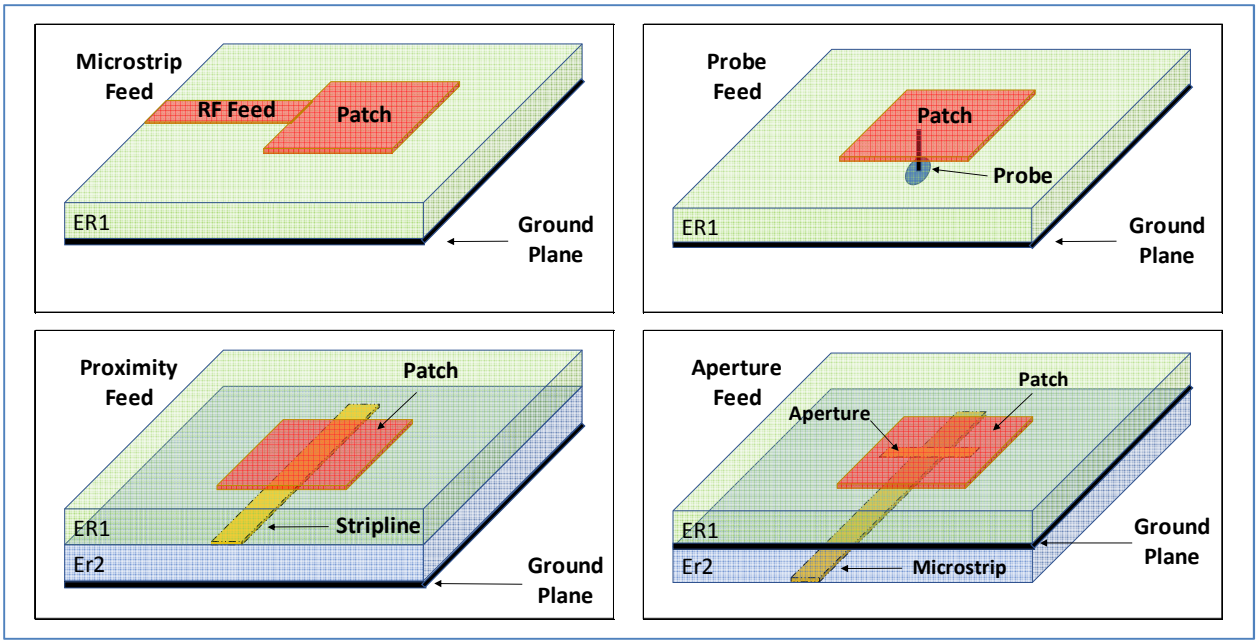

Figure 2-3: Microstrip Patch Feeding Mechanisms. Adapted, with permission, from Antenna Theory: Analysis and Design, John Wiley & Sons [4]

Advantages of the microstrip and probe feeds include ease of fabrication and impedance matching; however, unwanted spurious radiation and surface waves limit the thickness of the substrate which consequently limits the operational bandwidth to less than 5%. The microstrip feed is relatively easy to model whereas the probe feed is more challenging. Both have relatively poor cross-polarization radiation [4, p. 786].

Advantages of proximity coupling and aperture coupling include ease of matching, low spurious radiation (since the RF feed is either buried as a strip line or on the backside of the antenna and separated from the radiating patch by a ground plane), good cross polarization, and large bandwidth; however, they can be more difficult to model and fabricate since alignment is required between feed and patch [4, p. 787].

2.3.3 Fringing Fields

The electric fields fringe at the edges of the patch, along the length and the width. The magnitude of the fringing depends on substrate thickness, substrate dielectric constant, and the dimensions of the patch. Fringing makes the patch larger electrically than it is physically. This impacts resonance and must be considered when determining radiator dimensions [4, p. 790].

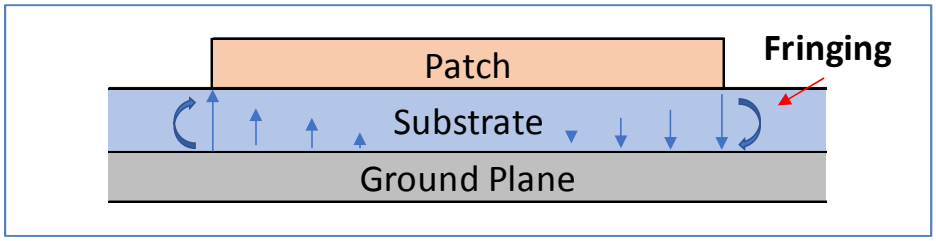

Figure 2-4: Fringing Fields. Adapted, with permission, from Antenna Theory: Analysis and Design, John Wiley & Sons [4]

2.4 Aperture Coupled Microstrip Antenna

David Pozar, currently Professor Emeritus in the Electrical and Computer Engineering department at the University of Massachusetts, first introduced a microstrip antenna coupled to an RF feed through a circular aperture in 1985 [12]. Shortly thereafter Sullivan and Schaubert released a paper which illustrated a microstrip antenna coupled to an RF feed through a

rectangular aperture [13]. Pozar succinctly summarized the history and theory of aperture coupled microstrip antennas in his 1996 paper [14]. It is an often-cited paper and a good starting point for those wanting to learn about the operation of aperture fed antennas.

2.4.1 Basic Structure

An exploded view of an aperture coupled patch antenna is given below. An RF feed couples to the patch through the rectangular aperture, which is etched into the ground plane and centered beneath the patch. There is an upper and lower substrate which may or may not consist of the same material [13].

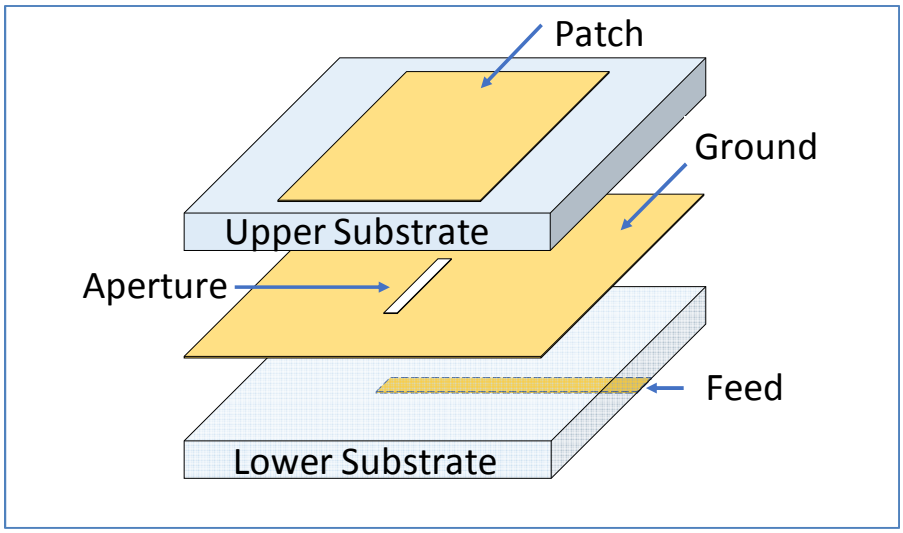

Figure 2-5: Exploded View Aperture Antenna. © 1986 IEEE

2.4.2 Principles of Operation

The aperture fed antenna has several knobs that can be used to dial-in any given desired resonance. The size of the patch primarily determines the resonant frequency. The length of the slot primarily controls the real part of the input impedance. The length of the stub primarily

controls the imaginary part of the input impedance. The thickness of the substrate primarily determines the bandwidth. To a certain extent all four knobs impact each other, and none of the parameters (resonant frequency, input impedance, and bandwidth) are controlled independently. Regardless, almost any resonance can be brought to dead center of the Smith chart. Overall, the antenna has over a dozen parameters. The impact of each parameter has been well articulated by Pozar, and the following paragraphs in this section are paraphrased from this work [14].

The upper substrate thickness impacts bandwidth and coupling. The thicker the substrate, the wider the bandwidth and the lower the coupling. The dielectric constant impacts bandwidth and radiation efficiency. The lower the D_k, the greater the bandwidth and higher the efficiency.

The length of the microstrip patch determines the frequency of resonance. The shorter the length, the higher the resonant frequency. The width of the microstrip patch determines the real part of the impedance. The narrower the patch, the higher the resistance.

The center of the microstrip patch is aligned with the center of the aperture. Moving the patch away from the aperture, along the axis of the feed, lowers coupling and impacts the input impedance. Moving the patch away from the aperture, orthogonal to the axis of the feed, has little impact to coupling and the associated input impedance.

The lower substrate thickness impacts path loss, spurious radiation, and width of the feed. The thicker the substrate, the lower the path loss, the higher the spurious radiation, and the wider the feed. The dielectric constant impacts the width of the feed. The lower the D_k, the wider the feed. This is an important consideration at millimeter wave frequencies where it is possible to specify a feed line that cannot be manufactured due to etching tolerances.

The length of the aperture impacts the real part of the input impedance and the back-radiation levels. The larger the length, the higher the resistance and the larger the level of back-radiation. The width of the aperture also impacts the real part of the input impedance, but to a much smaller extent than the length of the aperture. The ratio of width to length is typically between 1/10 to 1/100; however, at millimeter wave frequencies etching tolerances prohibit ratios above 1/10.

The width of the feed line determines its characteristic impedance and impacts the coupling to the slot. The wider the feed line, the lower the characteristic impedance and the lower the coupling to the slot.

The feed line is aligned with the center of the aperture and orthogonal to the axis of the aperture. If the feed line is either offset or rotated from the center of the aperture, then coupling will be lower.

The tuning stub is inductive and is used to cancel out the capacitance of the aperture coupled antenna. The longer the stub, the greater the inductance. The length of the stub is typically $1/5$ to $1/4$ of wavelength in the respective dielectric.

2.5 Dual Band Resonant Slot Microstrip Antenna

A dual frequency patch antenna using resonant slots and fed by an aperture was first introduced by Maci et all [15] using TM_{10} excitation. In their research it was shown that the radiation patterns of both frequencies held characteristics identical to that of a typical patch antenna, with no apparent broad side nulls or grading lobes. Shortly thereafter, Yazidi et all [16], introduced an aperture fed antenna with resonant slots and showed that that a smaller lower to

upper resonance ration can be achieve using TM_{01} excitation. In addition, their work outlined how the slot length and slot position are important parameters for reducing the ratio between the upper and lower frequencies.

2.5.1 Basic Structure

Figure 2-6, which has been adapted by permission of the IET [16], gives the exploded view of the dual band antenna. Resonant slots are etched into the rectangular patch near the radiating edge and parallel to the aperture in the ground plane.

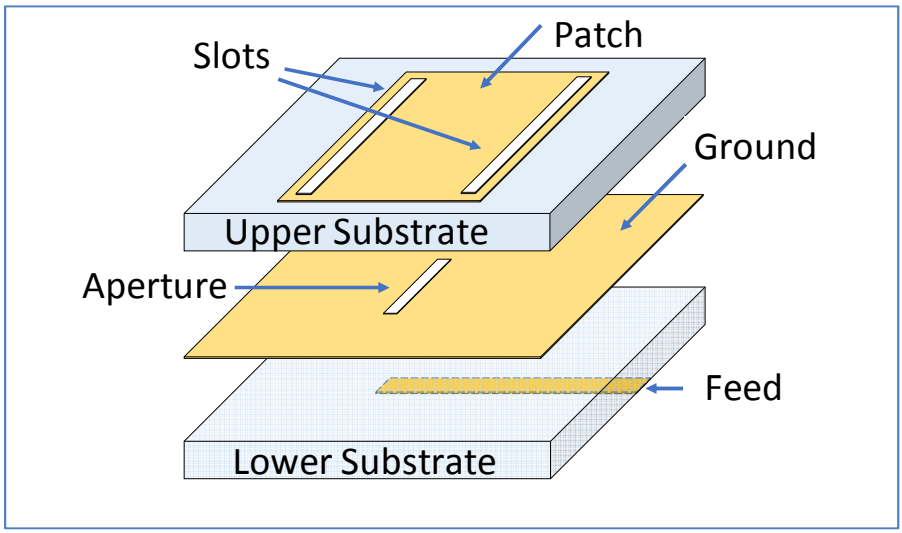

Figure 2-6: Exploded View of Dual Band Antenna

2.5.2 Principles of Operation

The operation of the antenna can be understood through microwave cavity theory. Figure 2-7 illustrates the field configurations for the 1st and 3rd order resonant modes in a rectangular cavity where the width is larger than the length [4, p. 804]. When drawing a comparison to a

microstrip antenna then consider the patch as the top of the cavity, the ground plane as the bottom of the cavity, and the dielectric substrate as the material within the cavity.

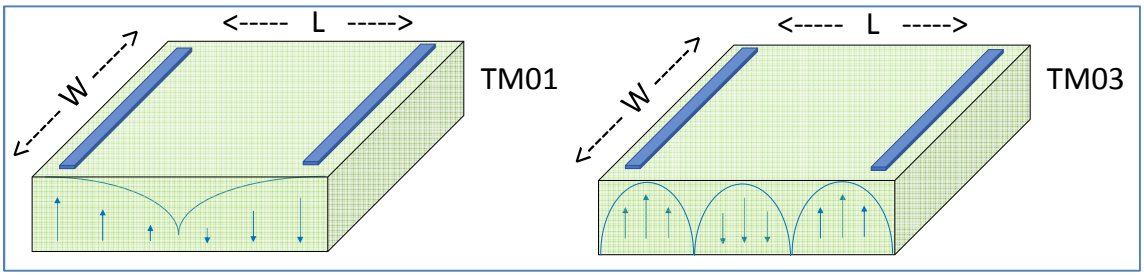

Figure 2-7: Electric Field Configurations (W > L). Adapted, with permission, from Antenna Theory: Analysis and Design, John Wiley & Sons [4]

Since current flow is at a maximum when the electric field is at a minimum, then the slots are etched near the radiating edge which is a location that substantially perturbs the radiation pattern of the 3rd order mode while having only a minor impact on the radiation pattern of the 1st order mode [17].

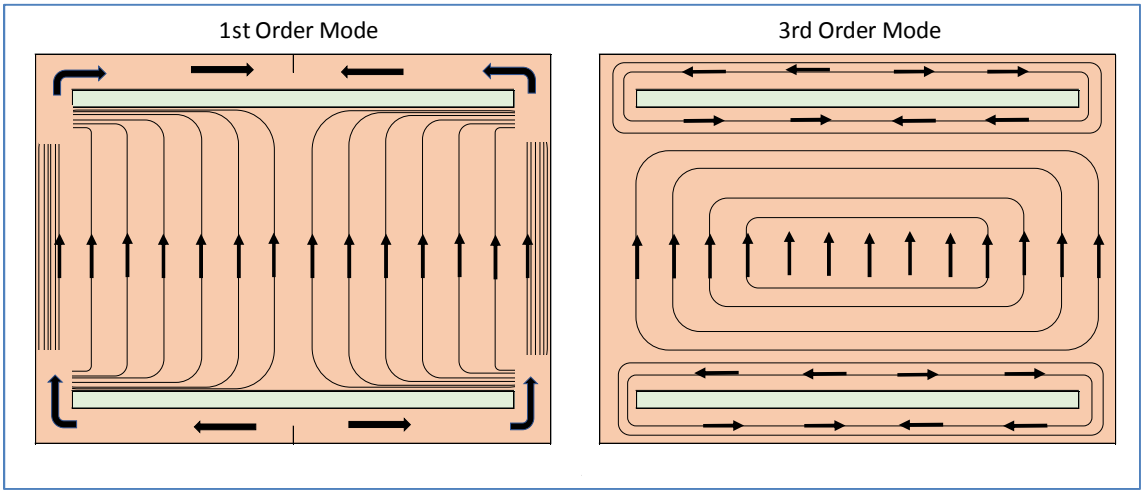

Figure 2-8: Current Flow on Slotted Patch

Figure 2-8, which has been adapted by permission of the IET [17], illustrates the current flow after implementation of the resonant slots. The current flow of the 1st order mode is largely

unchanged, especially in the region which has the weakest electric field. However, the current flow of the 3rd order mode has changed substantially, especially in the region which has weakest electric field. The associated radiation pattern is reminiscent of the 1st order mode of a dipole antenna, rendering it useful since it no longer has the 3-lobe shape associated with 3rd order mode.

Figure 2-9, which has been adapted by permission of the IET [17], illustrates how implementation of the slots impact the resonant frequencies; there is a minor shift in the resonant frequency of the 1st order mode and a substantial shift in resonant frequency of the 3rd order mode. Both the 1st and 3rd order resonant frequencies are dependent on both the size of patch and the size of the resonant slot.

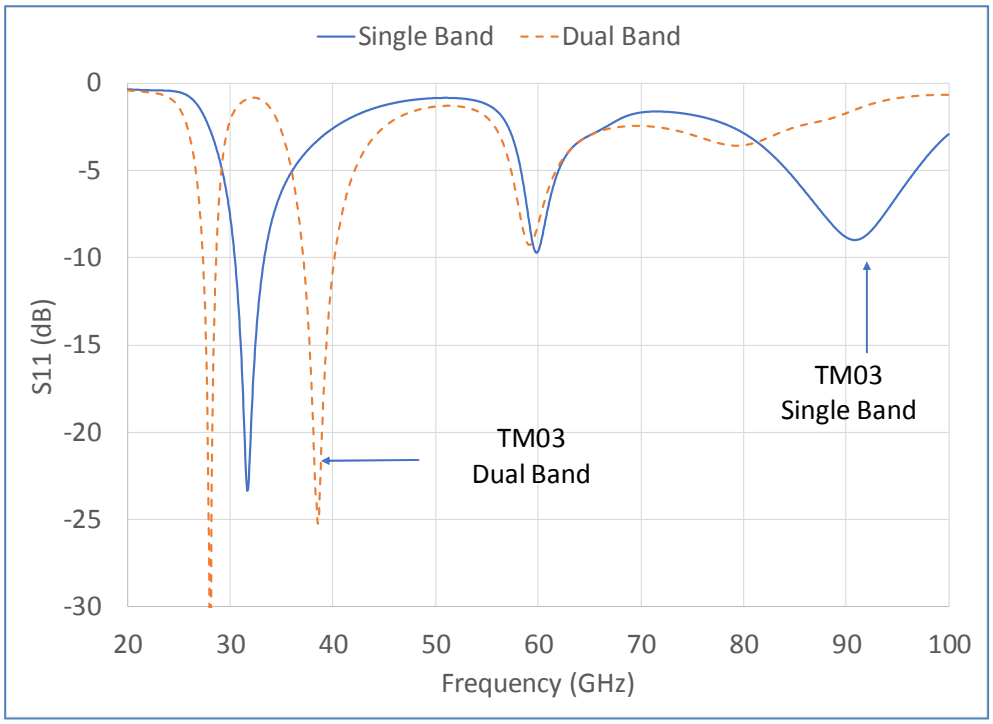

Figure 2-9: Frequency Shift Caused by Resonant Slots

2.6 Antenna Arrays

An antenna array is a grouping of antenna elements into a geometrical pattern that produces a cumulative radiation pattern that is more useful than the radiation pattern of the single element. The antenna elements can be patches, horns, wire dipoles, or anything that radiates. In general, the antenna elements are all the same, although that need not be the case. As the number of antenna elements within the array increases, the cumulative radiation pattern becomes narrower and more directive. Consequently, antenna arrays are useful for long distance communication systems [4, p. 285].

2.6.1 Basic Structure

Arrays are classified as linear (one-dimensional) or planar (two-dimensional). Broadside radiation is perpendicular to the plane of the patch antenna whereas end-fire radiation is directed along the axis of the array. Linear arrays can radiate the main beam in either broadside, end-fire, or anywhere in between. Planar arrays can radiate the main beam to any point in space. The radiation pattern of an array is a function of the radiation pattern of the element in conjunction with the Array Factor. The Array Factor is a function of the number of elements, the spacing of the elements, and the amplitude and phase of the signal at each element.

Both linear and planar arrays can be classified as uniform (in amplitude and spacing) or nonuniform (in either amplitude or spacing). For a uniform array the theoretical worst-case suppression of the first major lobe is – 13.4 dB. For a nonuniform array better suppression can be achieved since the purpose of driving the elements with unequal amplitude, or spacing them with unequal distance, is to minimize sidelobes. Driving the elements of an array with unequal

amplitude is referred to as tapering. The most well know methods of tapering are Tschebyscheff and binomial.

2.6.2 Principles of Operation

Increasing the number of elements in an array increases the directivity, with the trade-off being more and larger sidelobes. Spacing the elements farther apart generates higher directivity; however, the element spacing is typically kept smaller than half a wavelength to avoid the occurrence of grating lobes [18].

Bevalacqua, when he was a student of Balanis at Arizona State University, published a dissertation on the optimization of antenna arrays. He shows that with proper spacing and amplitude tapering a sidelobe suppression of 18 dB can be achieved for an ultrawideband array Bevalazqua concludes that the hexagonal array is a best starting point for an array geometry [19].

CHAPTER 3

DESIGN CALCULATIONS

This chapter presents the design procedure and calculations for the single band aperture fed antenna, the dual band aperture fed antenna, the theoretical checkered array, the theoretical 4x1 linear array, and the 4x1 RF feed network.

3.1 Design Goals

The design goals of the dual band antenna are presented in Table 3-1.

Table 3-1: Design Goals

Parameter	Specification
VSWR	< 2
Input impedance	50 ohms
Lower Frequency Band	27.5 GHz to 28.35 GHz
Upper Frequency Band	37.0 GHz to 40.0 GHz
Antenna Polarization	Linear
Antenna Element Gain	> 5 dBi
Efficiency	> 80%
Sidelobes	~ - 13 dB (no tapering)

Using a thicker the substrate causes the microstrip antenna to have a larger bandwidth. With the pin fed patch antenna, the inductance associated with the feeding pin limits the thickness of the substrate. Consequently, the aperture fed patch antenna was chosen over the pin fed patch antenna since it is possible to achieve a broader bandwidth.

3.2 Aperture Fed Microstrip Patch Antenna

3.2.1 Choice of Resonant Frequency

The aperture coupled patch antenna was initially designed to resonate at the center of the lower band. It was subsequently observed that implementation of the slots into the patch not only established an upper resonance but also shifted the lower resonance down in frequency by roughly 12% (APPENDIX B). The aperture coupled patch antenna was ultimately designed to resonate at roughly 31.8 GHz with the understanding the subsequent implementation of the slots would shift the lower resonance to roughly 27.9 GHz.

3.2.2 Choice of Resonating Mode

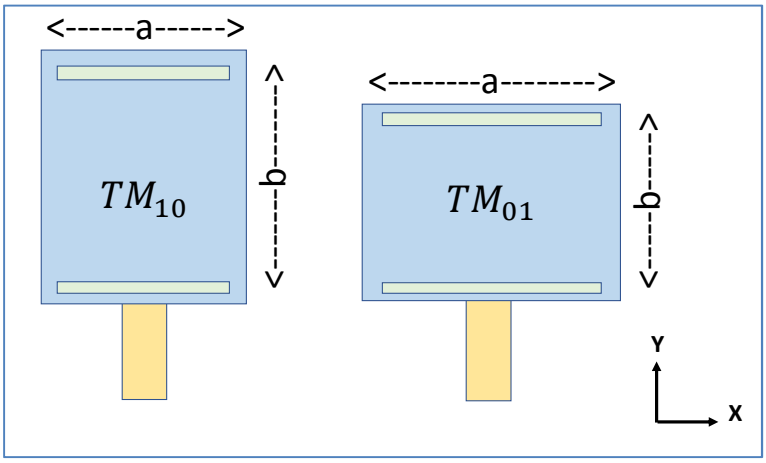

Figure 3-1: Physical Orientation versus Excitation Mode

Figure 3-1, which has been adapted by permission of SciTech Publishing [8], shows the aperture coupled microstrip patch antenna can either be elongated in the y-axis or elongated in the x-axis. When $a > b$, the TM_{01} is the lowest order mode and possesses the lowest resonant frequency. The TM_{10} is the next highest order mode and has the next lowest resonant frequency.

When $b > a$, the TM_{10} is the lowest order mode and TM_{01} is the next highest order mode [8, p. 24].

Elongation in the x-axis enables the implementation of longer resonant slots, which in turn enables the resonance associated with the slots to be generated at a lower frequency [16]. In other words, a smaller upper to lower resonance ratio can be achieved when the rectangular patch is elongated in the x-axis.

3.2.3 Choice of Material

The selection of a substrate material is a balance between the required electrical, mechanical, environmental, and economic constraints [8, p. 235].

The key electrical parameters of the substrate material are dielectric constant, represented by D_k (also known as relative permittivity represented by ε_r), and dissipation factor, represented by D_f (also known as loss tangent represented by $tan\delta$).

The dielectric constant, D_k, of the substrate determines the physical size of the patch antenna. The larger the dielectric constant, the smaller the element size, but also the smaller the impedance bandwidth and directivity [14]. Surface wave loss increases with larger D_k. The use of substrates with higher dielectric constant also tightens fabrication tolerances [8, p. 235].

The dissipation factor, D_f, of the substrate is a measure of the quantity of electrical energy that is converted to heat by a dielectric. The lowest possible loss tangent maximizes the antenna efficiency (decreases the losses) [8, p. 235]. The dielectric constant of the RF feed should be selected for good microstrip circuit qualities, typically in the range of 2 to 10 [14].

Overall, a high-performance laminate must be used at millimeter wave frequencies to minimize insertion loss.

Astra MT77 is chosen for the upper and lower substrate. The material is offered by Isola [20]. It is a very low loss laminate that exhibits exceptional electrical properties which are very stable over a broad frequency and temperate range. The material has a dielectric constant (D_k) of 3.0 and a dissipation factor (D_f) of 0.0017. It is currently offered in thickness 0.0050" (0.1270 mm), 0.0075" (0.1905 mm), 0.0100" (0.2540 mm), 0.0200" (0.5100 mm), 0.0300" (0.7600 mm), and 0.0600" (1.5000 mm). The available copper weights are 1⁄3, 1⁄2, and 1 oz.

A copper weight of 1⁄2 oz. is chosen for the patch and RF feed since this is a thickness commonly used today in the manufacture of PCB's (printed circuit boards). A copper weight of 1/3 oz. is chosen for the ground plane since it was noticed in the parametric analysis that larger thicknesses detune the antenna (APPENDIX C).

3.2.4 Choice of Antenna Substrate Thickness

Choice of the antenna substrate thickness impacts the mutual coupling between elements of the array, operational bandwidth, and back radiation levels. The operational bandwidth is calculated following the equations:

Equation 3-1

$$BW_{lower} = \frac{f_{Hi} - f_{Lo}}{f_o} = \frac{28.3\ GHz - 27.5\ GHz}{27.9\ GHz} = 2.9\%$$

Equation 3-2

$$BW_{upper} = \frac{f_{Hi} - f_{Lo}}{f_o} = \frac{40.0\ GHz - 37.0\ GHz}{38.5\ GHz} = 7.8\%$$

A plot of percent bandwidth of a rectangular patch versus the electrical thickness of the substrate is determined following [21, p. 244] and reproduced for a material with D_k of 3 (Figure 3-2).

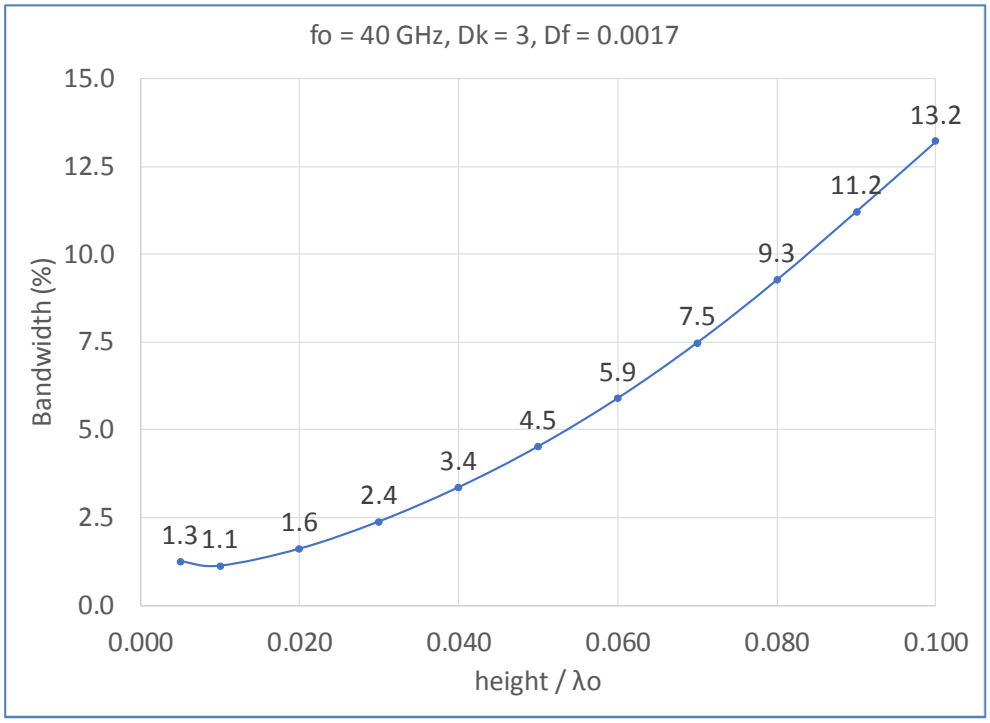

Figure 3-2: Percent Bandwidth versus Electrical Thickness of a Rectangular Patch Antenna

It is evident that an electrical thickness of 0.070 is required to achieve a bandwidth of 7.5%. The associated height is calculated as follows:

Equation 3-3

$$h_u = \lambda_o * 0.070 = \frac{c}{(f_r)_{01}} * 0.055 = \frac{299792458 \frac{m}{s}}{40\ GHz} * 0.070 = 0.525\ mm$$

Antennas on substrates that are 0.01-0.03 have yielded front-to-back ratios on the order of 20 dB [13]. A material thickness of 0.510 mm is chosen (as a starting point) for the upper substrate to achieve the required bandwidth. Attention will be given to the back-radiation levels shown in the simulation results.

For a resonant frequency of 31.8 GHz; the limitation on the height of the upper substrate, to avoid surface waves, is calculated following [8, p. 61].

Equation 3-4

$$h_u \leq \frac{0.3c}{2\pi(f_r)_{01}\sqrt{\varepsilon_r}} \leq \frac{0.3\left(299792458\frac{m}{s}\right)}{2\pi(31.8\,GHz)\sqrt{3}} \leq 0.026\,mm$$

Consequently, it is anticipated that a thickness of 0.510 mm will create challenges due to surface waves when trying to find the optimum spacing of the elements in the array.

3.2.5 Choice of Feed Substrate Thickness

Thinner microstrip substrates result in less spurious radiation from feed lines, but the path loss is high. A compromise of 0.01λ to 0.02λ is desirable [14]. For a resonant frequency of 31.8 GHz; the recommended limitations of the lower substrate height are calculated as follows:

Equation 3-5

$$h_l \geq 0.01\lambda \geq 0.01\frac{c}{(f_r)_{01}\sqrt{\varepsilon_r}} = 0.0364\,mm$$

Equation 3-6

$$h_l \leq 0.02\lambda \leq 0.02\frac{c}{(f_r)_{01}\sqrt{\varepsilon_r}} = 0.0728\,mm$$

A material thickness of 0.127 mm is used for the lower substrate since this is readily available in the lab. Again, attention will be given to the back-radiation levels shown in the simulation results.

3.2.6 Calculation of the Patch Effective Permittivity

For a relative permittivity of 3.0, a height of 0.510 mm, and a width of 3.312 mm; the effective permittivity of the upper substrate is calculated as follows [22, p. 460] – equation 8-205b:

Equation 3-7

$$\varepsilon_{effu} = \frac{\varepsilon_r + 1}{2} + \frac{\varepsilon_r - 1}{2}\left(1 + 12\frac{h_u}{W_u}\right)^{-1/2} = 2.59$$

3.2.7 Calculation of the Patch Width (x-axis)

For a resonant frequency of 31.8 GHz; the patch width is calculated as follows [4, p. 803] – equation 14-34:

Equation 3-8

$$W_u = \frac{c}{2(f_r)_{01}\sqrt{\varepsilon_r}} = \frac{299792458\ m/s}{2(31.8\ GHz)\sqrt{3}} = 3.334\ mm$$

3.2.8 Calculation of the Fringing Length (y-axis)

For an effective permittivity of 2.59, a width of 3.334 mm, and a height of 0.510 mm; the fringing length is calculated as follows [23]:

Equation 3-9

$$\Delta l = 0.412\frac{(\varepsilon_{effu} + 0.300)(W_u/h_u + 0.264)}{(\varepsilon_{effu} - 0.258)(W_u/h_u + 0.800)}h = 0.241\ mm$$

3.2.9 Calculation of the Patch Length (y-axis)

For a resonant frequency of 31.8 GHz, an effective permittivity of 2.59, and a fringing length of 0.241 mm; the patch length is calculated following the equation in APPENDIX A.

Equation 3-10

$$L = \frac{c}{2(f_r)_{01}\sqrt{\left(\frac{\epsilon_r}{\epsilon_{effu}}\right)\epsilon_r}} - 2\Delta L = 2.050\ mm$$

3.2.10 Calculation of the Aperture Width (y-axis)

The aperture width is one percent of the wavelength in free space [24]. For a resonant frequency of 31.8 GHz; the aperture width is calculated to be as follows:

Equation 3-11

$$Apeture\ Width = \left(\frac{c}{(f_r)_{01}}\right)\left(\frac{1}{100}\right) = 0.094\ mm$$

3.2.11 Calculation of the Aperture Length (x-axis)

For a resonant frequency of 31.8 GHz and an effective permittivity of 2.59; the aperture length can be adjusted to obtain the desired resistive part of the impedance [13]. The max length of the aperture is estimated to be less than a half wavelength and is estimated as follows:

Equation 3-12

$$Max\ Apeture\ Length < \left(\frac{c}{(f_r)_{01}}\right)\left(\frac{1}{\varepsilon_{eff}}\right)(0.49) = 1.782\ mm$$

The antenna was simulated in CST MWS using the parameters calculated in this chapter and then a parametric analysis was run on the length of the aperture, as per Table 3-2.

Table 3-2: Parameter Sweep Values for Aperture Length

Sweep Run #	% of λ in the Lower Substrate	Stub Length (mm)
1	47.2%	1.717
2	47.4%	1.724
3	47.6%	1.731
4	47.8%	1.739
5	48.0%	1.746
6	48.2%	1.753
7	48.4%	1.761

Figure 3-3 (simulation dimensions outlined in Table 4-1) indicates an aperture length of 1.739 mm (pink line) intersects the 50-ohm point of the y-axis at 31.8 GHz. It is the best choice to match the real part of the antenna impedance to 50-ohm input feed line.

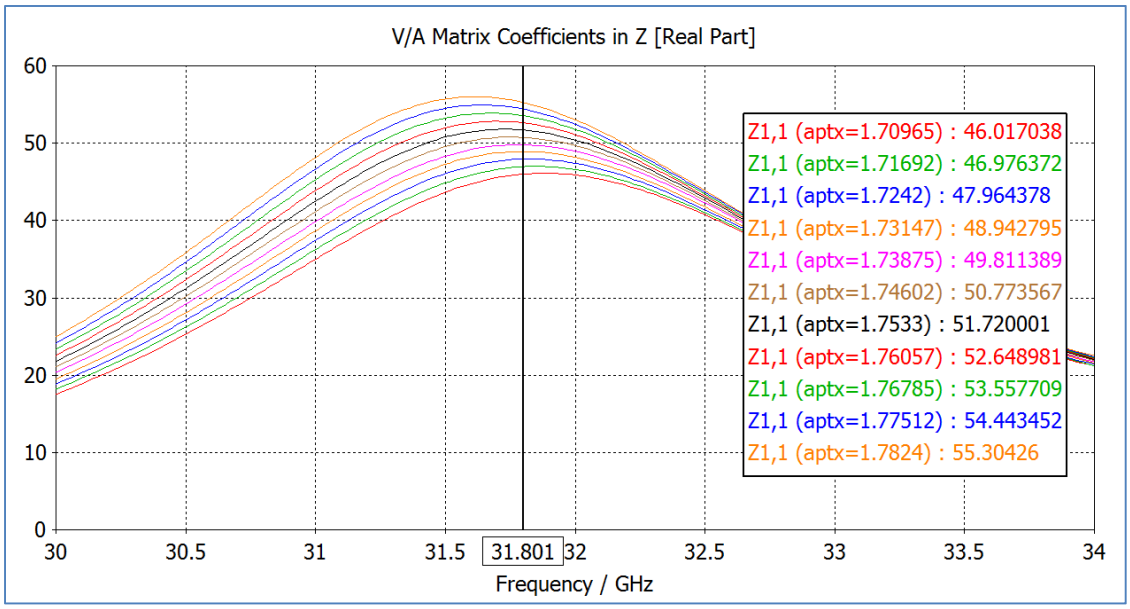

Figure 3-3: Input Impedance (Real) Versus Aperture Length

3.2.12 Calculation of the RF Feed Effective Permittivity and Width

The effective permittivity of the lower substrate is calculated following [22, p. 205] – equation 8-205b:

Equation 3-13

$$\varepsilon_{effl} = \frac{\varepsilon_r + 1}{2} + \frac{\varepsilon_r - 1}{2}\left(1 + 12\frac{h_l}{W_{feed}}\right)^{-1/2}$$

The width of the RF feed is calculated following [22, p. 205] – equation 8-205a:

Equation 3-14

$$Z_c = \frac{120\pi}{\sqrt{\epsilon_{effl}}\left[\frac{W_{feed}}{h_l} + 1.393 + 0.667\ln\left(\frac{W_{feed}}{h_l} + 1.444\right)\right]}$$

For a characteristic impedance of 50 ohms and a height of 0.127 mm; solving the two equations with two unknows yields:

Equation 3-15

$$\varepsilon_{effl} = 2.417 \; and \; W_{feed} = 0.321 \; mm$$

3.2.13 Calculation of the RF Feed Stub Length (y-axis)

For a resonant frequency of 31.8 GHz; the open-circuited stub length can be adjusted to obtain the desired reactance [13]. The max length of the stub is typically less than a quarter wavelength [14] and is estimated as follows:

Equation 3-16

$$Max \; Stub \; Length < \left(\frac{c}{(f_r)_{01}}\right)\left(\frac{1}{\varepsilon_{effl}}\right)(0.25) = 0.976 \; mm$$

Again, the antenna was simulated in CST MWS using the parameters calculated in this chapter and then a parametric analysis was run on the length of the stub, as per the Table 3-3.

Table 3-3: Parameter Sweep Values for Stub Length

Sweep Run #	% of λ in the Lower Substrate	Stub Length (mm)
1	16%	0.625
2	17%	0.664
3	18%	0.703
4	19%	0.742
5	20%	0.781
6	21%	0.820
7	22%	0.859

Figure 3-4 (simulation dimensions outlined in Table 4-1) indicates a stub length if 0.742 mm (pink line) has a max and a min that is symmetrical about the zero point of the y-axis, and is therefore the best choice to cancel out the reactance associated with the aperture fed antenna.

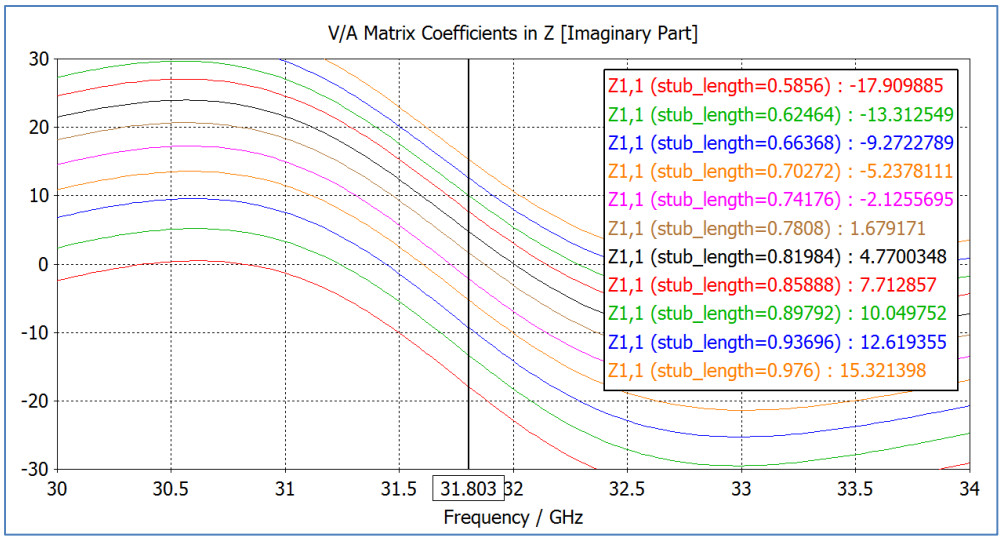

Figure 3-4: Input Impedance (Imaginary) Versus Stub Length

The S11 (dB) of the final aperture coupled microstrip antenna is given in Figure 3-5 (simulation dimensions outlined in Table 4-1). All other simulation results are in CHAPTER 4.

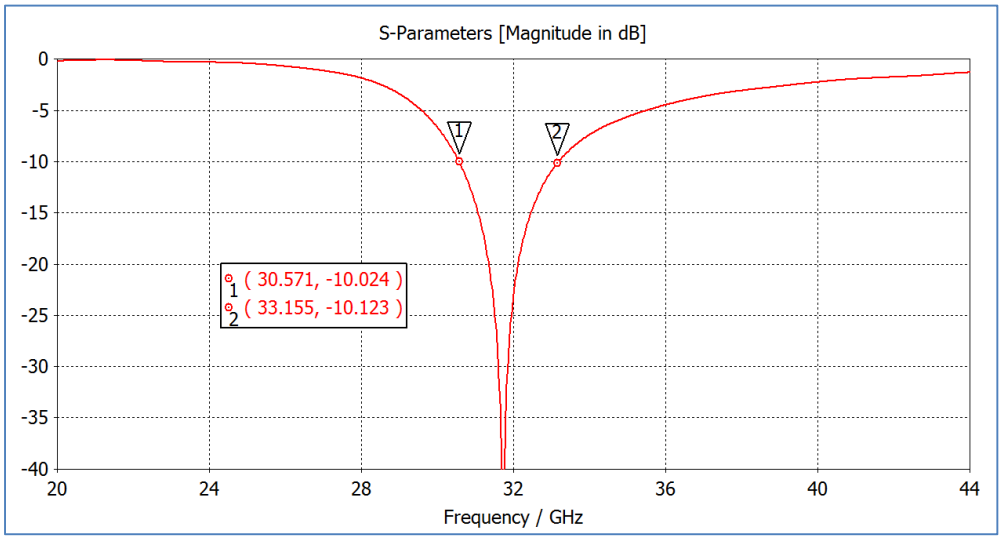

Figure 3-5: S11 Magnitude (dB) of Aperture Fed Antenna

3.3 Dual Band Microstrip Patch Antenna

Presented in [17, pp. 227, Eqn 8] is an equation to estimate slot length. The work however was completed on a dual band pin fed microstrip antenna, and consequently the equation is not entirely valid for an aperture fed microstrip antenna since the current flows are slightly different. Consequently, the dimensions of the resonant slot (length, width, and offset) in this work were determined empirically using CST MWS. After the slot dimensions were realized, an effort was made to determine a modified form of the equation in [17, pp. 227, Eqn 8] and the work is presented in APPENDIX B.

3.3.1 Estimation of the Resonant Slot Dimensions

To ensure a good radiation efficiency at both frequencies, the aspect ratio between the two sides of the patch is fixed in the range [17]:

Equation 3-17

$$0.7 < L/W < 0.8$$

Using $L = 2.050\ and\ W = 3.334\ mm$, it follows that L/W is equal to 0.615 and does not meet the stated criteria. Since $L\ and\ W$ were determined during the design of the aperture coupled microstrip antenna, then the only option is to proceed with these dimensions. Attention will be given to the radiation efficiency shown in the simulations of the final dual band antenna.

The best antenna performance in terms of both radiative properties and simultaneous impedance matching at the two operating frequencies is obtained when the width d of the two slots is comparable with the thickness h_u of the upper substrate and when [17]:

Equation 3-18

$$\frac{L}{50} < w < \frac{L}{15}\ \ldots\ and\ \ldots\ l < \frac{W}{10}$$

Using L = 2.050 and W = 3.334 mm, it follows that 0.041 mm < w <0.137 mm … and … l < 0.334 mm. Since the thickness of the upper substrate was already chosen to realize a large operational bandwidth, then it is not feasible to make the width d of the two slots comparable with the thickness h_u. Otherwise such a large width of the slot will not perturb the 3rd order mode in manner that generates a usable upper resonance.

Consequently, and as a starting point, d is chosen to be the same as w, which is chosen to be the same as l (where d is slot width, slot w is the offset from bottom edge of patch, and l is slot offset from side edge of patch. This aligns with the approach taken by Maci, et al to generate a half-wavelength microstrip resonator [17].

As per Table 3-4, a parametric analysis, with a sweep step size of 0.010 m, was run on the resonant slot dimensions keeping $l = d = w$.

Table 3-4: Parameter Sweep Values Versus Resonant Slot dimensions

Sweep Run #	Wu (mm)	Ls (mm)	l = d =w (mm)
1	3.334	3.252	0.042
2	3.334	3.232	0.052
3	3.334	3.212	0.062
4	3.334	3.192	0.072

Although the criteria states that $w < 0.140\ mm$ is feasible, it was quickly seen that resonant slots with dimensions above 0.720 mm would not be usable due to the excessive shift in the upper resonance. Hence, the parametric analysis is limited to 4 sweeps.

Figure 3-6 indicates resonant slot dimensions between 0.420 mm (red line) and 0.520 mm (green line) will generate a dual band antenna that has a lower resonance centered at roughly 28 GHz and an upper resonance centered at roughly 38 GHz. However, with the implementation of the resonant slots the antenna is now detuned.

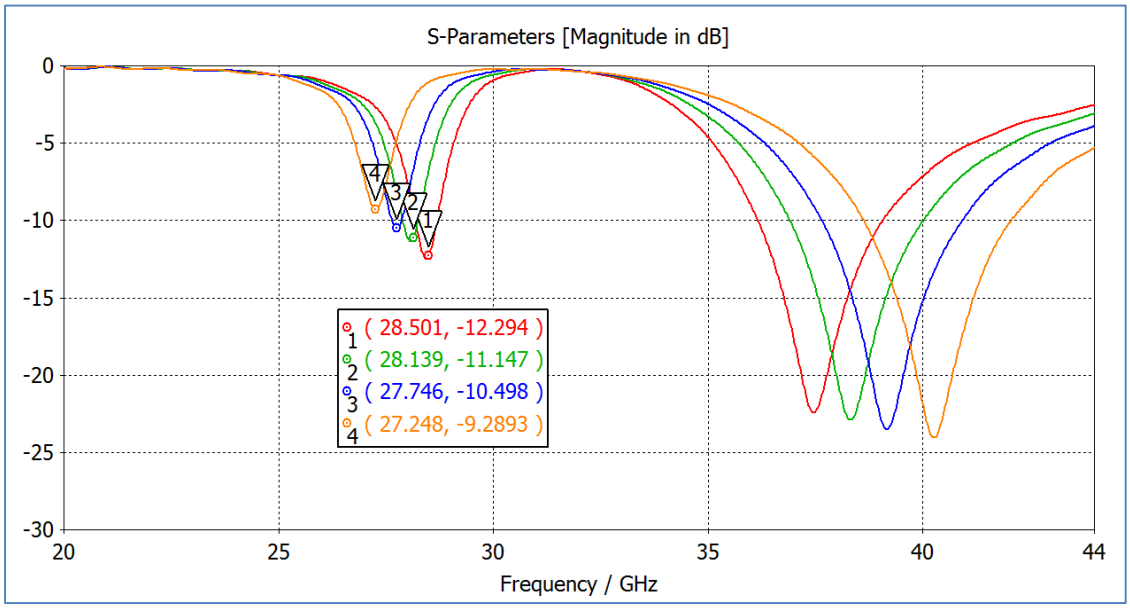

Figure 3-6: S11 (dB) Versus Resonant Slot Dimensions of 32.0 GHz Aperture Antenna

A parametric analysis on aperture length and stub length was done on the dual band antenna following the process outlined in Chapter 3. The following parameters were obtained:

- Aperture Length: 1.940 mm
- Stub Length: 0.8465 mm

Using the new values for aperture length and stub length a second parametric analysis, with a sweep step size of 0.002 mm, was run on the resonant slot dimensions keeping $l = d = w$, as per Table 3-5.

Table 3-5: Parameter Sweep Values versus Resonant Slot dimensions

Sweep Run #	Wu (mm)	Ls (mm)	L = d = w (mm)
1	3.334	3.252	0.042
2	3.334	3.248	0.044
3	3.334	3.244	0.046
4	3.334	3.240	0.048
5	3.334	3.236	0.050
6	3.334	3.232	0.052

Figure 3-7 indicates sweep #5 (pink line) centers the lower resonance at 28 GHz. The antenna however still does not meet the desired performance due to lack of bandwidth at the lower resonance.

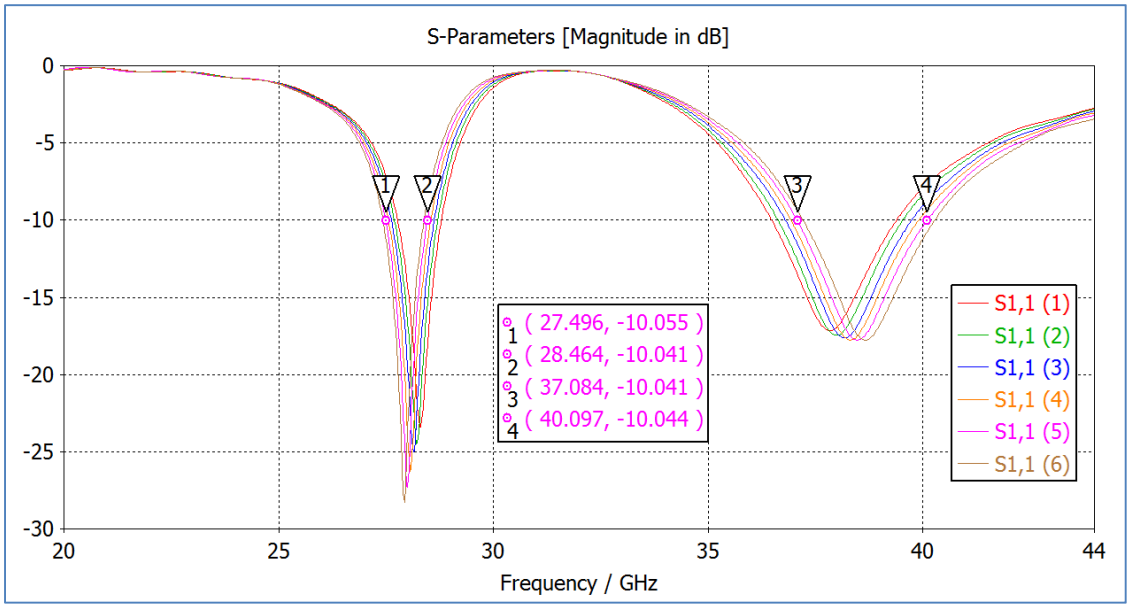

Figure 3-7: S11 (dB) Versus Resonant Slot Dimensions of 31.7 GHz Aperture Antenna

As w increases the slot creeps away from the edge of the patch where the 3rd order mode is strongest. Therefore, it is reasonable to keep w as small as feasible while tuning the parameters l & d to achieve desired performance.

3.3.2 Determination of the Resonant Slot Dimensions

A parametric analysis was run on all the antenna parameters (APPENDIX C) and then the antenna was tuned to generate the desired dual-band response using the knowledge summarized in Table C-2. The optimized values are as follows:

- Aperture Length: set 1.940 mm
- Stub Length: set to 0.847 mm
- Slot Width (d): set to 0.052 mm
- Slot Edge in x-axis from patch edge (w): set to 0.045 mm
- Slot Edge in y-axis from edge of patch (l): set to 0.043 mm

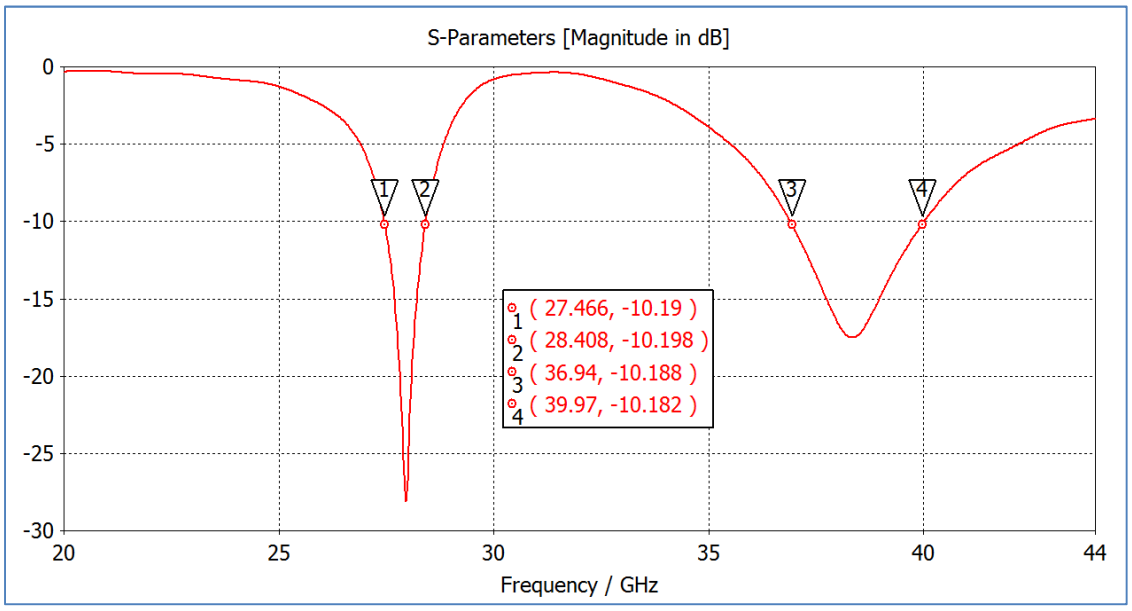

Figure 3-8: S11 Magnitude (dB) of the Dual Band Antenna

It is primarily the slot length, and secondarily the parameter l, that determines the upper resonance frequency. An l of 0.043 mm corresponds to a slot length of 3.250 mm. The "dialed-in" frequency response of the dual band antenna is given in Figure 3-8 (simulation dimensions as per Table 4-2). All the other simulation results are presented and discussed in CHAPTER 4.

3.3.3 Array Network

With a dual band antenna, the goal is to find a spacing pattern that will generate a sidelobe suppression, at both the lower and upper resonance, that is equal to or better than the sidelobe suppression in a uniform array operating in a single band. Therefore, the target is to have a sidelobe suppression that is equal to, or better than, -13.2 dB, at both operating bands.

Many array patterns were experimented with in the simulation tool and the associated side lobe suppression is listed in Table 3-6. Diagrams of each array pattern can be found in APPENDIX D. A spacing of 4.0 mm is λ/2 at upper resonance and ~λ/3 at lower resonance. A spacing of 5.6 mm is ~2λ/3 at upper resonance and λ/2 at lower resonance. The square and square-offset array patterns with 4.0 mm x 4.0 mm spacing meet the design goal; however, the spacing of the elements are too close to allow routing of RF input feed. The square and square-offset array patterns with 5.6 mm x 5.6 mm spacing are just short of the design goal at the upper resonance. The checkered square patterns yield excellent performance at the lower resonance, but at the upper resonance there is a large lobe that runs along the x-y plane. This configuration could possibly be used in an application that does not require large scan angle. The checkered 3x3 diamond pattern with 8.0 mm x 8.0 mm spacing has excellent performance at the lower resonance and just misses the design goal at the upper resonance, and it is noticed the same pattern with 4x4 elements slightly improves the side lobe suppression. The checkered 3x3 and

4x4 diamond patterns with 11.2 mm x 11.2 mm spacing have poor performance. Overall, the checkered diamond pattern (Figure 3-9) yields reasonable sidelobe suppression and allows enough room for routing of RF input signals.

Table 3-6: Sidelobe Suppression for Various Array Shapes

Array Shape	Array Size	Number of Elements	Array Spacing (mm)	Lower Resonance Sidelobe (dBc)	Upper Resonance Sidelobe (dBc)
Square	4x4	16	4.0x4.0	19.9	14.3
Square	4x4	16	5.6x5.6	14.2	12.7
Square, Offset	4x4	16	4.0x4.0	17.9	14.3
Square, Offset	4x4	16	5.6x5.6	14.2	12.7
Square, Checkered	4x2	8	8.0x8.0	14.4	7.6
Square, Checkered	4x2	8	11.2x11.2	16.5	8.3
Diamond, Checkered	3x3	9	8.0x8.0	15.8	12.5
Diamond, Checkered	3x3	9	11.2x11.2	12.8	7.5
Diamond, Checkered	4x4	16	8.0x8.0	14.5	12.7
Diamond, Checkered	4x4	16	11.2x11.2	13.0	8.2

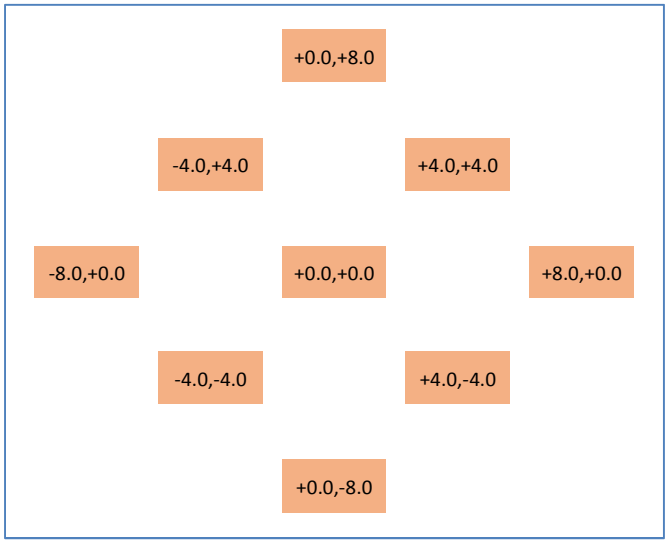

Figure 3-9: Checkered Diamond 3x3 Array with 8.0 x 8.0 mm Spacing

The challenge with developing an RF feed network for a checkered 3x3 diamond array with aperture fed antennas is finding a way to feed the elements without creating cross talk due to coupling. Initially, an attempt was made to feed the bottom elements and the top elements from opposite directions in the y-axis. This led to a valuable lesson into the nature of the aperture fed antenna which does not exist with the pin fed antenna. When feeding elements from opposite directions the phase need be 180° out of synchronization to get proper constructive and destructive interference in the radiation pattern. With this finding in hand, there remained an open question on how to feed the center element. Consequently, and as a starting point, it was decided to fabricate a checkered linear 4x1 array (Figure 3-10), which is a subset of the larger diamond. The idea is to get the linear array working first, and then determine the feed network for the diamond pattern in a later work.

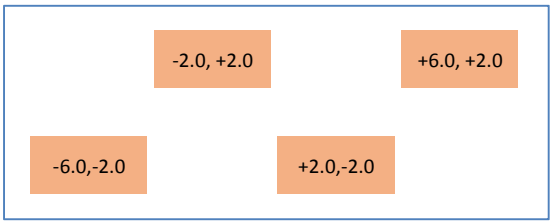

Figure 3-10: Checkered Linear 4x1 Array with 8.0 x 4.0 mm Spacing

3.3.4 RF Feed Network

The RF feed network for the checkered linear 4x1 array consists of a Wilkinson splitter feeding two more Wilkinson splitters [25]. The block diagram is given in Figure 3-11, and is representative of the bottom view of the PWB (hence the output feed lines seemingly do not align with the elements in Figure 3-1). Each Wilkinson splitter consists of two quarter wave transformers that were designed to operate at the midpoint between the lower and upper

resonance (32 GHz). The characteristic impedance of each quarter wave transformer is 70.7 ohms, ensuring a proper match between 50-ohm input and 50-ohm output. Each quarter wave transformer has a 100-ohm resistor placed between the output ports, to improve matching for all ports and improve isolation between each output port. The dimensions of the of the quarter wave transformer are easily determined as per the work of Wilkinson [25]. The width of the RF feed line was calculated earlier in Section 3.2.12, and following the same process the width of the quarter wave transformer is calculated to be 0.178 um.

Equation 3-19

$$Z_{Quarter} = Z_o\sqrt{2} = 50\sqrt{2} = 70.7\ ohms$$

Equation 3-20

$$l = \frac{\lambda}{4} = \frac{\frac{c_o}{\sqrt{\varepsilon_{effl}} * f}}{4} = 1.512\ mm$$

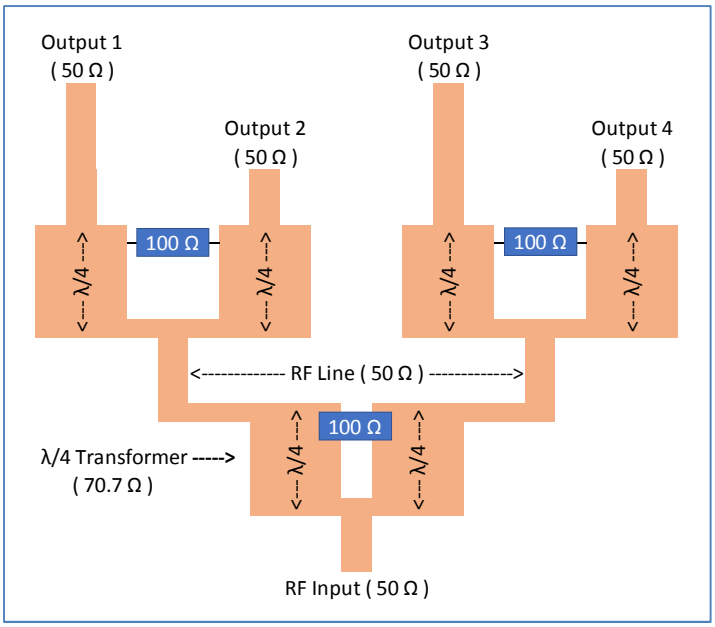

Figure 3-11: RF Feed Network Block Diagram

Each output RF trace is of different length since the elements in the array are slightly offset in the y-axis. Unequal lengths will generate an unequal change in phase. If nothing is done to compensate for the unequal lengths then the radiation pattern of the array will take on an unexpected shape. Consequently, each RF path must be of equal distance to ensure matching of phase at each antenna element. The length of the RF traces that feed the lower elements can extended by implementing an "s-pattern". The extra bends associated with the "s-pattern" create a disturbance in the phase, making it difficult to match phase even when all RF paths are of the same length. Consequently, extra bends were implemented into the longer RF path simply to enable better phase matching. A picture of the final 4x1 RF feed network is given in Figure 3-12. A magnified view of the Wilkinson splitter is given in Figure 3-13.

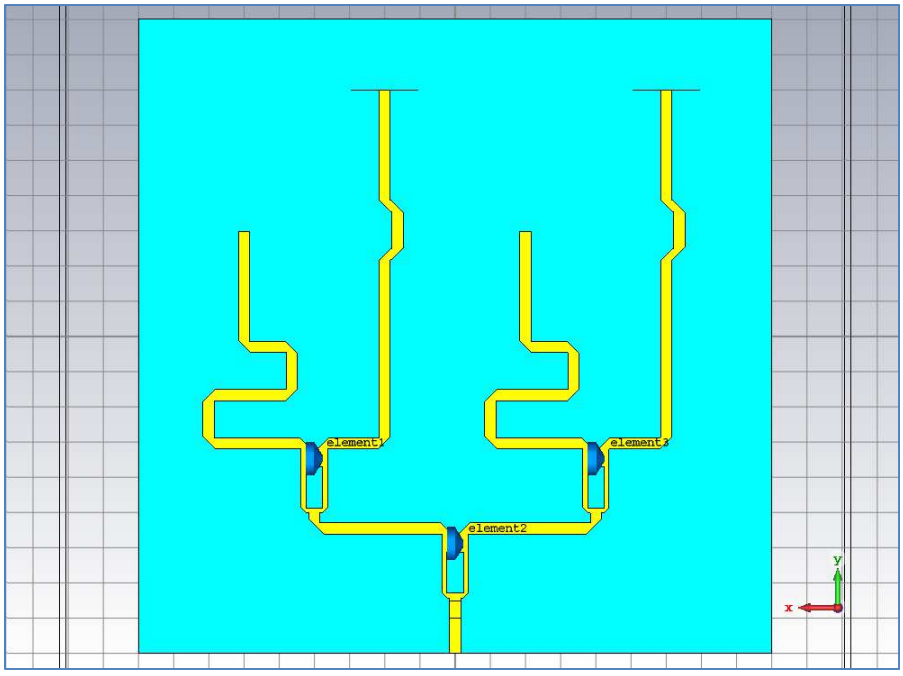

Figure 3-12: RF Feed Network Layout in CST MWS

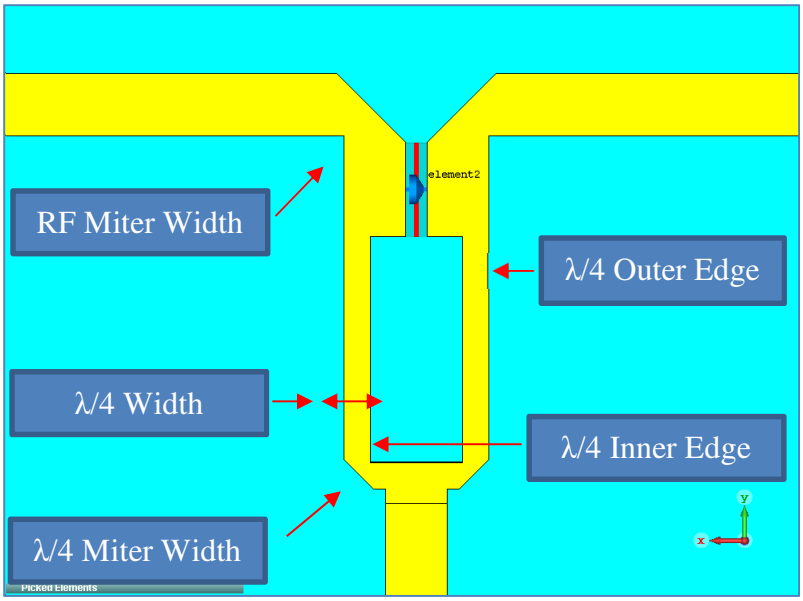

Figure 3-13: Wilkinson Splitter Layout in CST MWS

The mitered edges are sloped at 45°. Critical to performance is the extent to which the mitered edges cut into the width of RF trace. The feed network was simulated in AWR [26] and the dimensions of the transformer were tweaked using the "tuning" feature to achieve optimal return loss and phase match in both operating bands. The final dimensions are given in Table 3-7.

Table 3-7: Final Dimensions of Wilkinson Splitter

Parameter	Value	Comments
λ/4 Width	0.136 mm	
λ/4 Outer Edge	1.667 mm	
λ/4 Miter Width	0.085 mm	At the narrowest point
λ/4 Miter Width	0.085 mm	At the narrowest point
RF Trace Miter Width	0.200 mm	At the narrowest point

CHAPTER 4

SIMULATION RESULTS & COMPARISON

This chapter begins with an overview of the software used to simulate the radiators. Next are presented the simulations for the single band antenna, the dual band antenna, the theoretical arrays, the RF feed, and the linear array using the RF feed. A comparison of the simulations for the various radiators is given at the end of this chapter.

4.1 Simulation Software Overview

CST MWS 2015 is used to generate the numerical solution using the Antenna Workflow within the Microwave Suite [3].

A CST MWS simulation can be run using one of six offered solvers: time domain, frequency domain, eigenmode, integral equation, asymptotic, and multilayer. All simulations in this chapter have been run using the time domain solver with mesh type "hexahedral TLM" set to an accuracy of -40 dB. As a rule of thumb, the size of the mesh cell should never be larger than 8 cells per wavelength [27]. In this chapter, and to ensure good accuracy, the largest cells were set to 15 cells per wavelength and the smallest cells were set to 20 cells per wavelength (where wavelength is associated with the highest frequency in the simulation). The meshing was done automatically.

CST MWS offers two types of ports to feed the RF signal; discrete ports and waveguide ports. Weiland, Timm, and Munteanu authored an article on commercial tools used for electromagnetic simulation titled "Practical Guide to 3D Simulation" [27]. The authors outline

in detail the differences between the types of ports used to feed the input signal. A summary of their more salient points follows in the next two paragraphs.

The discrete port is placed between the RF feed line and the ground plane, and feeds the signal to the RF line at a discrete point. The user must input the TEM mode and line impedance, and then during simulation CST MWS will calculate the voltage and current. Discrete ports introduce a parasitic series inductance, which is proportional to the distance between the RF feed and the ground. As such, discrete ports will always introduce a small perturbation into the numerically calculated solution. The only way to eliminate the perturbation is to extend the excited transmission line to infinity to eliminate the appearance of reflections, which of course is not practical.

Waveguide ports were introduced as a means of truncating the infinite line, without introducing any perturbations. The waveguide port is placed perpendicular to the RF feed line. The user must input the area of the waveguide port (i.e. the area for the eigen mode solution), and then during simulation CST MWS will calculate the E-field, H-field, line impedance, and propagation constant. Waveguide ports provide a better match to the mode pattern as well as higher accuracy for the S-parameters [28].

A waveguide port has been used in all simulations presented in this chapter. It was centered in the x-axis and placed at the edge of the substrate. The shielding feature was not enabled. The patch is centered over the substrate. In the following plots the red line indicates the reference plane of the waveguide port is set at the center of the aperture and the green line indicates it has been set at a ¼ wavelength from the center of the aperture.

4.2 CST MWS Simulations of Aperture Fed Antenna

The simulations run using the parameters specified in Table 4-1.

Table 4-1: Aperture Fed Antenna Simulation Dimensions

Parameter	Value	Parameter	Value
Patch Width	3.336 mm	Upper Substrate Height	0.510 mm
Patch Length	2.050 mm	Upper Substrate Er	3.0
Aperture Width	0.094 mm	Lower Substrate Height	0.127 mm
Aperture Length	1.739 mm	Lower Substrate Er	3.0
Stub Length	0.742 mm	Copper Thickness	18 um (1/2 oz.)
Stub & Feed Width	0.321 mm	Ground Plane Thickness	12 um (1/3 oz.)
Substrate Width	6 mm	Substrate Length	8 mm

4.2.1 Aperture Fed Antenna S11 (Magnitude and Phase)

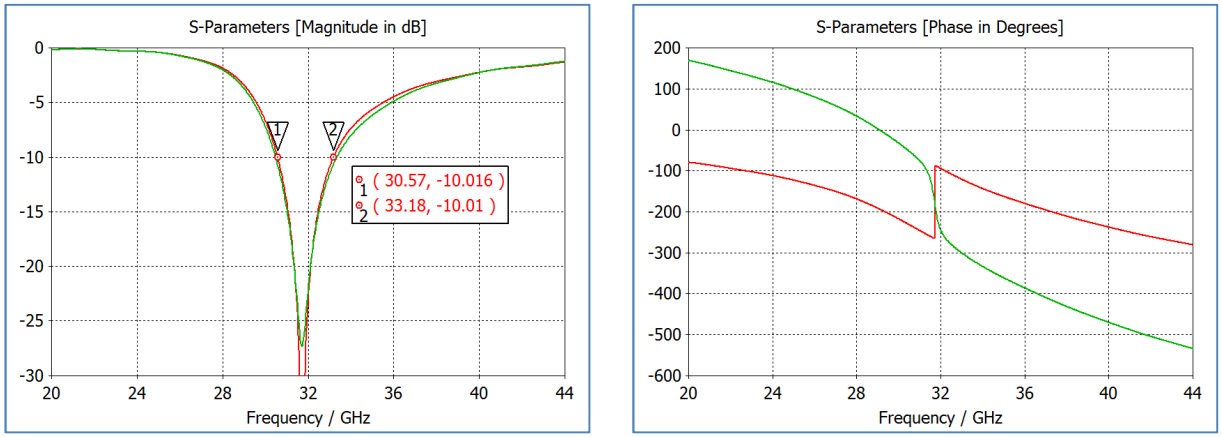

Figure 4-1: Aperture Fed Antenna S11 (Magnitude & Phase)

The resonant frequency is 31.7 GHz. The 10 dB return loss bandwidth is 8.2% and extends from 30.6 GHz to 33.2 GHz. The phase changes rapidly at the resonant frequency and

the phase difference between the red line and the green line (from the center of the aperture to the quarter wavelength reference point), within the 10-dB bandwidth, is roughly 180°.

4.2.2 Aperture Fed Antenna Z-Smith Chart

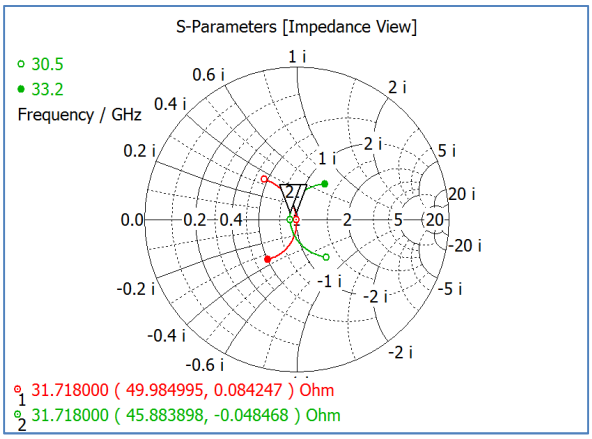

Figure 4-2: Aperture Fed Antenna Z-Smith Chart

The arc of the S11 is symmetrical within the 10-dB bandwidth and rotates about the center of the Z-Smith Chart indicating the antenna is matched to a 50-ohm system.

4.2.3 Aperture Fed Antenna Input Impedance (Real & Imaginary)

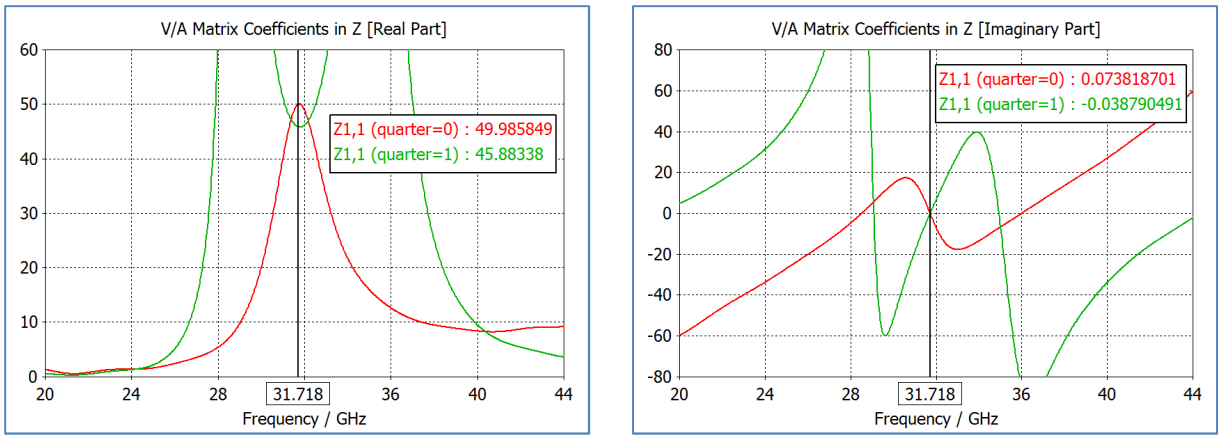

Figure 4-3: Aperture Fed Antenna Input Impedance (Real & Imaginary)

At the resonant frequency, the real part of the input impedance wobbles about the 48-ohm point and the imaginary part of the input impedance wobbles about the 0-ohm point.

4.2.4 Aperture Fed Antenna 3D Farfield Plot

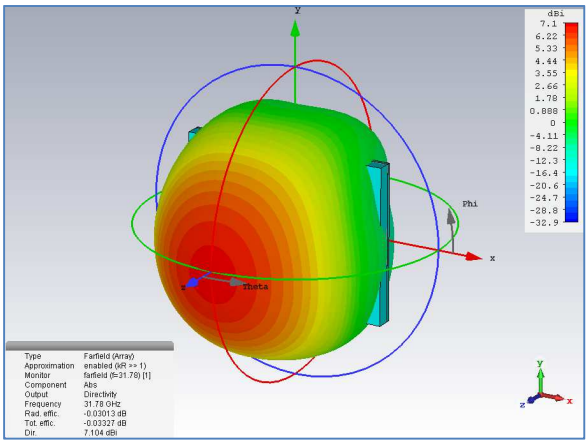

Figure 4-4: Aperture Fed Antenna 3D Farfield Plot

The radiation pattern is shaped like a sphere and has a directivity of 7.1 dBi in the broadside. The radiation efficiency is 99.3% (-0.03 dB).

4.2.5 Aperture Fed Antenna Polar Plots

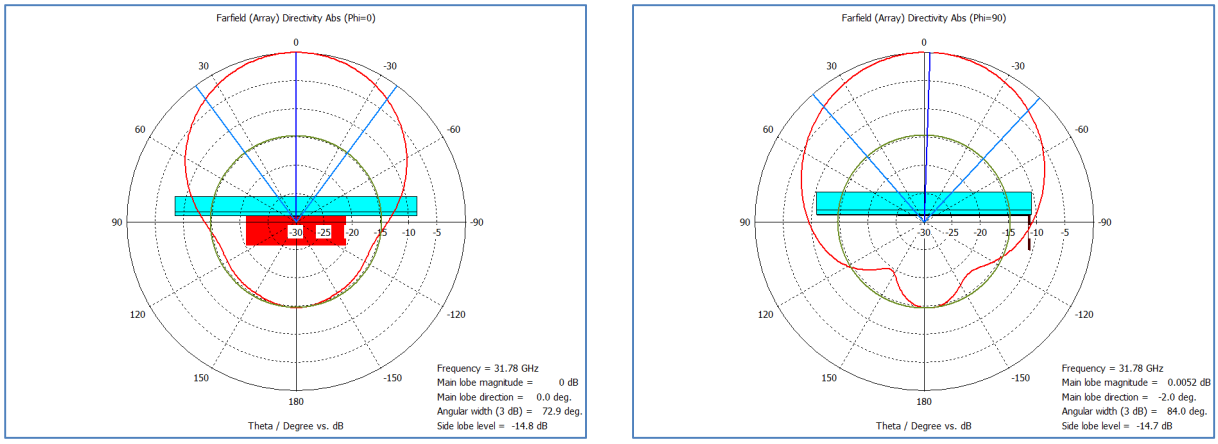

Figure 4-5: Aperture Fed Antenna Polar Plot, Phi = 0 & Phi = 90

The back lobe is – 14.7 dB down from the main lobe and would be smaller if either the upper or lower substrate were thinner. The angular width (3db) is 72.9° for Phi = 0° and 84.0° for Phi = 90°.

4.2.6 Aperture Fed Antenna Surface Current

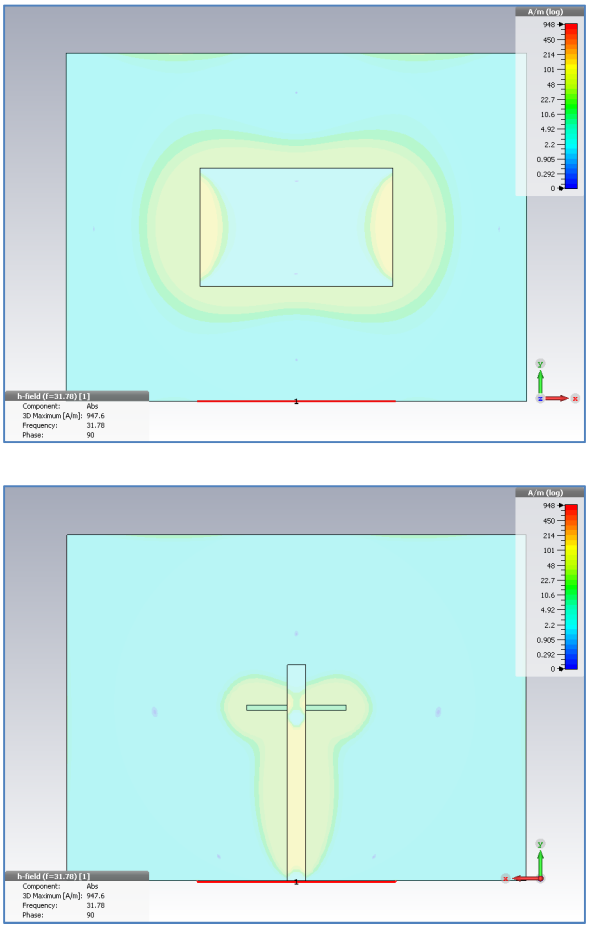

Figure 4-6: Aperture Fed Antenna Surface Current (Phase = 90°)

The current distribution is strongest on the edges of the patch, around the aperture, and in the RF feed. The current flow along the length of the patch (along the inside of the y-axis edges) determines the resonant frequency. During the design phase this length was set to be 1/2 of a

wavelength in the respective dielectric substrate. There is little to no current flow along the width of the patch (inside of the x-axis edges).

4.3 CST MWS Simulations of Dual Band Antenna

The simulations were run using the parameters specified in Table 4-1 in conjunction with the updated or new parameters specified in Table 4-2. The center of the resonant slot is offset from the x-axis edge of the patch by 0.071 mm in the y-axis.

Table 4-2: Dual Band Antenna Simulation Dimensions

Parameter	Value	Parameter	Value
Aperture Length	1.940 mm	Stub Length	0.847 mm
Slot Width	0.052 mm	Slot Length	3.250 mm

4.3.1 Dual Band Antenna S11 (Magnitude & Phase)

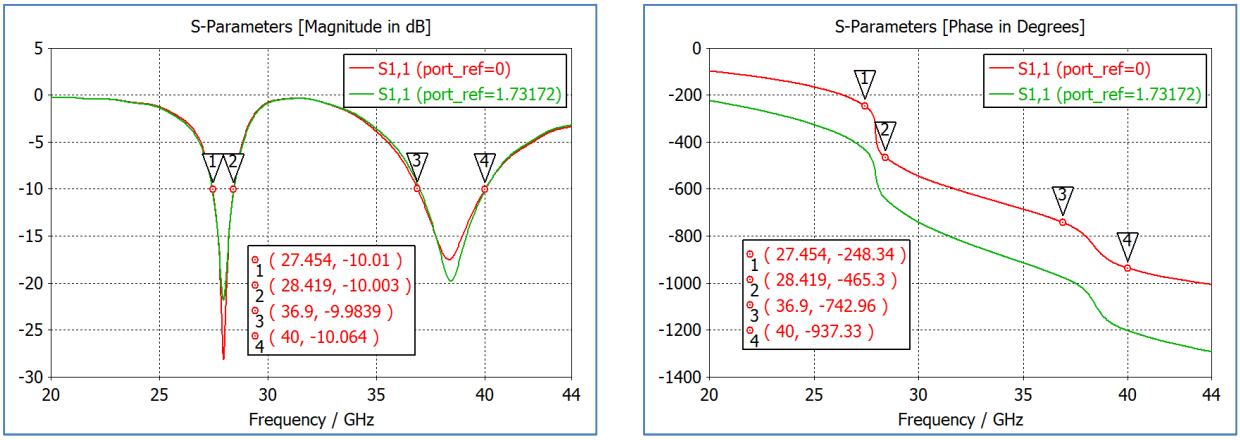

Figure 4-7: Dual Band Antenna S11 (Magnitude & Phase)

There are two resonant frequencies; one at 27.9 GHz and the other at 38.5 GHz. The lower resonance has a 10 dB return loss bandwidth of 3.2% and extends from 27.5 GHz to 28.4

GHz. The upper resonance has a 10 dB return loss bandwidth of 7.9% and extends from 36.9 GHz to 40.0 GHz. The phase changes rapidly at the resonant frequencies. Since the magnitude of the upper resonance is not as narrow and deep as the lower resonance, then the phase change of the upper resonance is not as steep and rapid as the lower resonance. At the lower resonance, the phase difference between the red line and the green line (from the center of the aperture to the quarter wavelength reference point), within the 10-dB bandwidth, is roughly 180°. At the upper resonance, the difference between the red line and the green line is not a quarter of a wavelength (1.732 mm is roughly 1/3 of a wavelength at 38.5 GHz) and therefore the phase difference is not 180°.

4.3.2 Dual Band Antenna Z-Smith Chart

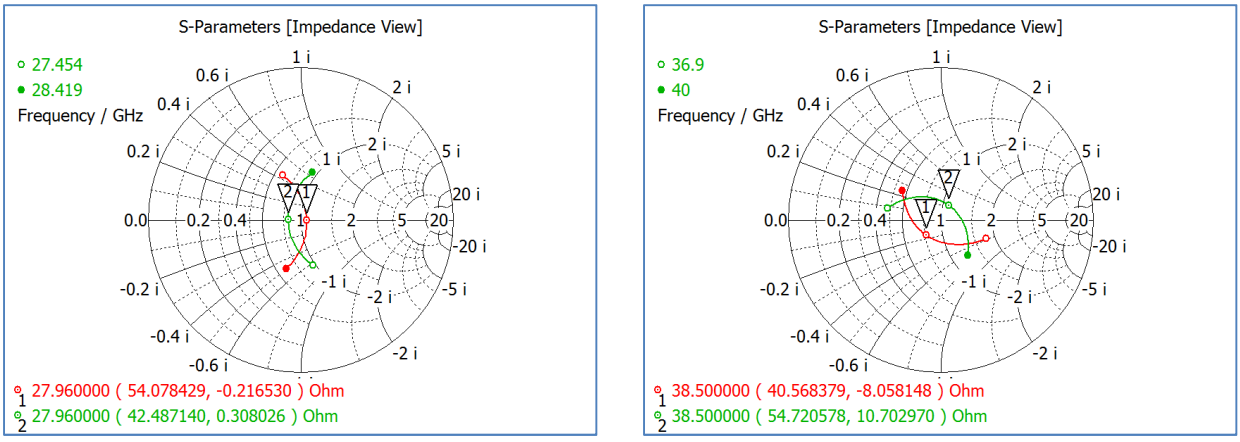

Figure 4-8: Dual Band Antenna Z-Smith Chart at 28 GHz & 38 GHz

The arc of each S11 is symmetrical within the 10-dB bandwidth and rotates around the center of the Z-Smith Chart indicating the antenna is matched to a 50-ohm system. The reference plane for the wave guide port was offset from the center of the aperture by 1.732 mm (1/4 wavelength at 27.9 GHz) for the lower resonance, and, by 1.255 mm (1/4 wavelength at

38.5 GHz) for the upper reference. This is the reason both plots show a quarter wavelength rotation from red line to green line.

4.3.3 Dual Band Antenna Input Impedance (Real & Imaginary)

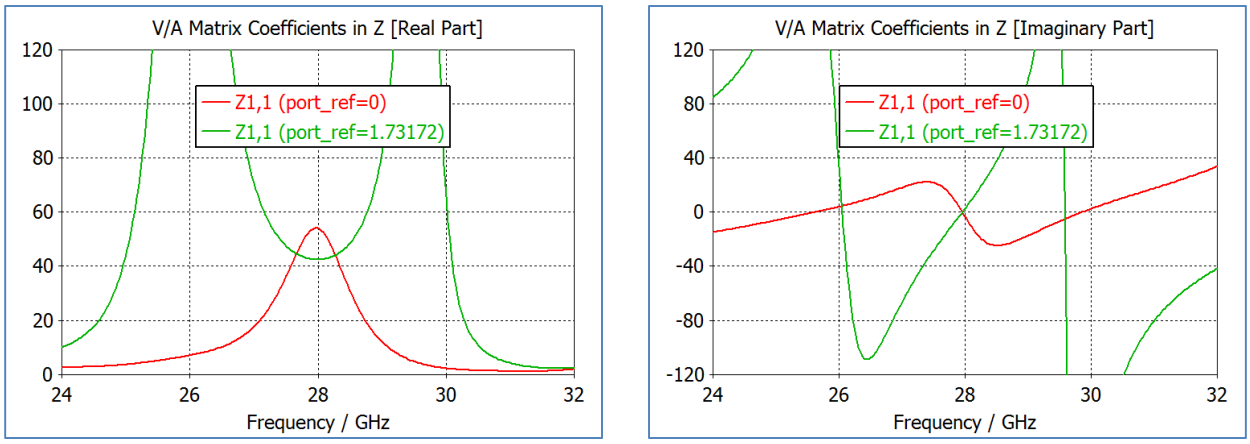

Figure 4-9: Dual Band Antenna Input Impedance (Real & Imaginary) at 28 GHz

At the lower resonance, the real part of the input impedance wobbles about the 48-ohm point and the imaginary part of the input impedance wobbles about the 0-ohm point.

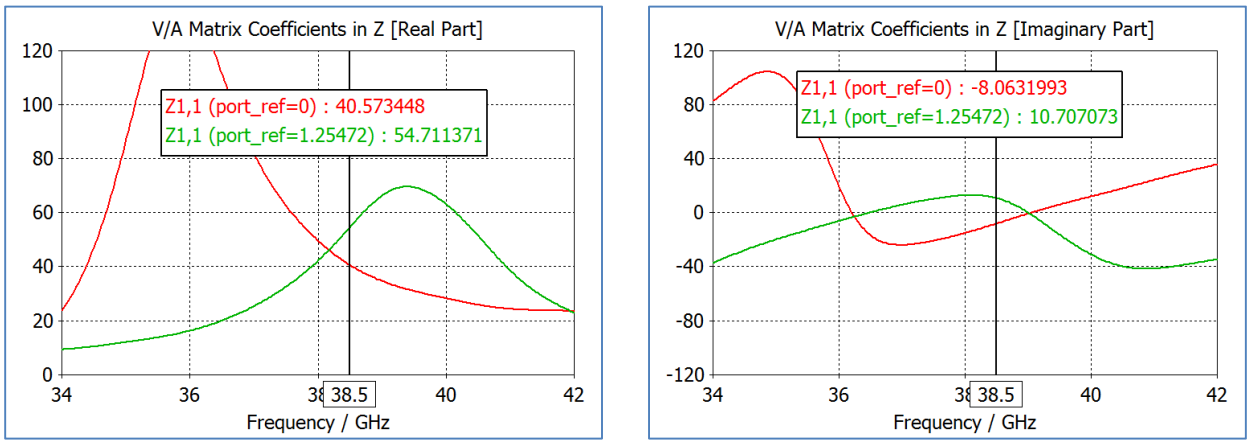

Figure 4-10: Dual Band Antenna Input Impedance (Real & Imaginary) at 38 GHz

At the upper resonance, the real part of the input impedance wobbles about the 47-ohm point and the imaginary part of the input impedance wobbles about the 0-ohm point.

4.3.4 Dual Band Antenna 3D Farfield Plot

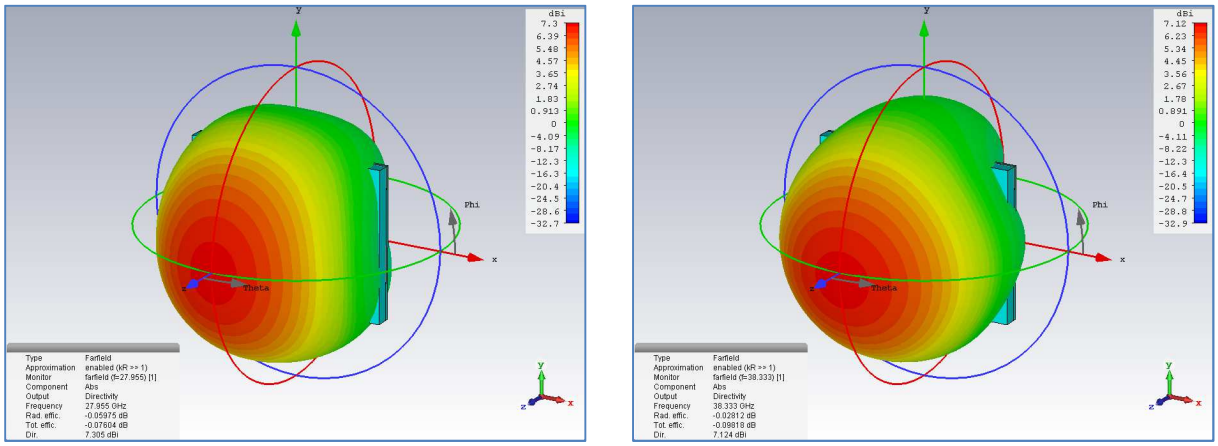

Figure 4-11: Dual Band Antenna 3D Farfield Plot at 28 GHz & 38 GHz

For both the lower and upper resonance, the radiation pattern is shaped like a sphere and have a directivity of 7.1 dBi in the broadside. At the lower resonance, the radiation efficiency is 98.6% (-0.06 dB) which is worse than the single band antenna. At the upper resonance, the radiation efficiency is 99.3% (-0.03 dB) which is the same as the single band antenna.

4.3.5 Dual Band Antenna Polar Plots at Lower Resonance

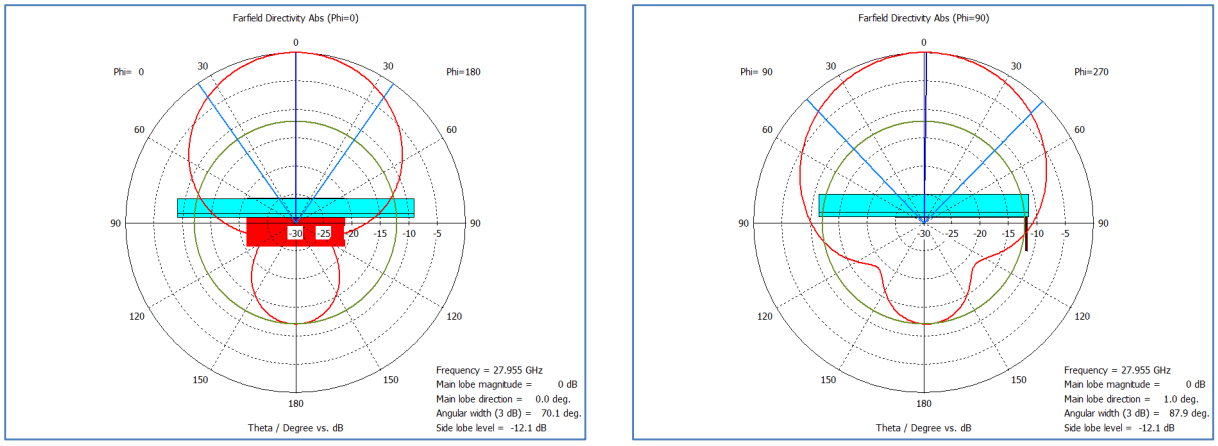

Figure 4-12: Dual Band Antenna Polar Plots at 28 GHz, Phi = 0 & Phi = 90

For the lower resonance the back lobe is 12.1 dB lower than the main lobe, which is ~ 2dB worse than the single band antenna, and would be smaller if either the upper or lower substrate were thinner. The angular width (3db) is 70.1° for Phi = 0° and 87.9° for Phi = 90°, which is roughly the same as the single band antenna.

4.3.6 Dual Band Antenna Polar Plots at Upper Resonance

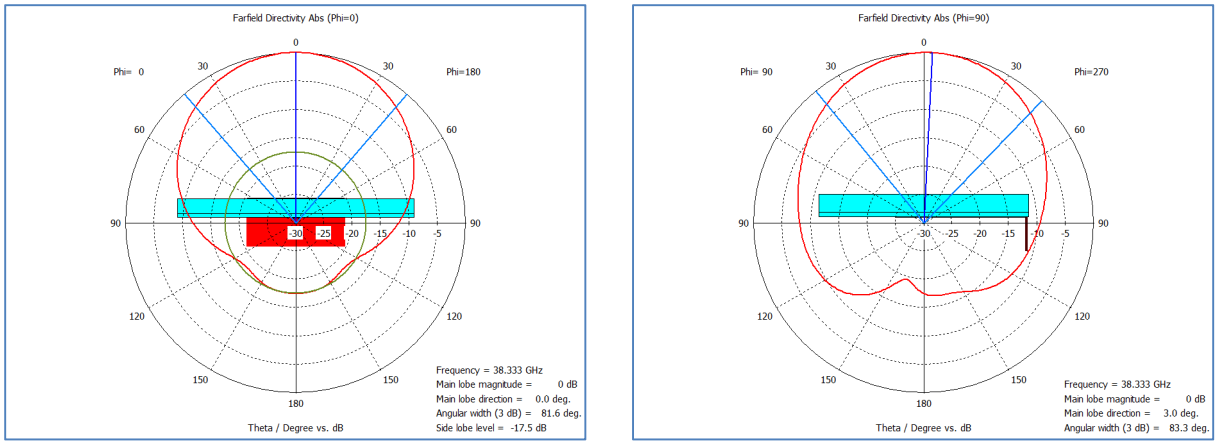

Figure 4-13: Dual Band Antenna Polar Plots at 38 GHz, Phi = 0 & Phi = 90

For the upper resonance the back lobe is 17.5 dB lower than the main lobe, which is ~ 3 dB better than the single band antenna. The angular width (3db) is 81.6° for Phi = 0° and 83.3° for Phi = 90°, which is roughly the same as the single band antenna. Since the upper resonance is associated with the slots in the microstrip patch then it stands to reason that the back lobe generated by the upper resonance will be smaller than the back lobe generated by the lower resonance.

4.3.7 Dual Band Antenna Surface Current

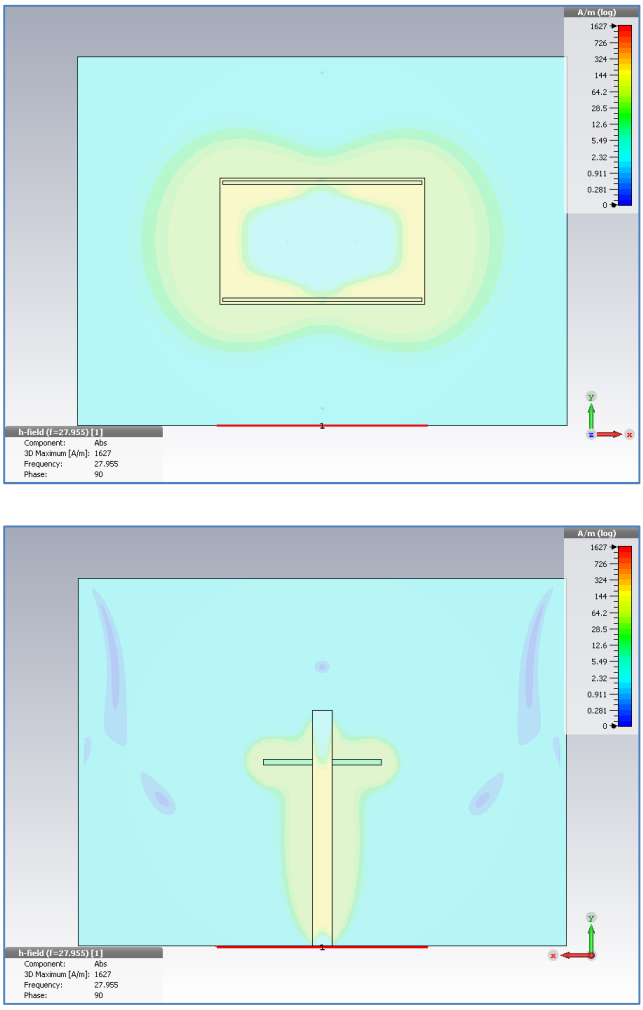

Figure 4-14: Dual Band Antenna Surface Current at 28 GHz (Phase = 90°)

At the lower resonance, the current distribution is like the single band antenna with the notable difference being that there is also current flow on the inside of the x-axis edges (i.e. along the width of the patch). In practice, this means the lower resonant frequency is determined not only by the length of the patch but also by length, width, and position of the slot. Since the electric field is strongest along the width of the patch (Figure 2-7) then the surface current along the x-axis edges generates only a minor shift in the lower resonance.

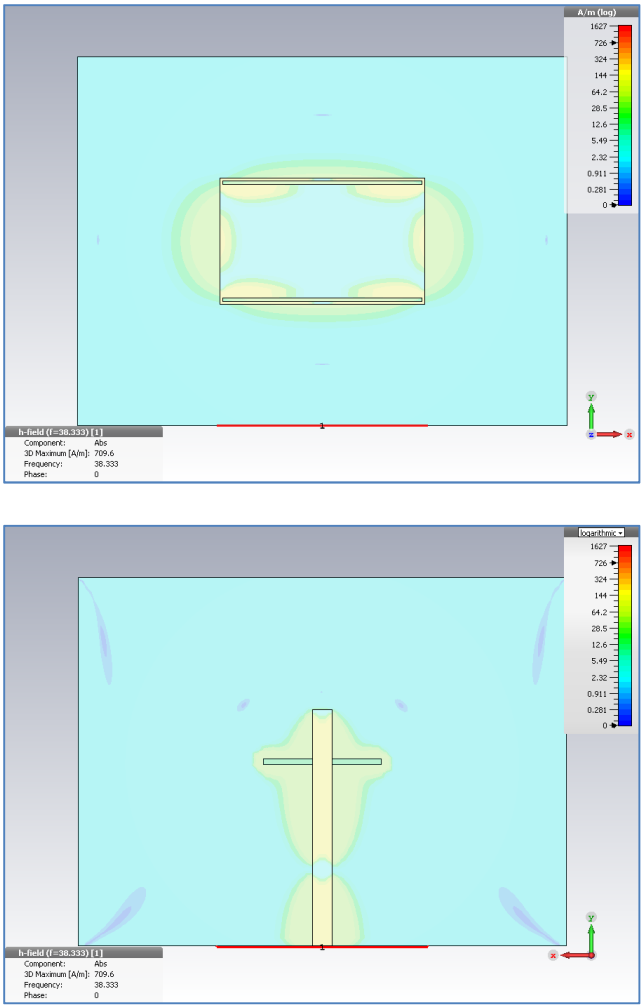

Figure 4-15: Dual Band Antenna Surface Current at 38 GHz (Phase = 0°)

At the upper resonance frequency, the current distribution is strongest on the inside of the x-axis edges (i.e. along the width of the patch) where the electric field is weakest. Observation of the current distribution around the slot reveals a null at the center of the slot, directly above the RF feed. APPENDIX B discusses a method to estimate the upper resonant frequency based on the current flow around the slot.

4.4 CST MWS Simulations of Phased Array

Table 4-3: Phase Array Simulation Dimensions

Array Type	Array Size	Spacing (mm)	Reference
Checkered Diamond	3x3	8 mm x 8 mm	Figure 3-9
Checkered Linear	4x1	8 mm x 4mm	Figure 3-10

4.4.1 Checkered Diamond 3x3 Array 3D Farfield Plots

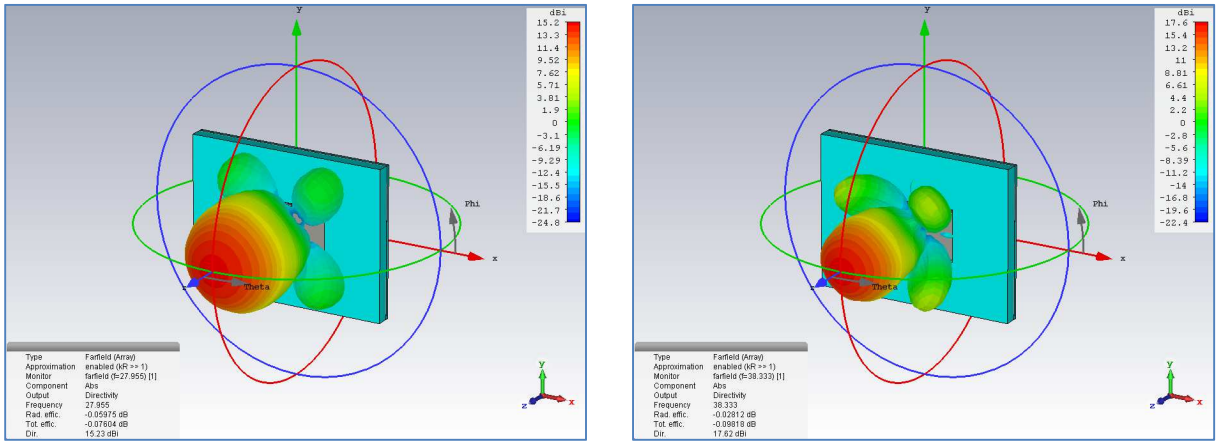

Figure 4-16: Checkered Diamond 3x3 Array 3D Farfield Plot at 28 GHz & 38 GHz

The checkered diamond array has caused the spherical radiation patter to become elongated, with the lower resonance having a directivity of 15.2 dBi and the upper resonance having a directivity of 17.6 dBi, both in the broadside. The radiation efficiency remains as was seen with the dual band antenna.

4.4.2 Checkered Diamond 3x3 Array 3D Polar Plots

For the lower resonance, the angular width (3db) is 31.3° and the side lobes are 15.9 dB lower than the main lobe for Phi = 45°. For the upper resonance, the angular width (3db) is

23.7° and the side lobes are 12.5 dB lower than the main lobe for Phi = 45°. The back lobes are as was seen in the dual band antenna. Although the separation between array elements is constant in the physical domain, it is a variable in the frequency domain. The lower resonance sees an electrical separation of 1/2 wavelength whereas the upper resonance sees an electrical separation of 1/3 wavelength. This is the reason the lower resonance has smaller directivity, better sidelobe suppression, and greater angular width.

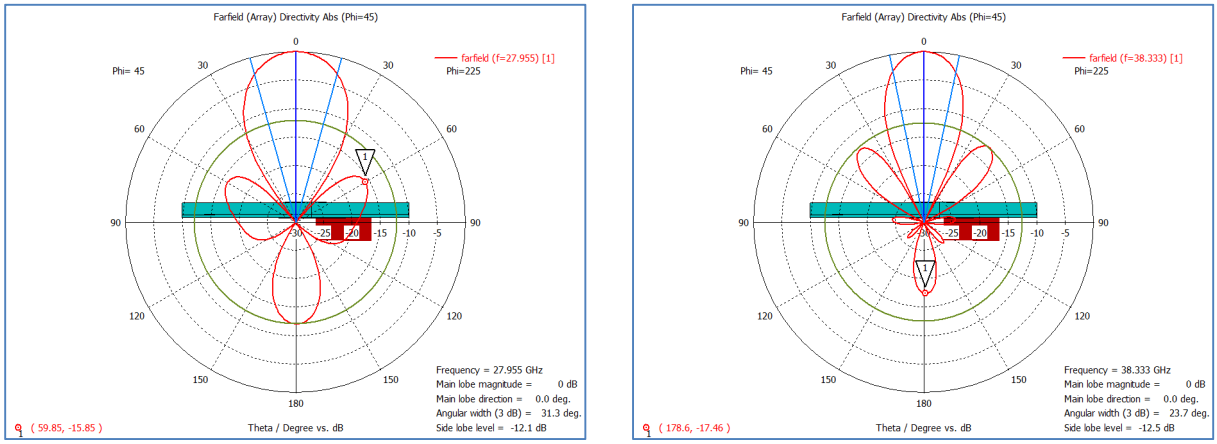

Figure 4-17: Checkered Diamond 3x3 Array Polar Plot at 28 GHz & 38 GHz, Phi = 45

4.4.3 Checkered 4x1 Array 3D Farfield Plots

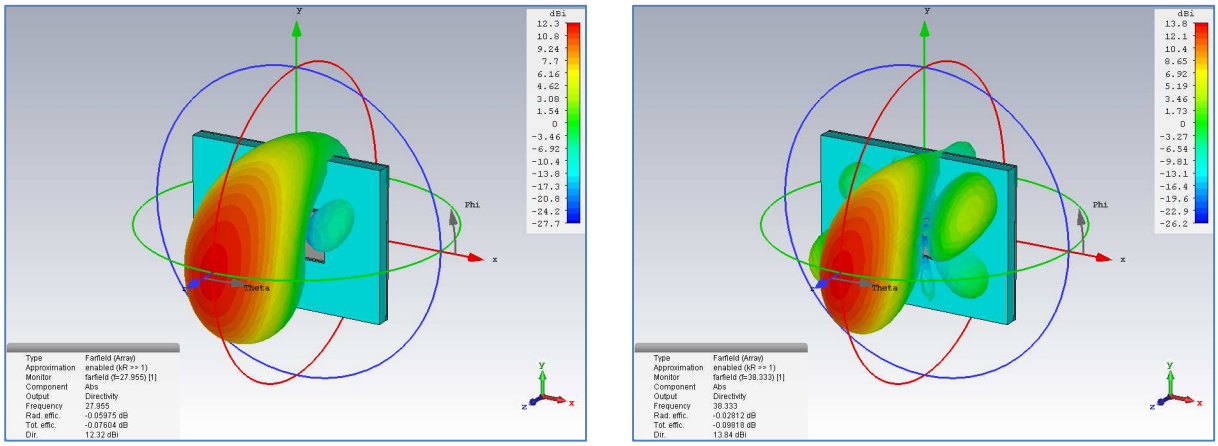

Figure 4-18: Checkered 4x1 Array 3D Farfield Plot at 28 GHz & 38 GHz

The linear array has caused the spherical radiation patter to become shaped like a disk, with the lower resonance having a directivity of 12.3 dBi and the upper resonance having a directivity of 13.8 dBi, both in the broadside. The radiation efficiency remains as was seen with the dual band antenna.

4.4.4 Checkered 4x1 Array Polar Plots

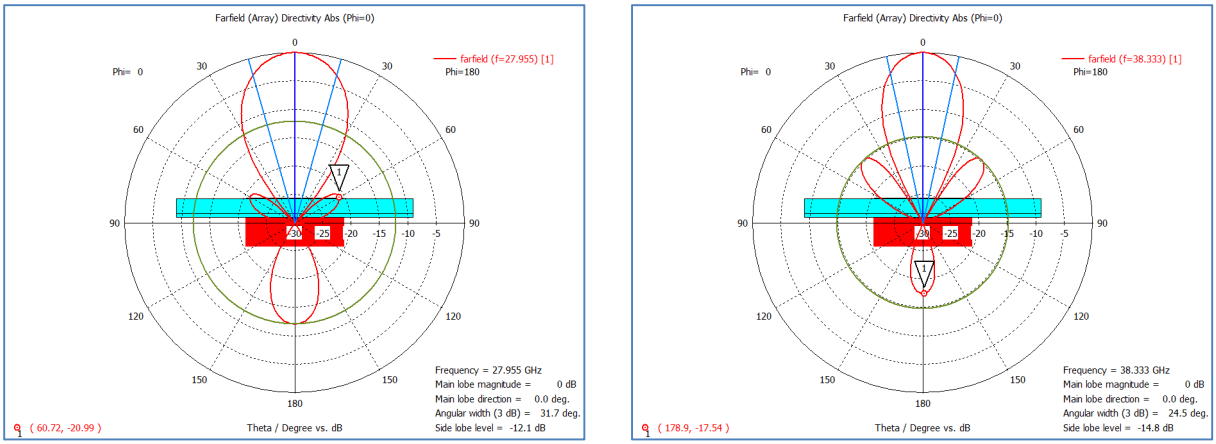

Figure 4-19: Checkered 4x1 Polar Plot at 28 GHz & 38 GHz, Phi = 0

For the lower resonance, the angular width (3db) is 31.7° and the side lobes are 20.9 dB lower than the main lobe for Phi = 0°. For the upper resonance, the angular width (3db) is 24.5° and the side lobes are 14.8 dB lower than the main lobe for Phi = 0°. The back lobes are as was seen in the dual band antenna.

4.5 CST MWS Simulations of RF Feed Network

The dfx files of the entire RF feed network were exported from AWR and then loaded in to CST MWS. Simulations were run using the parameters specified in Table 3-7.

4.5.1 RF Feed Network S-Parameters

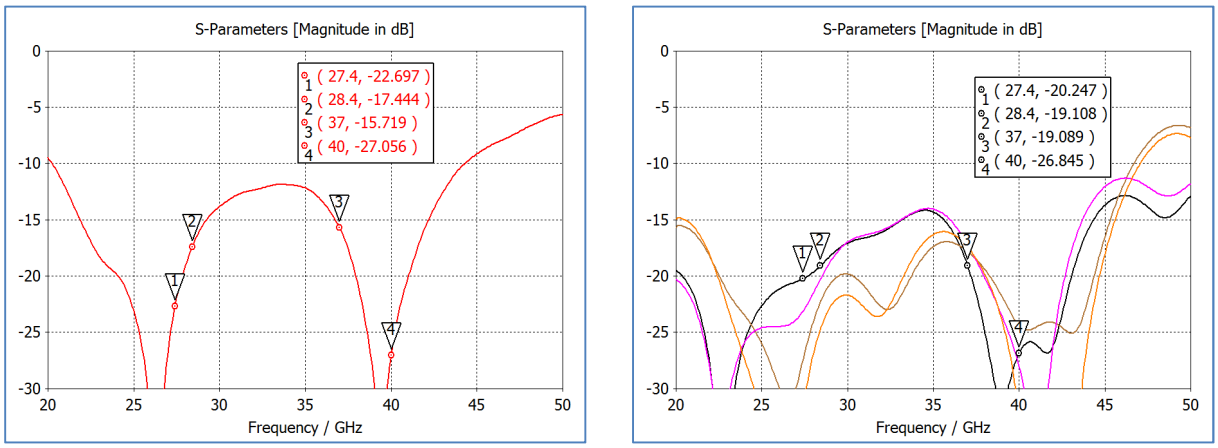

Figure 4-20: RF Feed Network Input & Output Return Loss

For both the lower and upper resonance, the input and output return loss of the RF feed network is better than 15 dB and therefore well matched to a 50-ohm system.

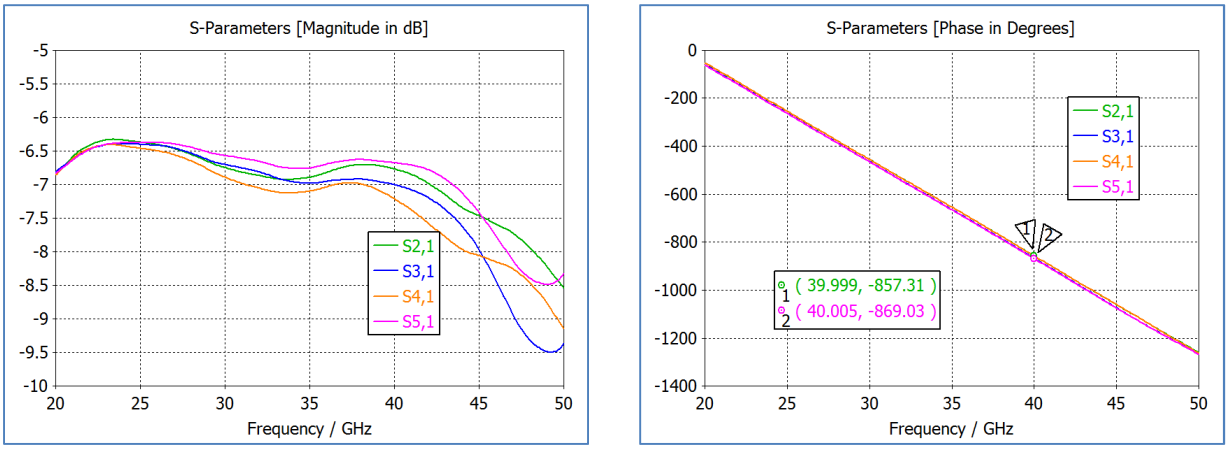

Figure 4-21: RF Feed Network Insertion Loss & Phase Difference

The difference in phase between each of the four paths is less than 12 degrees at 40 GHz, which is an error of 3.3% (12° ÷ 360°). Well within the established limit of λ/8 that enables sidelobe cancellation in a phased array [29].

4.5.2 RF Feed Network Z-Smith Chart

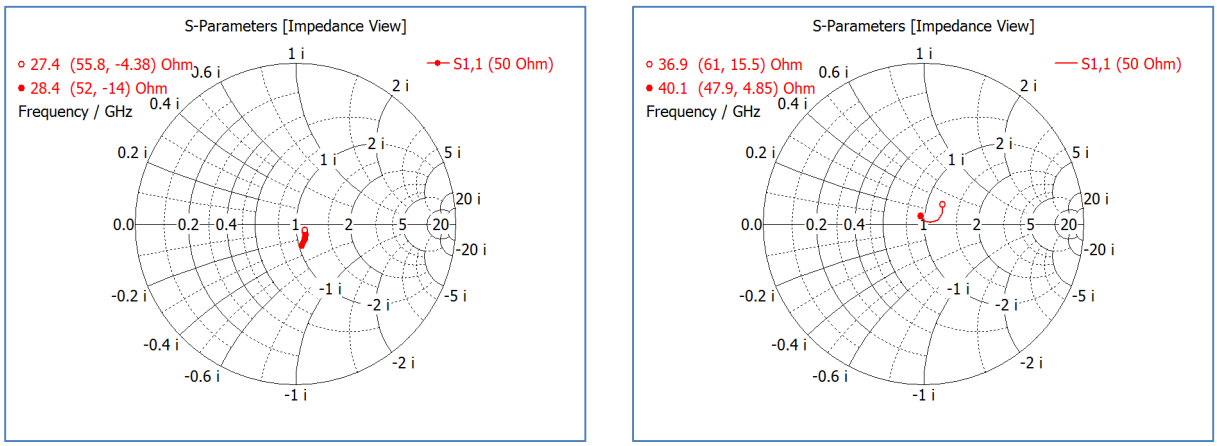

Figure 4-22: RF Feed Network Z-Smith Chart (Input) at 28 GHz & 38 GHz

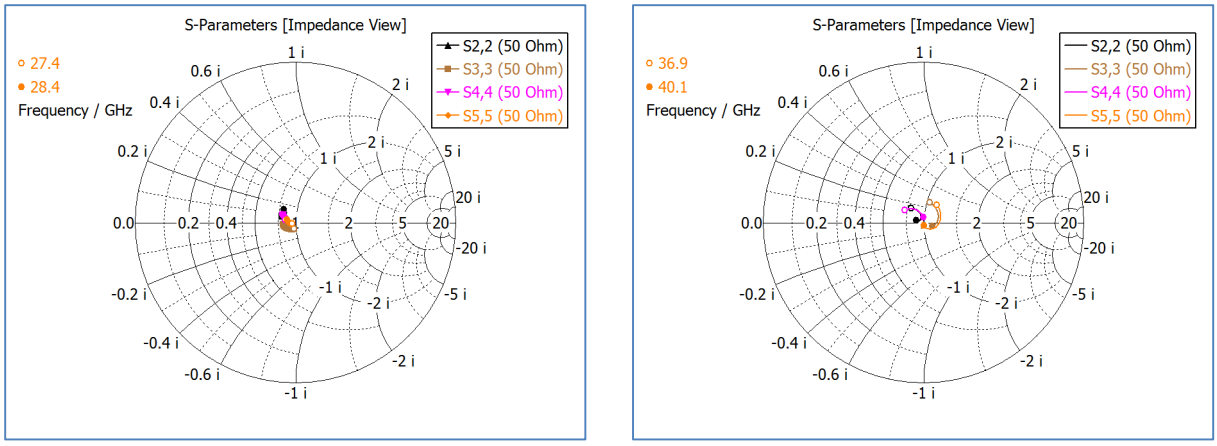

Figure 4-23: RF Feed Network Z-Smith Chart (Output) at 28 GHz & 38 GHz

For both the lower and upper resonance, the input and output impedance of the RF feed is close to the center of the Z-Smith Chart and therefore well matched to a 50-ohm system.

4.6 CST MWS Simulations of Checkered 4x1 Array with RF Feed Network

The simulations were run using the parameters specified in Table 4-2 in conjunction with the new (or updated) parameters specified in Table 4-4. The array elements are centered in the x-axis and offset +4 mm in the y-axis. The waveguide port is centered in the x-axis and offset from the edge of the substrate by +1.7 mm in the y-axis.

Table 4-4: Checkered 4x1 with RF Feed Simulation Dimensions

Parameter	Value	Parameter	Value
Substrate Width	20 mm	Substrate Length	20 mm

4.6.1 Checkered 4x1 Array with RF Feed S11 (Magnitude & Phase)

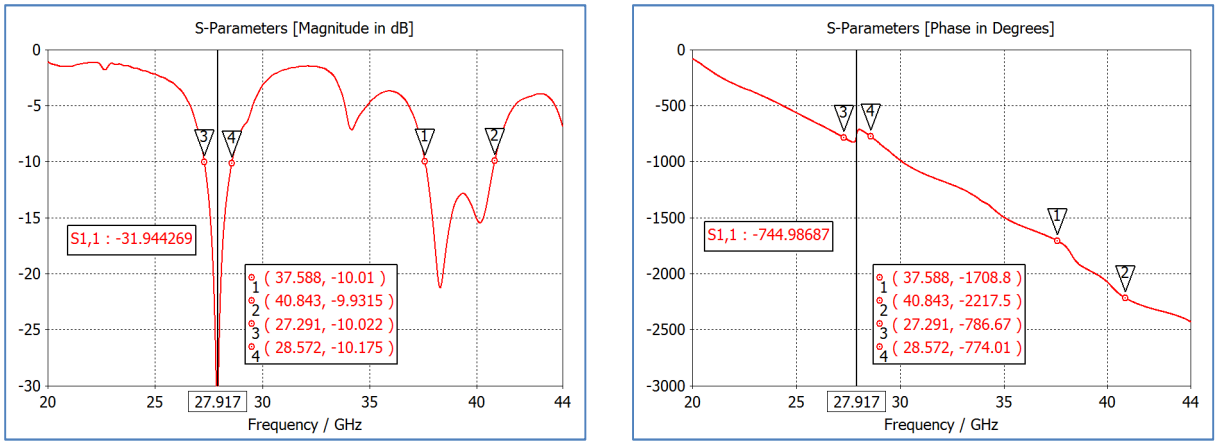

Figure 4-24: Checkered 4x1 Array with RF Feed S11 (Magnitude & Phase)

There are two resonant frequencies, one at 27.9 GHz and the other at 38.5 GHz. The lower resonance has a 10 dB return loss bandwidth of 4.1% and extends from 27.3 GHz to 28.5 GHz (slightly broader than the theoretical linear array). The upper resonance has a 10 dB return loss bandwidth of 8.2%, extends from 37.6 GHz to 40.8 GHz, and has shifted up by roughly 0.8

GHz due to the mutual coupling between the elements of the array. Also, there are dips at 34 GHz and 40 GHz which are cause by the RF feed network. The phase changes more rapidly at the resonant frequencies.

4.6.2 Checkered 4x1 Array with RF Feed 3D Farfield Plot

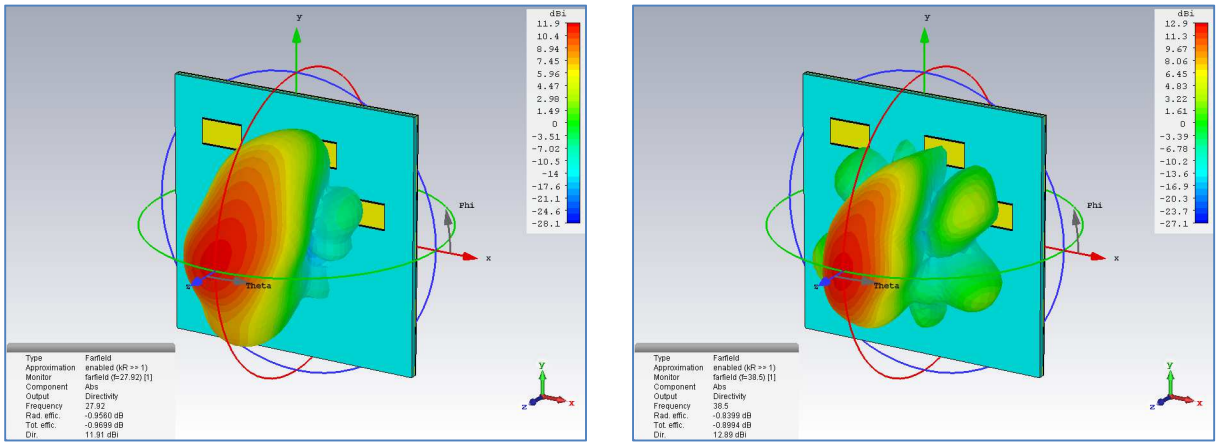

Figure 4-25: Checkered 4x1 Array with RF Feed 3D Farfield Plot

The radiation pattern is shaped like a disk as was the case with the theoretical linear array, with the lower resonance having a directivity of 11.9 dBi and the upper resonance having a directivity of 12.9 dBi, both in the broadside. At the lower resonance the radiation efficiency is 80.2% (-0.96 dB) and at the upper resonance the radiation efficiency is 82.4% (-0.84 dB), considerably worse than the theoretical linear array due to the losses in the RF feed network.

4.6.3 Checkered 4x1 Array with RF Feed Polar Plots

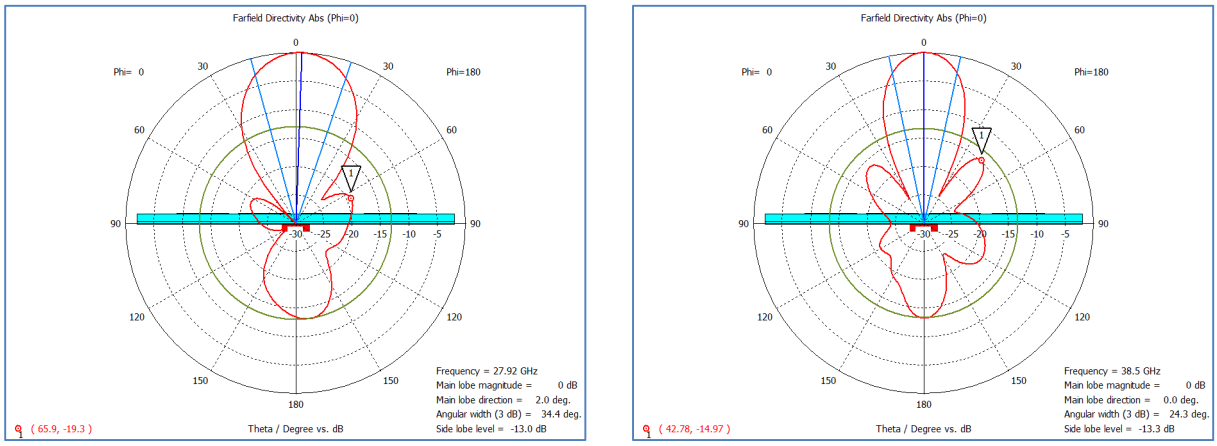

Figure 4-26: Checkered 4x1 Array w. RF Feed Polar Plots at 28 GHz & 38 GHz, Phi = 0

For the lower resonance, the angular width (3db) is 34.4° and the side lobes are 19.3 dB lower than the main lobe for Phi = 0°. For the upper resonance, the angular width (3db) is 24.3° and the side lobes are 14.9 dB lower than the main lobe for Phi = 0°. The overall performance is like the theoretical linear array, except for the back lobes which have taken-on an unsymmetrical pattern and are roughly 3 dB worse at the upper resonance. The strange shape of the back lobes is attributed to the RF feed network which includes several bends and three Wilkinson power dividers.

4.6.4 Summary of Simulation Results

A summary of the simulation results is given in Table 4-5. Implementing the slots reduces the efficiency and lowers the bandwidth of the lower resonance without impacting directivity or radiation pattern. The upper resonance is a perturbed third order mode but radiates like a first order mode. The performance of upper resonance is better than the lower resonance.

Table 4-5: Summary of Simulation Results

Parameter		Single Band	Dual Band	Checkered 4x4 Array	Linear 4x1 Array	Linear 4x1 Array RF Feed
Resonance Due to Patch						
Resonance	---	31.8 GHz	27.9 GHz	---	---	27.9 GHz
BW	---	8.2%	3.2%	---	---	4.1%
Radiation Pattern	---	Sphere	Sphere	Elongated Sphere	Disk	Disk
Directivity	---	7.1 dBi	7.1 dBi	15.2 dBi	12.3 dBi	11.9 dBi
Radiation Efficiency	---	99.3%	98.6%	98.6%	98.6%	80.2%
Back Lobe	---	-14.7 dB	-12.1 dB	-12.1 dB	-12.1 dB	-13 dB
3 dB BW	Phi = 00	72.9°	70.1°	---	31.7°	34.4°
	Phi = 45	---	---	31.3°	---	---
	Phi = 90	84.0°	87.9°	---	---	---
Side Lobe	---	---	---	-15.9 dB	-20.9 dB	-19.3 dB
Resonance Due to Slots						
Resonance	---	N.A.	38.5 GHz	---	---	38.5 GHz
BW	---	N.A.	7.9%	---	---	8.2%
Radiation Pattern	---	N.A.	Sphere	Elongated Sphere	Disk	Disk
Directivity	---	N.A.	7.1 dBi	17.6 dBi	13.8 dBi	12.9 dBi
Radiation Efficiency	---	N.A.	99.3%	99.3%	99.3%	82.4%
Back Lobe	---	N.A.	-17.5 dBc	-17.5 dBc	-17.5 dBc	-13.3 dBc
3 dB BW	Phi = 00	N.A.	81.6°	---	24.5°	24.3°
	Phi = 45	---	---	27.3°	---	---
	Phi = 90	N.A.	88.3°	---	---	---
Side Lobe	---	N.A.	---	-15.9 dBc	-20.9 dBc	-19.3 dBc

CHAPTER 5

MEASUREMENT RESULTS & COMPARISON

5.1 Fabrication

The antenna has extremely fine features that are difficult to fabricate. The center of the resonant slots relative the respective outer edges of the patch are specified to by 71 microns in the y-axis. Figure A-10, in Appendix A, indicates both the upper and lower resonance will shift by as much a 0.5 GHz if the position of the resonant slot is off by as little 10 microns. For perspective, the width of a human hair is ~ 20 to 150 microns. A laser etcher, such as the LPKF Proto Laser S4, can achieve an accuracy of +/-2 microns; however, the heat associated with the process of stripping away copper will cause a thin laminate to bow and twist rendering the final product useless. Leading edge PWB suppliers, such as TTM, Sanmina, and Aspocomp, can achieve an accuracy of +/- 20 microns with their plating process on 1/3 oz. copper without galvanic plating. However, observation of Figure 5-1 clearly illustrates the challenges these PWB suppliers encounter when etching such fine features into copper.

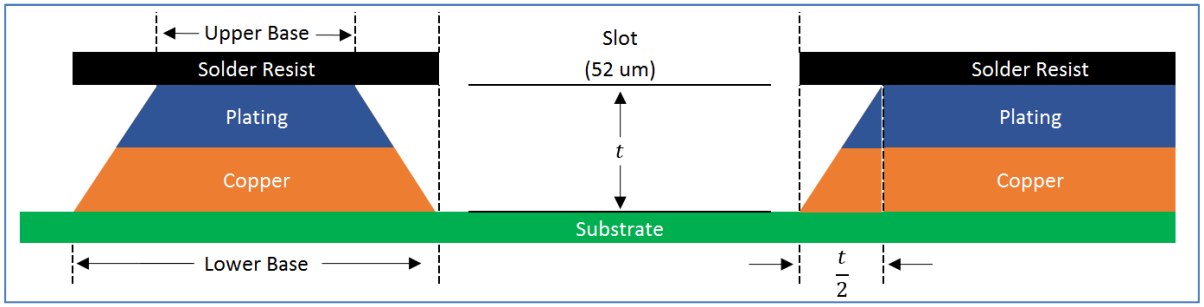

Figure 5-1: Typical Etching Characteristics. Adapted from [30].

Consider that the thickness of the 1/3 oz. copper is 12 microns and, when following IPC standards, the thickness of the galvanic plating is 20 microns, yielding a total copper & plating thickness of 32 microns. Thus, as per the slope shown in Figure 5-1, the width of the conductor base must be 32 microns larger than the width of the conductor top. This is a substantial difference in comparison to the specified width of the resonant slot (52 microns). And, since the center of the resonant slot is specified to be 71 microns from the edge of the patch, then the width of the lower base must be 45 microns and the width of the upper base must be 13 microns (which is outside their accuracy of +/- 20 microns).

Ultimately, the antenna was fabricated by Aspocomp, located in Oulu, Finland, with the agreement to violate IPC standards (for this proto antenna only) and radically down etch the 1/3 oz. copper to ~5 microns before implementing a galvanic plating of thickness of ~13 microns (yielding a total copper & plating thickness of ~17-20 um) [31]. A magnified photograph of the etched radiator is given in Figure 5-2.

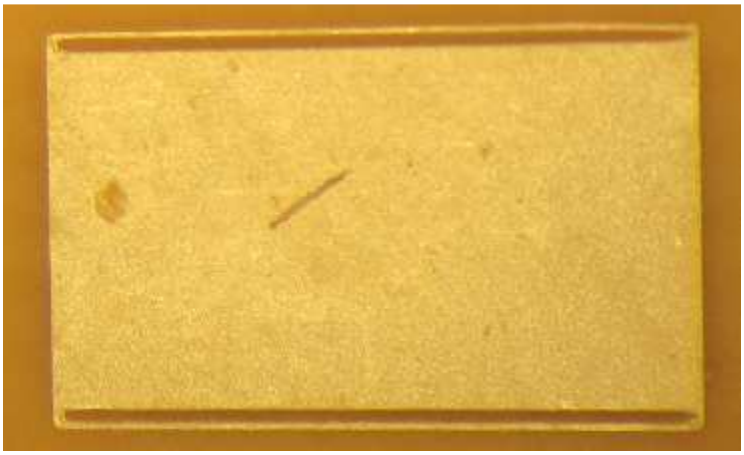

Figure 5-2: Photograph of Etched Radiator

5.2 Test Set Up

The performance of the aperture fed antenna, the dual band antenna, and the linear array was characterized at the Nokia facilities in Irving, Texas. Return loss was measured using the Keysight N5245A PNA-X Microwave Network Analyzer (10 MHz to 50 GHz). A laser level was used to manually align the x-y plane of the antenna prior to collecting radiation patterns inside an anechoic chamber. The path losses in the set-up were determined using horn antennas whose characteristics where well known. The CW signal was generated by the Keysight E8267D PSG Vector Signal Analyzer (250 kHz to 44 GHz) and received by the Keysight N9030A PXA signal Analyzer (3 Hz to 50 GHz).

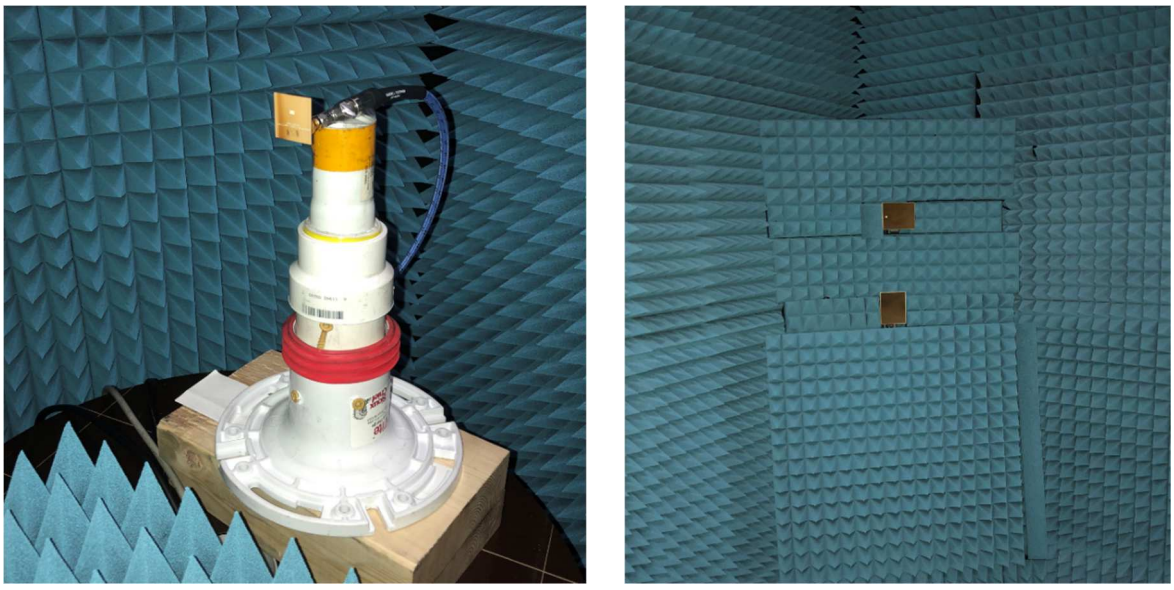

Figure 5-3: Photograph of Anechoic Chamber (Antenna & Receiving Horn)

5.3 Photographs of the Radiators

Pictures of the radiators are presented below. In Figure 5-5 and Figure 5-6, although not visible in the photograph, the resonant slots are present within the patch.

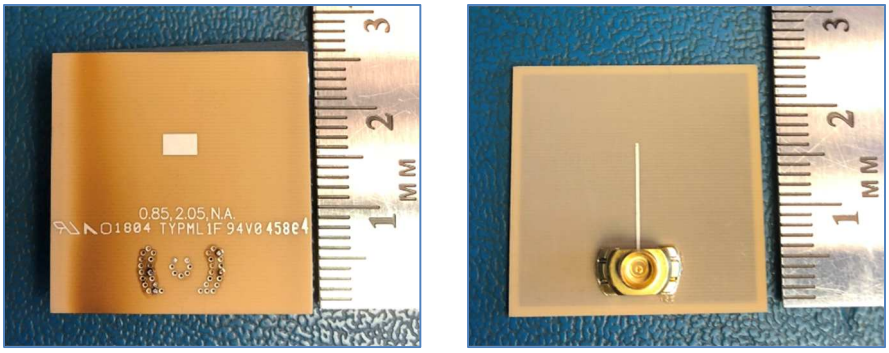

Figure 5-4: Photograph of Aperture Fed Microstrip Patch Antenna

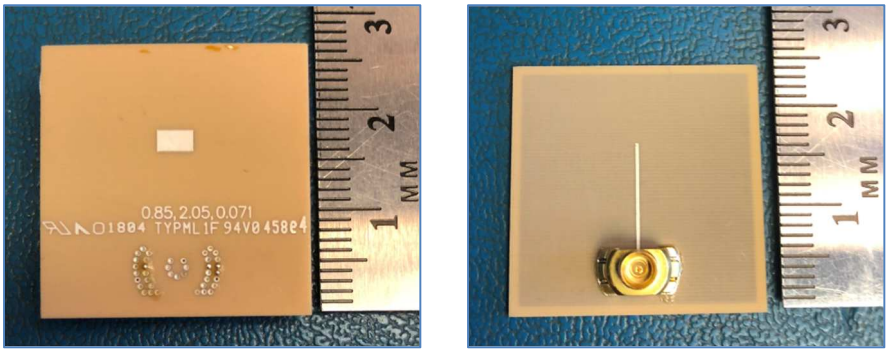

Figure 5-5: Photograph of Dual Band Microstrip Patch Antenna

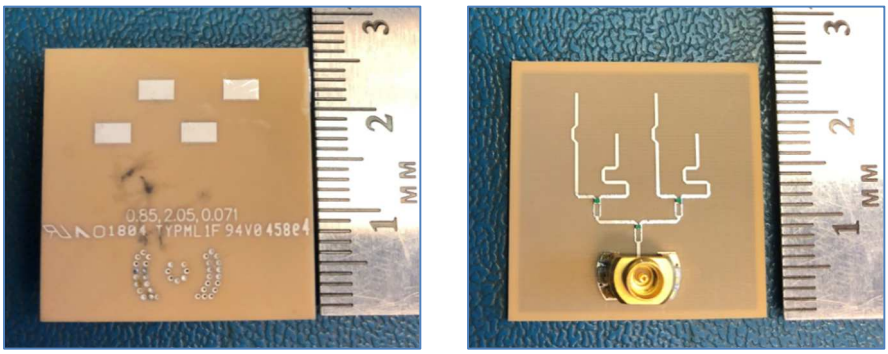

Figure 5-6: Photograph of Linear Array

5.4 Aperture Fed Microstrip Patch Antenna

Figure 5-7 compares the simulated S11 from Chapter 4 to the measured S11. A few differences are observed, namely the realized antenna has a double resonance at 32 GHz which creates a wider bandwidth. Consequently, the simulated model was updated so that the dimensions of the substrate (and the ground plane) matched the size of the fabricated radiators at 25 mm by 25 mm. Additionally, to align with their respective locations on the fabricated antenna, changes were made to the location of the patch (shifted from the center of the substrate by 3.5 mm in the y-axis) and the location of the RF feed point (shifted from the edge of the substrate by 4.5 mm in the y-axis). However, these changes alone were not enough to generate a match between the simulation and the realized radiator.

Ultimately, and as shown in Figure 5-8, a decent correlation was produced after implementing a discrete port and the Frequency Domain Solver in conjunction with auto-meshing feature. Now both curves show a double resonance in the operating band and a shallow resonance at roughly 38 GHz. The measured resonance at 31 GHz is generated by the patch antenna, and shows up at a slightly lower frequency in the improved simulation. The resonances at 32 GHz and 38 GHz do not appear in the simulation results when using a waveguide port, and are a result of the discrete port which has an inductance proportional to the distance between the RF trace and the ground plane. Since the discrete port feed behaves like an RF connector, then the differences at these resonances is attributed to the modeling, or lack thereof, of the RF connector. A better correlation can be achieved with either solver if an accurate model of the RF connector is introduced into the simulation.

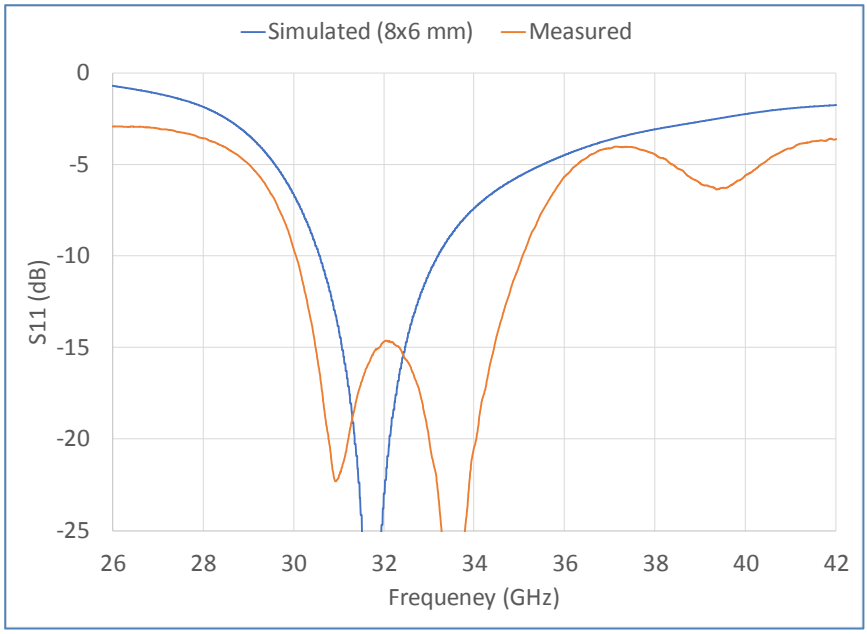

Figure 5-7: Aperture Fed Antenna (8x6mm), Simulated vs. Measured, S11 (dB)

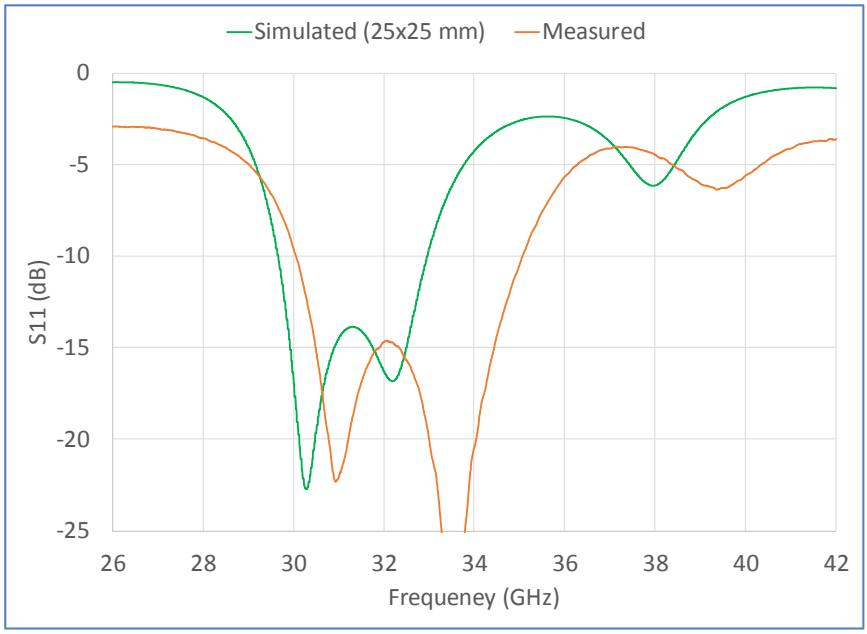

Figure 5-8: Aperture Fed Antenna (25x25mm), Simulated vs. Measured, S11 (dB)

The resonances at 32 GHz and 38 GHz are also a result of the position of the discrete port relative to the aperture of the antenna. S11 versus feed position is illustrated in Figure 5-10 for a waveguide port and in Figure 5-11 for a discrete port. The blue line represents a feed placed 4.5 mm from the edge of the substrate (11.5 mm from the center of the aperture). The green line represents a feed placed 14.5 mm from the edge of the substrate (3.5 mm from the center of the aperture). As the discrete port feed moves closer to the center of the aperture, the dips at 32 GHz and 38 GHz start to disappear. The inductance of the discrete port feed has created an impedance mismatch with the antenna, resulting in a standing wave on the feed line. The resonances at 32 GHz and 38 GHz are a result of the standing waves.

The radiation pattern associated with 25x25 mm substrate is given in Figure 5-9. When compared to the radiation pattern in Figure 4-4, there is now ripple.

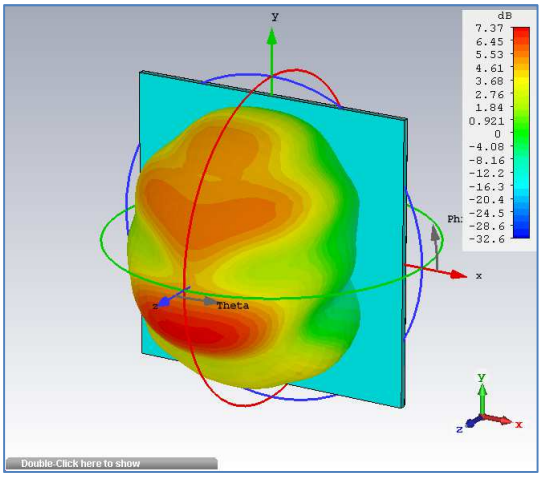

Figure 5-9: Aperture Fed Antenna (25x25mm) 3D Farfield Plot

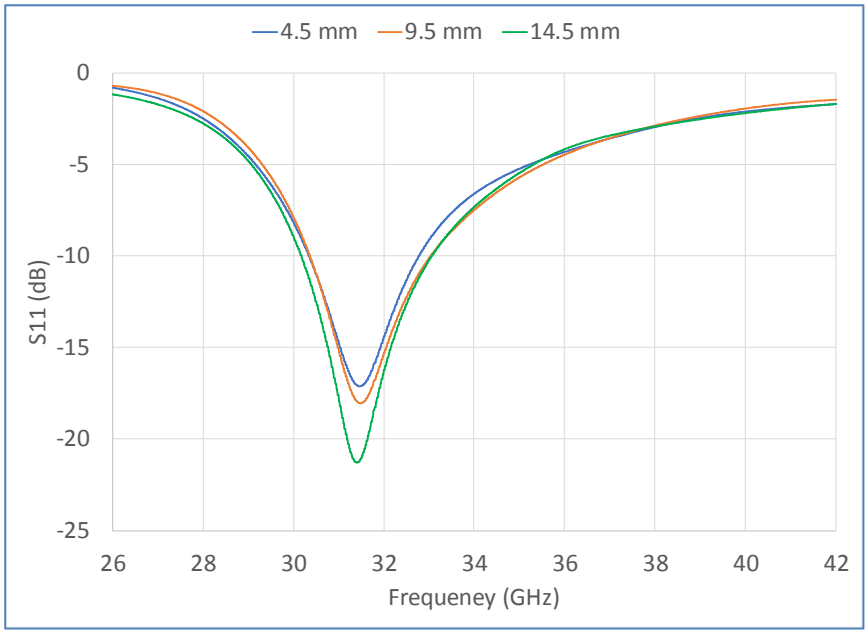

Figure 5-10: Aperture Fed Antenna (25x25mm), S11 (dB) vs. Feed Position, Waveguide Port

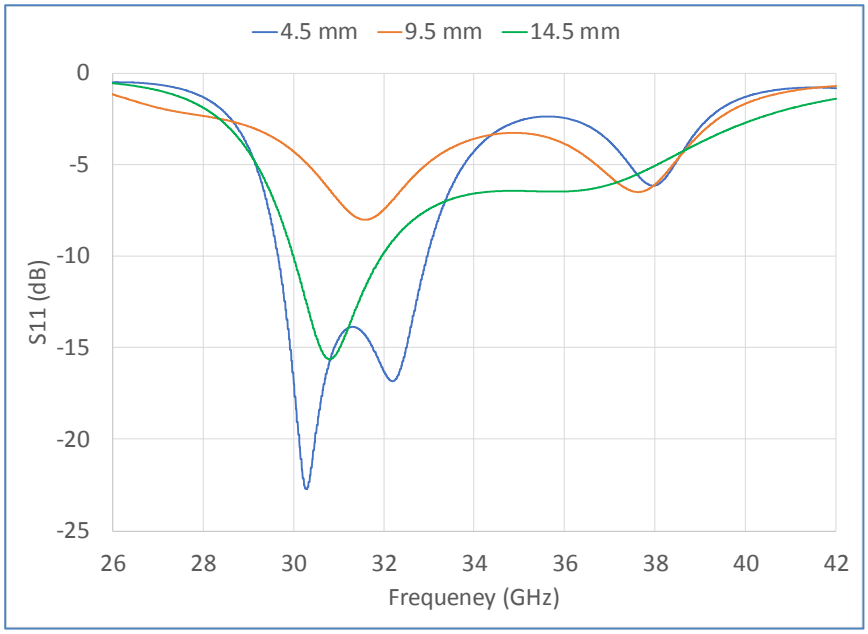

Figure 5-11: Aperture Fed Antenna (25x25mm), S11 (dB) vs. Feed Position, Discrete Port

It was initially speculated the flat top in the measurement data of Figure 5-12 was due to saturation of the test equipment. However, it was soon realized that a flat top could be generated in the simulation by enlarging the substrate (and without implementing a discrete port feed or auto meshing). The substrate is so electrically large and thick that there are reflections which generate constructive and destructive interference, and the impact is seen in both the simulated and measured results.

Since the radiator was aligned manually in the anechoic chamber, then it was not aligned perfectly in either the x, y, or z-axis. There is a mismatch of roughly +11°. The results were adjusted and this can be seen in the bottom left corner of Figure 5-12, where there is a gap in the data between theta equals -79° and -90°. Imperfect alignment also explains the peak gain difference since a tilted antenna will not radiate max power in the direction of the receiving horn antenna. This can be seen in Figure 5-9.

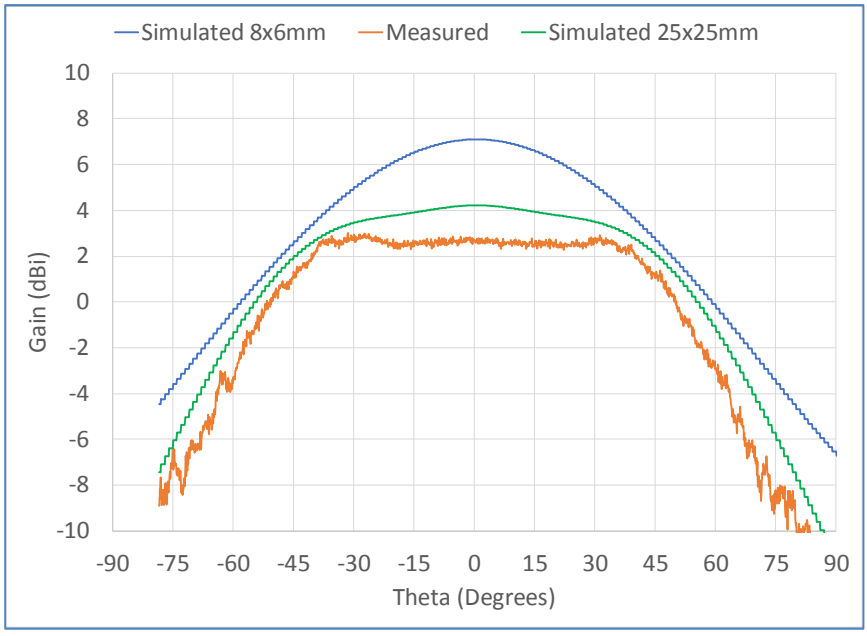

Figure 5-12: Aperture Fed Antenna, Simulated vs. Measured, Cartesian Plot, Phi = 0

5.5 Dual Band Microstrip Patch Antenna

The simulated 3D radiation patterns of the dual band antenna using 25x25 mm substrate are given in Figure 5-13. When compared to the radiation patterns using 8x6 mm substrate given in Figure 4-11Figure 4-4, there is now ripple due to surface waves in the electrically large upper substrate.

A comparison of the simulated to measured S11 is given in Figure 5-14 and Figure 5-15. Standing waves and the associated nulls are seen in the updated simulation results.

The lower and upper radiation patterns are shown in Figure 5-16 and Figure 5-17. The measured data has been adjusted by -4.5° for the lower resonance and +3.0° for the upper resonance. The flat top is again present due to constructive and destructive interference. The difference in gain is due to imperfect alignment of the antenna within the anechoic chamber during testing. Although not shown in Figure 5-17, the simulation results indicate the upper resonance becomes flatter as the patch moves closer to the upper edge of substrate.

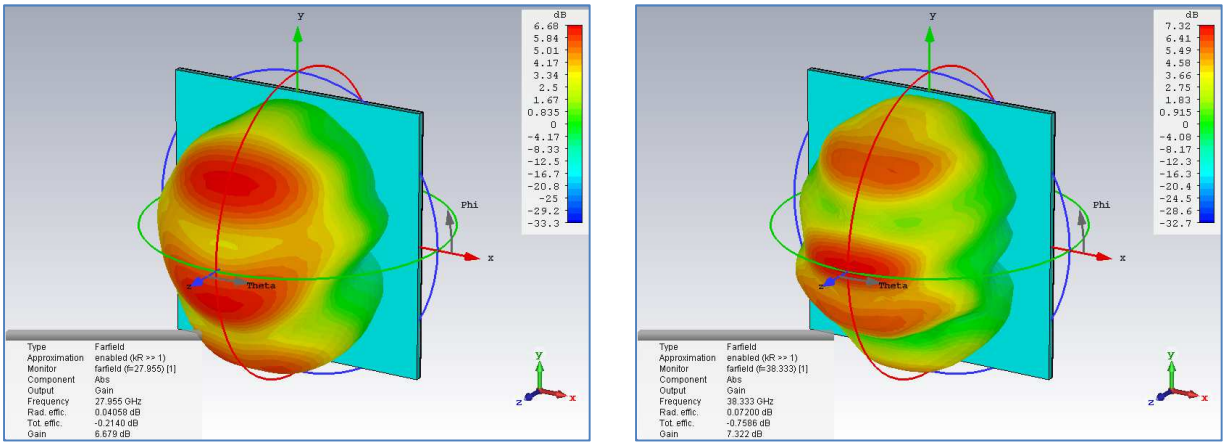

Figure 5-13: Dual Band Antenna (25x25mm) 3D Farfield Plot

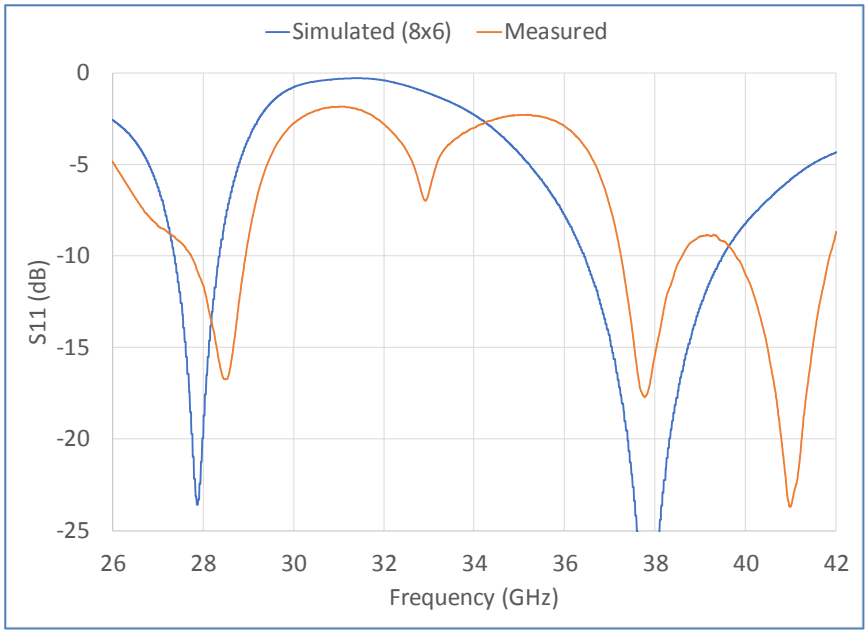

Figure 5-14: Dual Band Antenna (8x6mm), Simulated vs. Measured, S11 (dB)

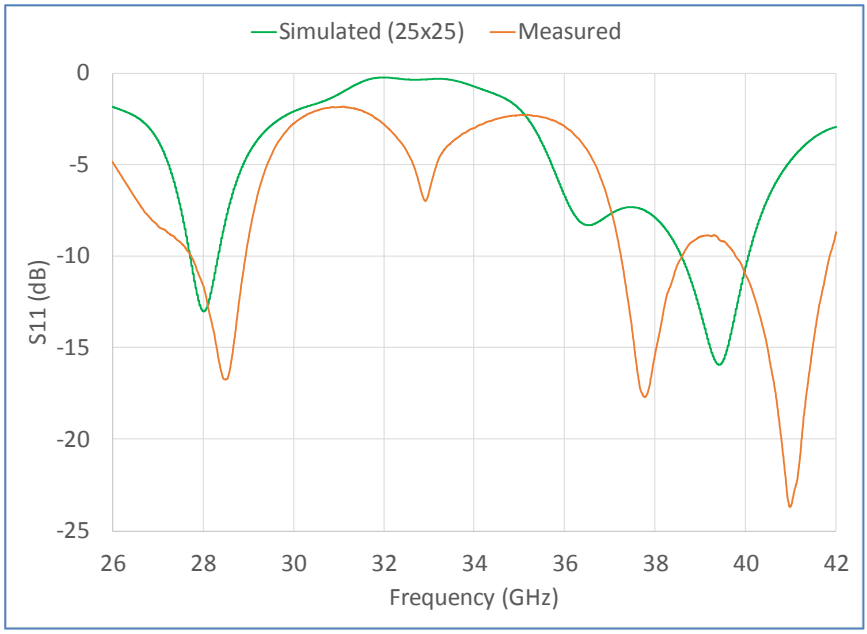

Figure 5-15: Dual Band Antenna (25x25mm), Simulated vs. Measured, S11 (dB)

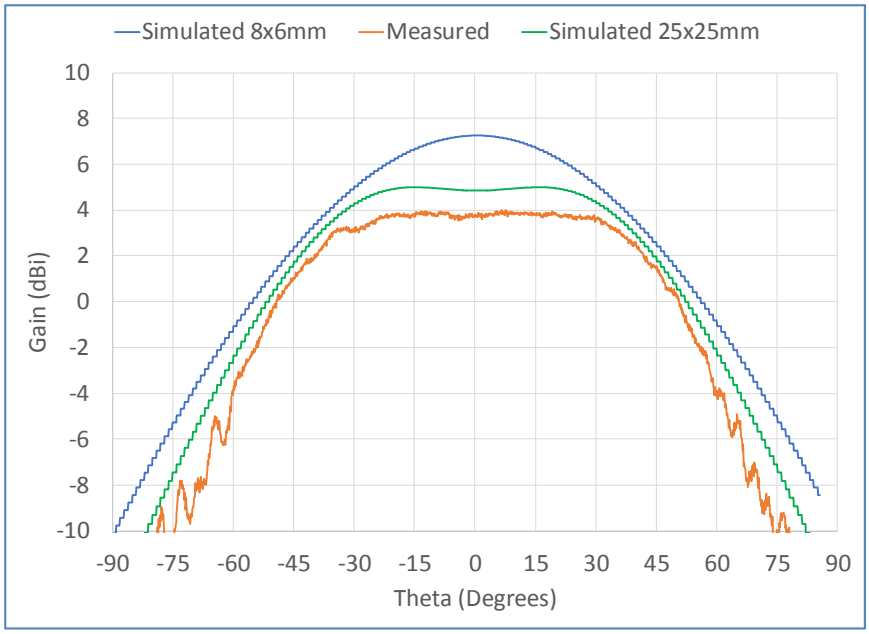

Figure 5-16: Dual Band Antenna, Simulated vs. Measured, Cartesian Plot at 28 GHz, Phi = 0

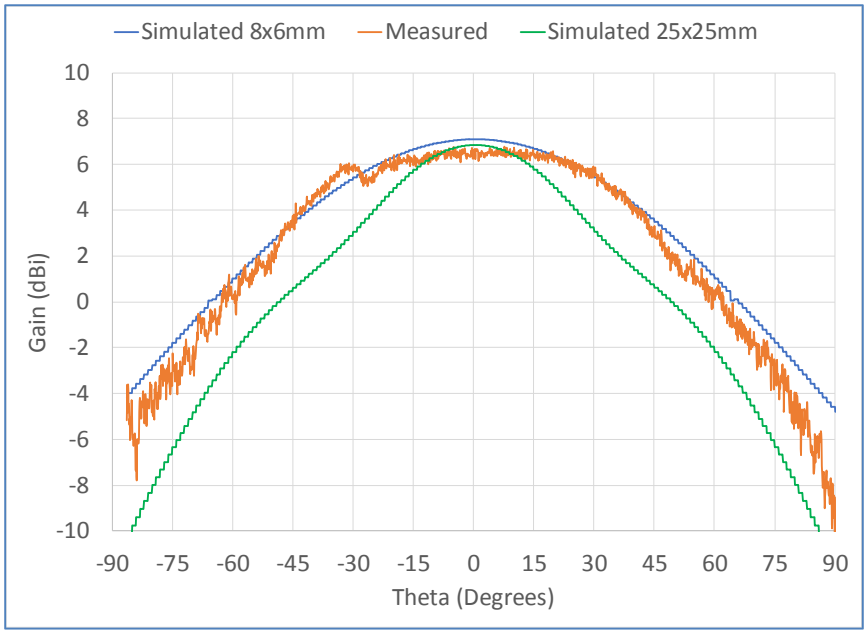

Figure 5-17: Dual Band Antenna, Simulated vs. Measured, Cartesian Plot at 38 GHz, Phi = 0

5.6 Linear Array

The simulated 3D radiation pattern of the linear array using 25x25 mm substrate is given in Figure 5-18, and is not much different than the radiation patterns shown in Figure 4-25 since the initial model used a 20x20 substrate.

A comparison of the simulated to measured S11 is given in Figure 5-19 and Figure 5-20. As can be seen in Figure 5-6, the RF feed is of enough length to create standing waves and the associated nulls are seen in the initial simulation results.

A comparison of the simulated to measured radiation patterns is given in Figure 5-21 and Figure 5-22. The measured data has been adjusted by -4.5° for the lower resonance and by +3.0° for the upper resonance. There is a small difference in gain that is due to a small misalignment of the antenna within the anechoic chamber during testing. The flat top is no longer present as the additive nature of the array dominates the radiation pattern.

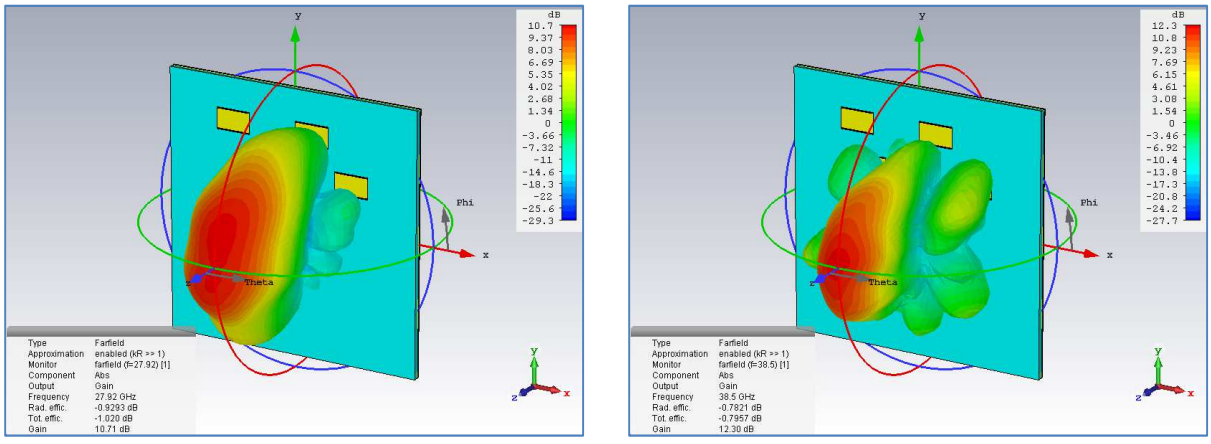

Figure 5-18: Linear Array with RF Feed (25x25mm) 3D Farfield Plot

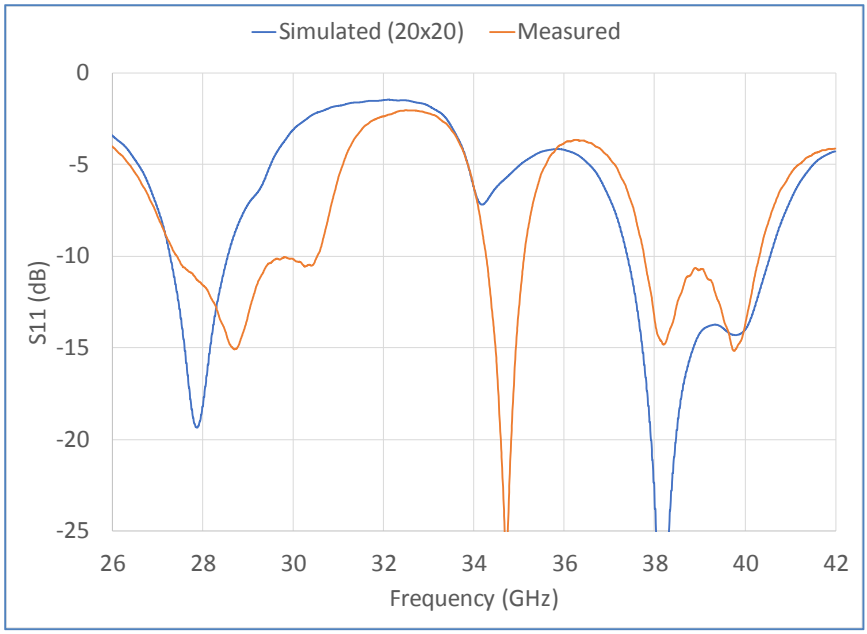

Figure 5-19: Linear Array (20x20mm), Simulated vs. Measured, S11 (dB)

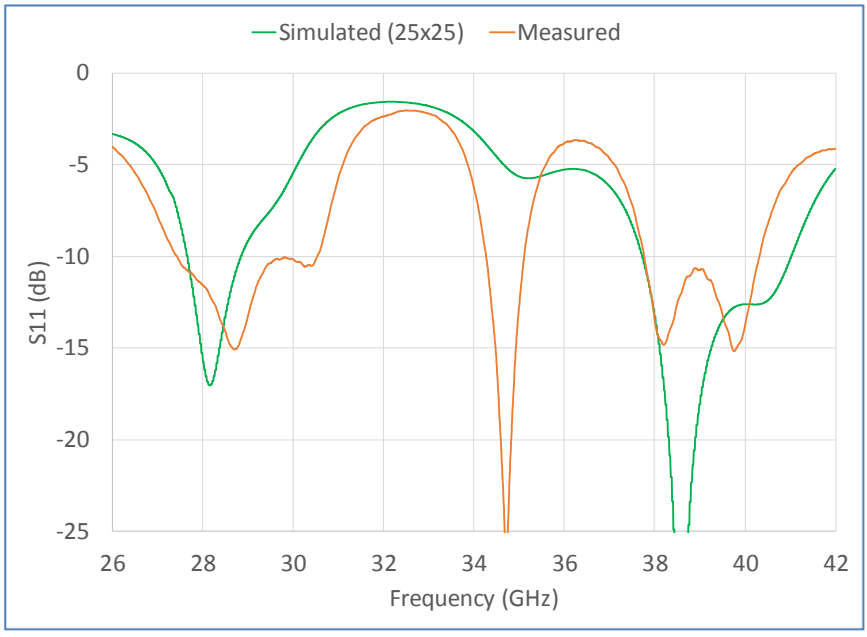

Figure 5-20: Linear Array (25x25mm), Simulated vs. Measured, S11 (dB)

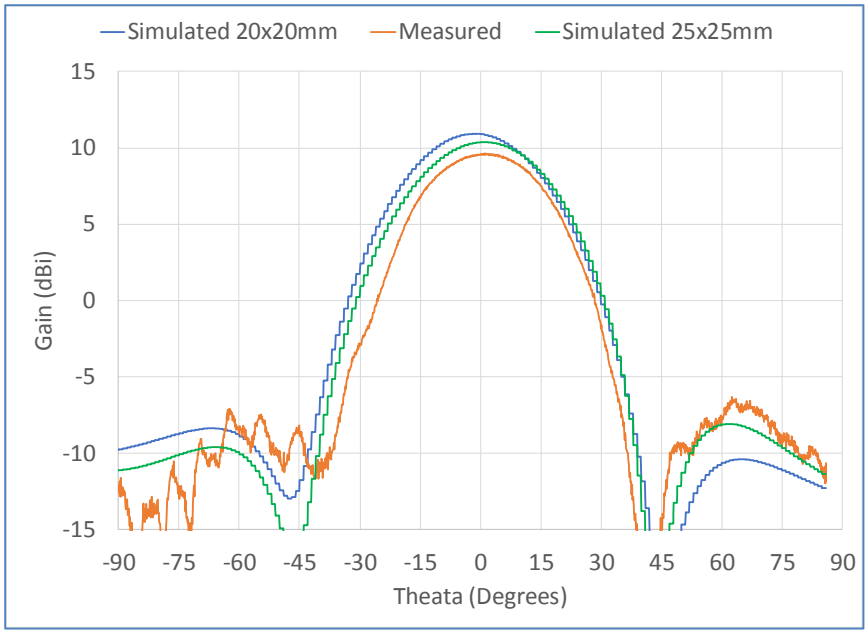

Figure 5-21: Linear Array, Simulated vs. Measured, Cartesian Plot at 28 GHz, Phi = 0

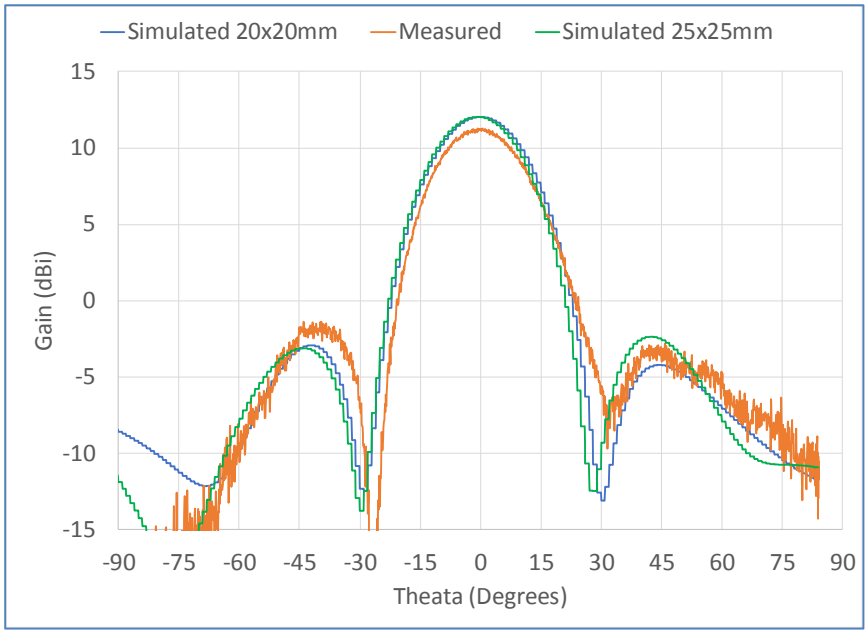

Figure 5-22: Linear Array, Simulated vs. Measured, Cartesian Plot at 38 GHz, Phi = 0

CHAPTER 6

CONCLUSION AND RECOMENDATIONS

6.1 Conclusion and Learnings

This work achieved the overall objective of investigating the feasibility of a dual band millimeter wave microstrip antenna and the associated phased array, applicable to the fifth-generation mobile communication systems in the USA.

During the design phase, a modified equation for predicting patch length and an approximation for predicting upper resonance frequency of the dual band antenna was formulated. It was noted that an aperture fed antenna with resonant slots excited in the TM_{01} mode enables an upper to lower resonance ratio that is smaller than that of a pin fed antenna with resonant slots excited in the TM_{10} mode. The bandwidth of the aperture antenna can be greater than that of a pin fed antenna, since the thickness of the upper substrate is not limited by the inductance associated with the feeding mechanism.

During the simulation phase, a parametric analysis was completed showing that some of the slot dimensions are sensitive to a movement as small as +/ -0.01 millimeters and that, aside from the slot, the most sensitive antenna dimensions are patch length, stub length, and aperture length. It was illustrated that a checkered diamond array pattern can minimize side lobes in two distinct operating bands. The depth of the miters and the number of bends are both significant when trying to match phase in the RF feed network. For an aperture fed antenna, it was noted that when feeding the elements from opposite directions the input signals need be 180° out of phase to get proper constructive and destructive interference in the radiation pattern. Resonant

slots etched near the edge of the patch significantly shift the 3rd order resonance and reduce the bandwidth of the lower resonance.

The fabrication process illustrated the etching capability limits of modern PWB suppliers and there are few companies that can etch features in copper that are smaller than the width of a human hair. Due to the extremely tight dimensional specifications of the resonant slots that occur at millimeter wave frequencies, it was determined that the resonant slot approach to dual band radiators is not practical for volume production.

The measurement results illustrated the significance of surface waves in an electrically large substrate and the associated impact to radiation patterns. The results also demonstrate the importance of modeling the RF connector at millimeter wave frequencies, since the associated inductance will shift the impedance locus of the antenna into the inductive area of the Smith chart causing unexpected ripples in the input return loss. These results show the significance of standing waves in an electrically long RF trace and how the associated resonances affect the input return loss. Small misalignments of the antenna within the anechoic chamber will cause the radiation patterns to indicate less than expected gain.

Reconciliation of the simulation results with reality revealed the differences between the waveguide port and the discrete port. To cross-check the accuracy of the Frequency Domain Solver, the final model was also simulated using the Time Domain Solver in conjunction with auto-meshing. The results matched; however, the simulation time was more than six hours. The Frequency Domain Solver is faster than the Time Domain Solver and is a good choice for future design activities.

6.2 Potential Future Work

Future research possibilities include the development a feed network for the checkered diamond array using a strip line feed, determining the exact equations for predicting the upper resonance, proper modeling of the RF connector (or via feed), and development of an aperture (i.e. bowtie, bone, diamond, etc.) that will broaden the lower resonance without narrowing the upper resonance or increasing back lobe radiation level.

Although PWB suppliers are not able to etch the fine features of the resonant slots, there are alternative technologies such as IC fabrication that easily achieve a tolerance of +/- 1 micron in their process. The approach taken in this thesis might find application in other areas.

APPENDIX A

EUQATION FOR PATCH LENGTH

Patch length is typically estimated using a widely known empirically developed equation that is given in engineering text books such as Balanis [4, p. 791] or Bankfrokft [9, p. 61]. For a resonant frequency of 31.8 GHz, an effective permittivity of 2.59, and a fringing length of 0.241 mm; the patch length is calculated as follows:

Equation A-1

$$L = \frac{c}{2(f_r)_{01}\sqrt{\epsilon_{effu}}} - 2\Delta L = 2.447\ mm$$

The resonance associated with a patch length of 2.447 mm lands at 27.9 GHz in the CST MWS simulation (Figure A-1) and is substantially less than the expected 31.8 GHz, an error of 12.3%. Upon inspecting above equation with the realization that *L* must be smaller to generate a higher resonance, it is obvious that either the fringing length is larger than calculated or the effective permittivity is larger than calculated (since the resonant frequency and the speed of light are fixed).

It was observed that, since ε_r is larger than ε_{eff}, using the relative permittivity in place of the effective permittivity leads to a more accurate prediction of patch length. This was also observed by Kai Fong Lee and Wei Chen. They wrote, "This formula is often used in the literature with ε_{eff} instead of ε_r. The original reference by Hammerstad [23] does not make it clear which is correct, since no formula for resonance frequency is given there. However, in our comparisons with measurements and the results from James (discussed below) we have obtained more accurate results by using ε_r" [21, p. 232]. Hence, using ε_r the patch length is calculated as follows:

Equation A-2

$$L = \frac{c}{2(f_r)_{01}\sqrt{\epsilon_r}} - 2\Delta L = 2.241\ mm$$

The resonance associated with a patch length of 2.241 mm lands at 29.8 GHz; an error of 6.2% (Figure A-1).

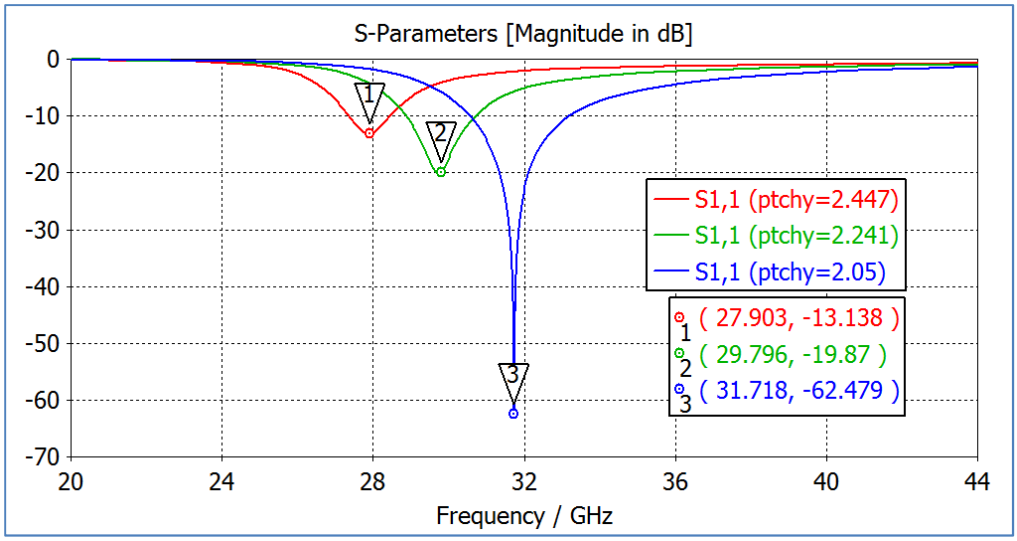

Figure A-1: Resonant Frequency versus Patch Length

Continuing with this idea, it was observed by this author that further modifying the equation, so that the relative permittivity is multiplied by the relative permittivity normalized by effective permittivity, leads to an extremely accurate prediction of patch length. Hence, using $(\varepsilon_r/\varepsilon_{effu}) * \varepsilon_r$ the patch length is calculated as follows:

Equation A-3

$$L = \frac{c}{2(f_r)_{01}\sqrt{\left(\frac{\epsilon_r}{\epsilon_{effu}}\right)\epsilon_r}} - 2\Delta L = 2.050\ mm$$

The resonance associated with a patch length of 2.050 mm lands at 31.7 GHz (Figure A-1), an error of 0.3%. It is important to note that aperture width and stub length were held the same for all three simulations in Figure A-1, and that is the reason the resonance at 31.8 GHz is so deep.

Antenna dimensions for resonant frequencies ranging from 7 GHz to 37 GHz were determined using Antenna Magus and then also calculated following the process outlined in CHAPTER 3. The dimensions generated by each method were simulated in CST MWS. A comparison is presented in Table A-1. The results are similar, although above 12 GHz the equation for patch length developed in this appendix yields a resonant frequency that more closely matches the target frequency.

Antenna Magus was contacted for insight into the operation of their algorithm design code. Although the details could not be shared, their customer support team stated they have implemented a multi-dimensional regression based approach as per a paper from Woods, Sikel, and Brand [32]. This gives a more generalized method, which isn't limited by substrate permittivity and electrical thickness like the empirically developed equation from Hammerstad.

The comparison presented in Table A-1 is for only one substrate material (dielectric constant of 3.0 and thickness of 0.510 mm). A substrate with dielectric constant 4.4 was also checked, and again there was seen a high correlation between Antenna Magus and the patch length equation developed in this appendix. Several substrates need be compared before making conclusion. Ultimately, it's the results we see in the laboratory that validate the equation. However, modern computers and simulation software have become so powerful that results presented here are a decent indication of what to expect.

Table A-1: Patch Length Accuracy Comparison

Design Frequency (GHz)	**7**	**12**	**17**	**22**	**27**	**32**	**37**
Parameter Values as per Antenna Magus							
Patch Width (mm)	15.142	8.833	6.235	4.818	3.926	3.312	2.865
ϵ_{effu}	2.84	2.77	2.71	2.66	2.63	2.59	2.56
Fringing Length (mm)	0.251	0.249	0.247	0.245	0.243	0.241	0.239
Patch Length (mm)	11.531	6.449	4.367	3.216	2.558	2.096	1.767
Parameter Values as per Calculations following CHAPTER 3							
Patch Width (mm)	15.142	8.833	6.235	4.818	3.926	3.312	2.865
ϵ_effu	2.84	2.77	2.71	2.66	2.63	2.59	2.56
Fringing Length (mm)	0.251	0.249	0.248	0.245	0.243	0.241	0.239
Patch Length (mm)	11.535	6.430	4.344	3.216	2.512	2.032	1.684
CST MWS Results using Parameters from Magus & Calculations following CHAPTER 3							
Magus, Resonance (GHz)	6.81	11.79	16.78	21.70	26.48	31.11	35.70
Magus, Error (%)	2.80	1.79	1.30	1.38	1.96	2.84	3.65
Calculated, Resonance (GHz)	6.80	11.82	16.87	21.88	26.85	31.90	37.03
Calculated, Error (%)	2.88	1.54	0.81	0.56	0.56	0.32	0.08

APPENDIX B

EUQATION FOR UPPER RESONANCE

Inspection of the current distribution around the resonant slot in Figure B-1 reveals that the null is located at the center of the resonant slot, is located directly over the RF feed, and is roughly with width of the RF feed.

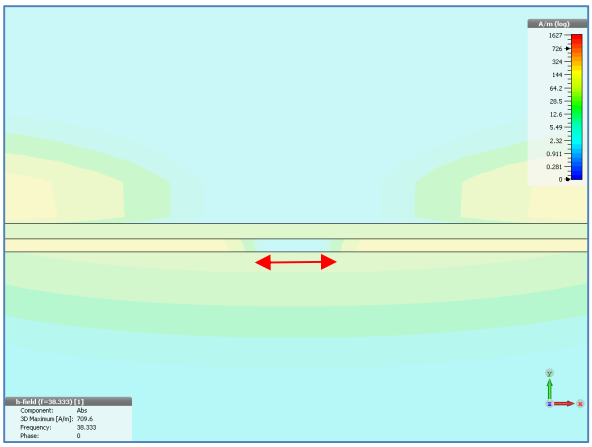

Figure B-1: Magnified View of Lower Slot on Dual Band Antenna

Visiting the equation for resonant frequency associated with the slot in a dual band pin fed patch antenna [17], the resonant frequency is estimated as follows:

Equation B-1

$$(f_r)_{03} = \frac{c}{2(Ls + d)\sqrt{\epsilon_{effslot}}}$$

Where:

Equation B-2

$$\varepsilon_{effslot} = \frac{\varepsilon_r + 1}{2} + \frac{\varepsilon_r - 1}{2}\left(1 + 12\frac{h_u}{W_{slot}}\right)^{-1/2} = 2.09$$

Since the resonant frequency is proportional to the length of the slot (*Ls*) and the width of the slot (*d*) then, when considering the nulls, the equation for the resonant frequency associated with the slot in an aperture fed patch antenna can be modified as follows:

Equation B-3

$$(f_r)_{03} = \frac{c}{2(Ls + d - Null_{factor})\sqrt{\epsilon_{effslot}}}$$

The variable $Null_{factor}$ is determined empirically by running simulations in CST MWS on several different scenarios of the aperture fed antenna, firstly without resonant slots and then secondly with resonant slots. Table B-1 summarize the findings. For a slot length of 3.100 mm, minimal error between predicted resonance and simulated resonance was observed when:

Equation B-4

$$Null_{factor} = \sqrt{\epsilon_{effslot}} * W_{feed}$$

This relationship held to an error less than 3% when the dielectric constant changed from 3 to 4, however, the error increased to almost 5% when the length of the slot changed from 3.100 mm to 3.250 mm (Table B-2). The equation can be used to roughly guess the minimum value of the upper resonance since the length of the slot cannot exceed the width of the patch. Further experimentation is required to establish a relationship that will hold true for all values of permittivity, substrate thickens, slot width, slot offset, and feed width.

Table B-1: CST MWS Resonance Comparison for Slot Length 3.100 mm

Design Frequency	**GHz**	**32**	**32**	**32**	**32**	**32**
Substrate Height	mm	0.150	0.250	0.350	0.450	0.550
Substrate Height Lambda	%	4.1	6.9	9.7	12.4	15.2
Magus Aperture Length	mm	1.028	1.256	1.463	1.648	1.815
Magus Aperture Width	mm	0.094	0.094	0.094	0.094	0.094
Magus RF Feed Width	mm	0.319	0.319	0.319	0.319	0.319
Magus Patch Length	mm	2.454	2.337	2.231	2.141	2.069
Magus Patch Width	mm	3.312	3.312	3.312	3.312	3.312
Magus Stub Length	mm	1.011	0.916	0.837	0.776	0.730
Slot Length	mm	3.100	3.100	3.100	3.100	3.100
Slot Width	mm	0.052	0.052	0.052	0.052	0.052
Slot Gap	mm	0.045	0.045	0.045	0.045	0.045
No Slots, CST Lower Resonance	GHz	31.7	31.7	31.7	31.6	31.3
Slots, CST Lower Resonance	GHz	28.0	28.3	28.5	28.4	28.3
Slots, CST Upper Resonance	GHz	37.99	38.3	38.6	38.7	39.0
Lower Resonance Change	%	11.7	10.9	10.2	9.9	9.5
sqrt (Ee(w/t, Er))		1.473	1.460	1.454	1.449	1.446
2(Ls + d + sqrt (Ee(w/t, Er))*Wf)		5.36E-3	5.37E-3	5.38E-3	5.38E-3	5.38E-3
Predicted Upper Resonance	GHz	37.97	38.2	38.4	38.5	38.6
Predicted Upper Error	%	0.06	0.09	0.49	0.59	1.13

Table B-2: CST MWS Resonance Comparison for Slot Length 3.250 mm

Design Frequency	**GHz**	**32**	**32**	**32**	**32**	**32**
Substrate Height	mm	0.150	0.250	0.350	0.450	0.550
Substrate Height Lambda	%	4.1	6.9	9.7	12.4	15.2
Magus Aperture Length	mm	1.028	1.256	1.463	1.648	1.815
Magus Aperture Width	mm	0.094	0.094	0.094	0.094	0.094
Magus RF Feed Width	mm	0.319	0.319	0.319	0.319	0.319
Magus Patch Length	mm	2.454	2.337	2.231	2.141	2.069
Magus Patch Width	mm	3.312	3.312	3.312	3.312	3.312
Magus Stub Length	mm	1.011	0.916	0.837	0.776	0.730
Slot Length	mm	3.250	3.250	3.250	3.250	3.2500
Slot Width	mm	0.052	0.052	0.052	0.052	0.052
Slot Gap	mm	0.045	0.045	0.045	0.045	0.045
No Slots, CST Lower Resonance	GHz	31.29	30.93	32.73	31.29	30.75
Slots, CST Lower Resonance	GHz	27.45	27.6	27.99	28.05	28.93
Slots, CST Upper Resonance	GHz	12.3	10.8	14.5	10.4	5.9
Lower Resonance Change	%	37.28	37.2	37.92	38.19	38.49
sqrt (Ee(w/t, Er))		1.473	1.460	1.454	1.449	1.446
2(Ls + d + sqrt (Ee(w/t, Er))*Wf)		5.36E-3	5.37E-3	5.38E-3	5.38E-3	5.38E-3
Predicted Upper Resonance	GHz	35.96	36.22	36.37	36.46	36.53
Predicted Upper Error	%	3.55	2.64	4.10	4.53	5.10

APPENDIX C

PARAMETRIC ANALYSIS OF DUAL BAND ANTENNA

The findings of the parametric analysis are summarized Table C-1. A legend is given in Table C-1. The most sensitive dimensions are patch length, aperture length, slot length, and the permittivity of the upper substrate.

IPC standards for etching tolerance is +/- 20% however it is reasonable to expect PWB suppliers to achieve +/- 0.0254 (one thousand of an inch) on ½ oz copper. The general idea of this parametric analysis is to shift dimensions as per PWB etching capabilities. In cases where such a small dimensional change generated no visible disturbance to the resonant frequencies, a larger dimensional change was implemented into the parametric analysis. Consequently, most x-axis or y-axis dimensions were shifted by either +/- 0.1 mm or +/- 0.01 mm depending on their sensitivity. The slots were shifted by +/-0.05 mm in the x-axis since anything greater would cause the slot break through the side of the patch rendering no point to simulation.

During the PWB fabrication process the aperture is etched into the ground plane and then a glue is used to bond the upper substrate to the lower substrate which includes the etched aperture. Depending on the quality of the bonding process, it is possible the aperture is either filled with glue or filled with air. A parametric analysis was run on aperture material dielectric constant and little difference was noticed. Ground plane thickness had little impact when the aperture dielectric constant of the bonding glue is same as the substrate. However, ground plane thickness does have noticeable impact on the resonances when the aperture is filled with air.

Table C-1: Legend for Parametric Analysis of Dual Band Antenna

Symbol	Frequency Shift
"— "	Less than +/- 0.10%
"↑" or "↓"	+/- 0.10% and +/- 0.50%
"↑↑" or "↓↓"	Between +/- 0.50% and +/- 1.00%
"↑↑↑" or "↓↓↓"	Between +/- 1.00% and +/- 1.50%
"↑↑↑↑" or "↓↓↓↓"	Greater than +/- 1.50%

Table C-2: Parametric Analysis Summary for Dual Band Antenna

Antenna Parameter				Lower Resonance	Upper Resonance
Feature	**Descriptor**	**Axis**	**Shifted**	**Incr. / Decrease**	**Incr. / Decrease**
patch	width	x-axis	+0.10 mm	↑	↓
patch	length	y-axis	+0.10 mm	↓↓↓↓	↓↓↓↓
aperture	length	x-axis	+0.10 mm	↓↓↓↓	↑↑
aperture	width	y-axis	+0.01 mm	↓	—
slot	length	x-axis	+0.01 mm	↓↓↓↓	↓↓↓
slot	width	y-axis	+0.01 mm	↓↓	↑
patch offset	---	x-axis	+0.10 mm	—	—
patch offset	---	y-axis	+0.10 mm	—	↓
aperture offset	---	x-axis	+0.10 mm	—	—
aperture offset	---	y-axis	+0.10 mm	↓↓	↑↑
slot offset	---	x-axis	+0.05 mm	—	—
slot offset	---	y-axis	+0.01 mm	↓↓	↑↑
upper substrate	height	z-axis	+0.02 mm	↓	↓

upper substrate	ε_r	---	+0.1	↓↓↓	↓↓↓
upper substrate	D_f	---	+0.0017	—	—
lower substrate	height	z-axis	+0.01 mm	↓	—
lower substrate	ε_r	---	+0.1	↑	↓
lower substrate	D_f	---	+0.0017	—	—
ground	height	z-axis	+0.02 mm	↑	—
patch	height	z-axis	+0.02 mm	↓	↓
feed	height	z-axis	+0.02 mm	—	—
feed	width	x-axis	+0.02 mm	↑	↑
feed	length	y-axis	+1.00 mm	↑	↓
stub	length	y-axis	+0.10 mm	↑	↑↑

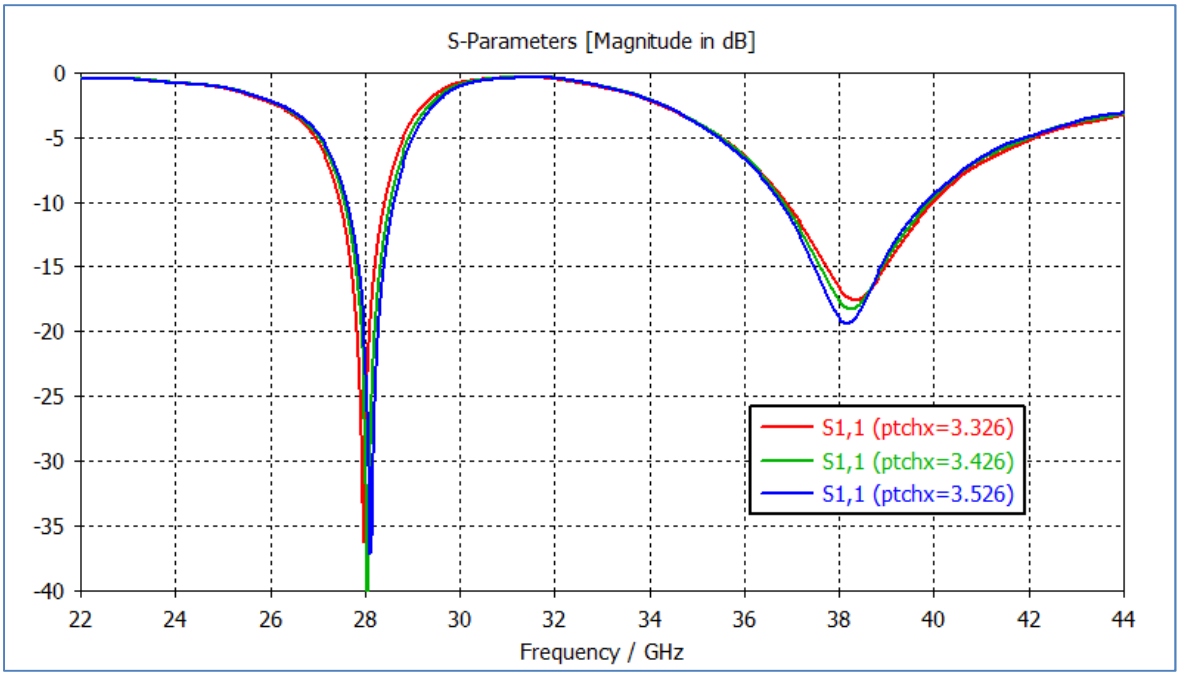

Figure C-1: Parametric Analysis of Patch Width (x-axis)

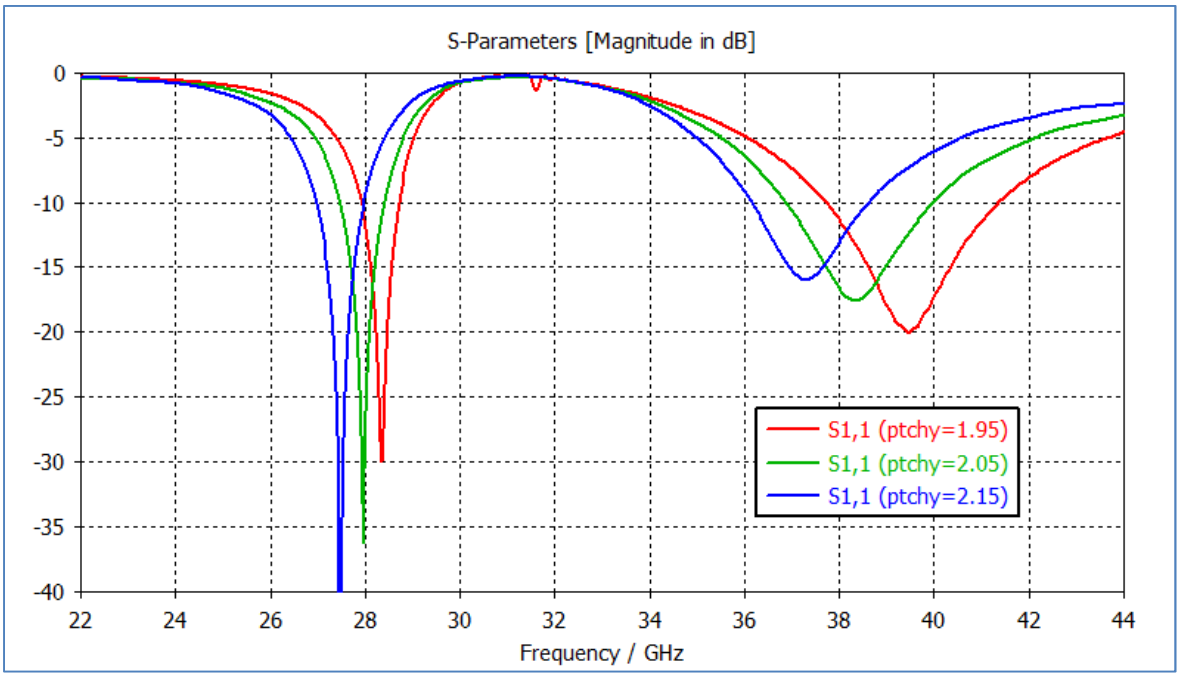

Figure C-2: Parametric Analysis of Patch Length (y-axis)

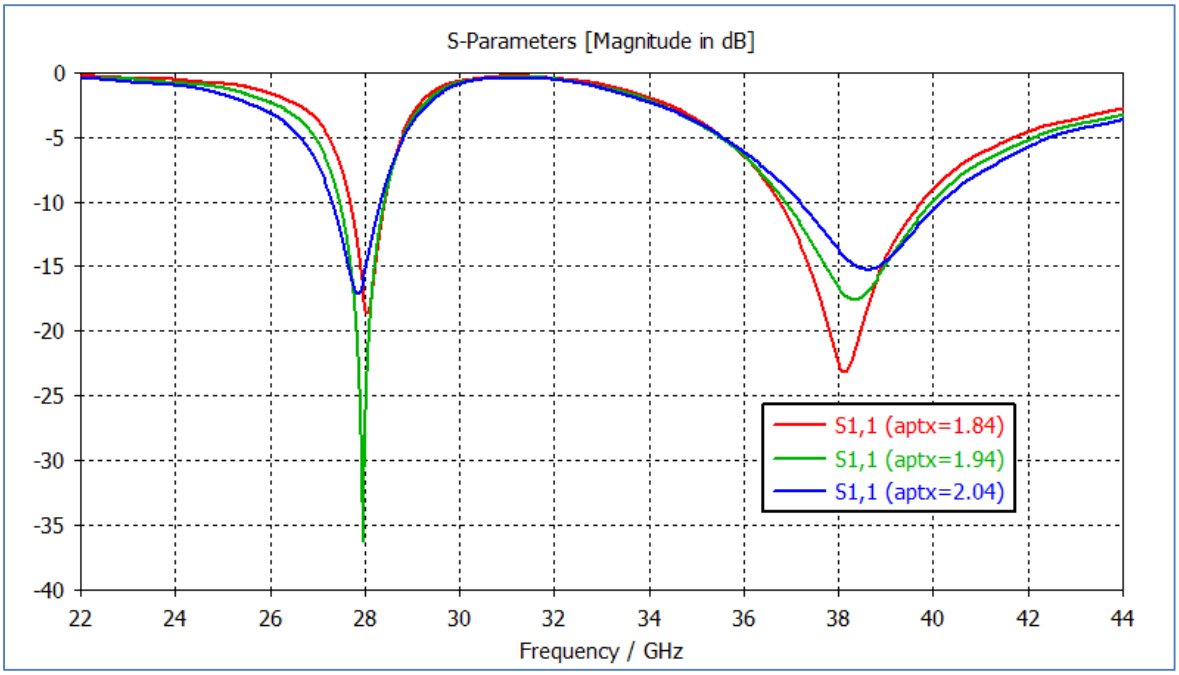

Figure C-3: Parametric Analysis of Aperture Length (x-axis)

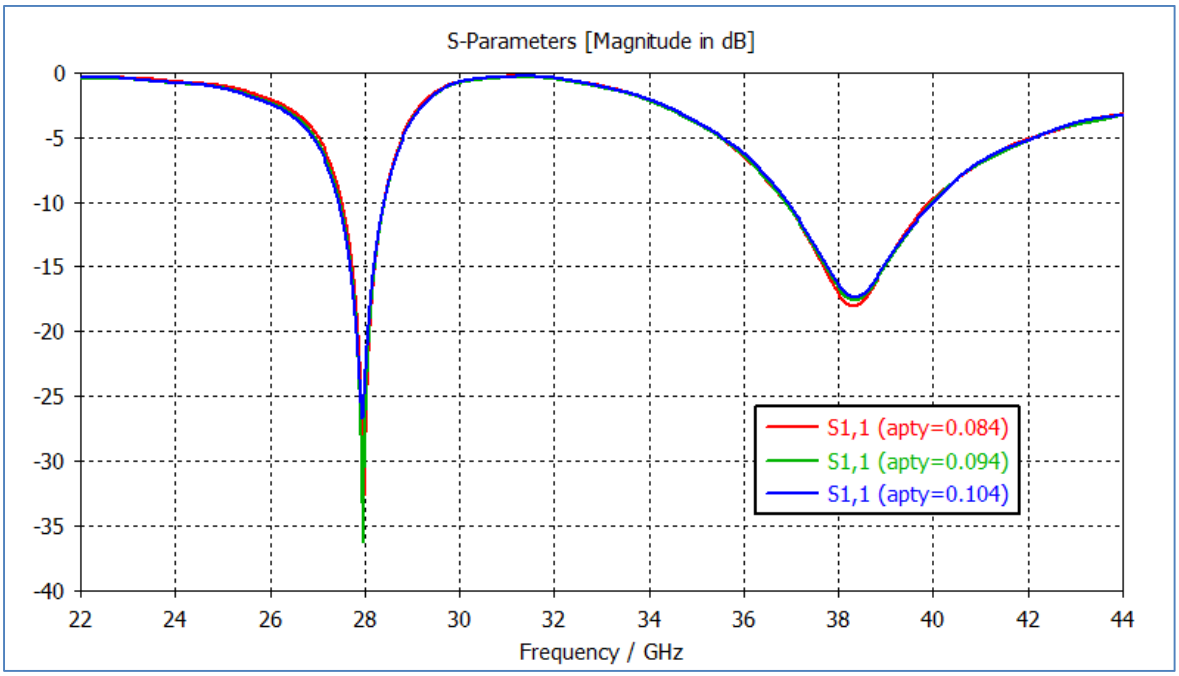

Figure C-4: Parametric Analysis of Aperture Width (y-axis)

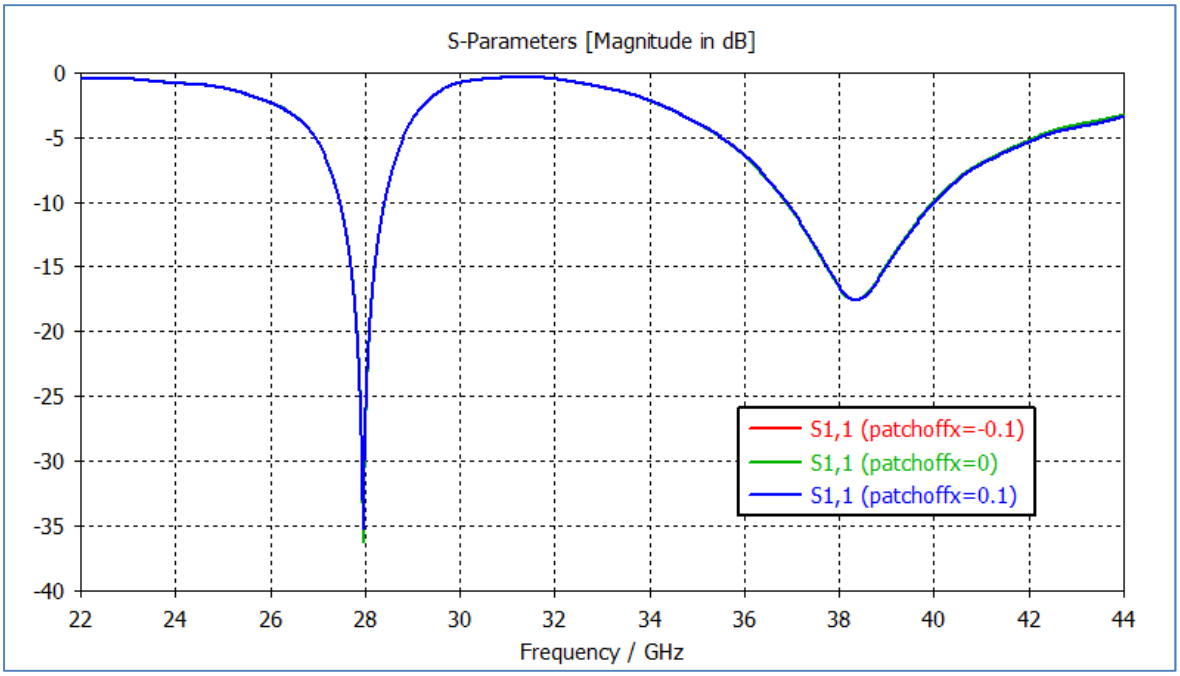

Figure C-5: Parametric Analysis of Patch Offset from Center (x-axis)

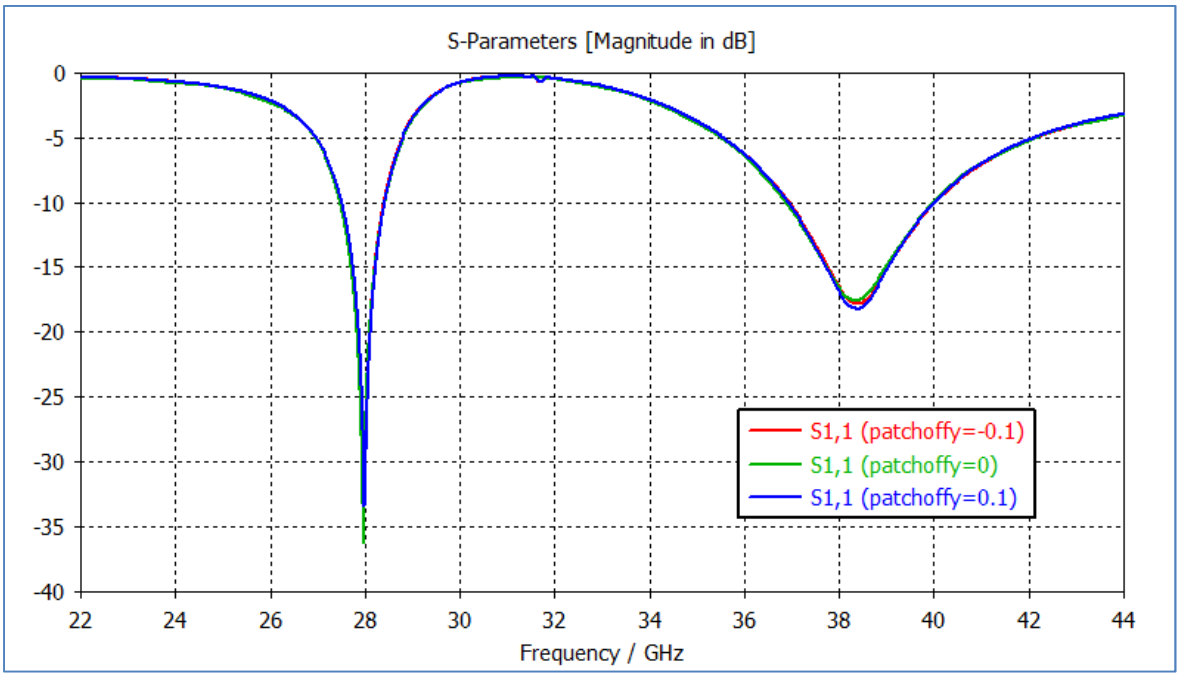

Figure C-6: Parametric Analysis of Patch Offset from Center (y-axis)

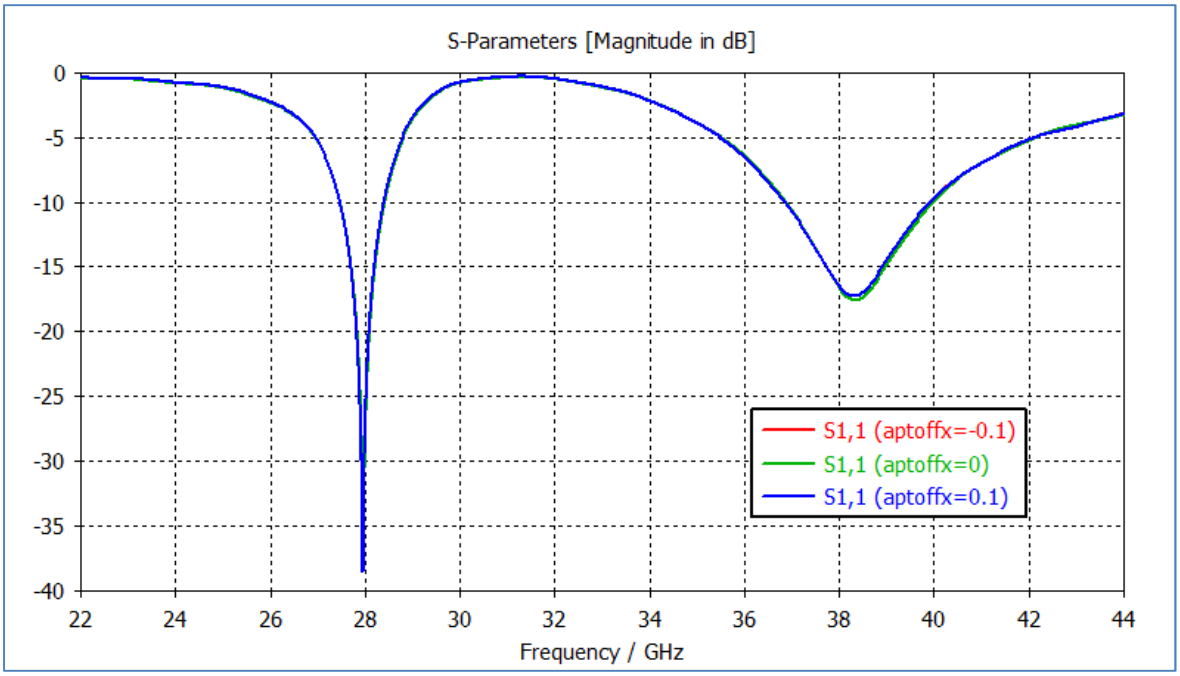

Figure C-7: Parametric Analysis of Aperture Offset from Center (x-axis)

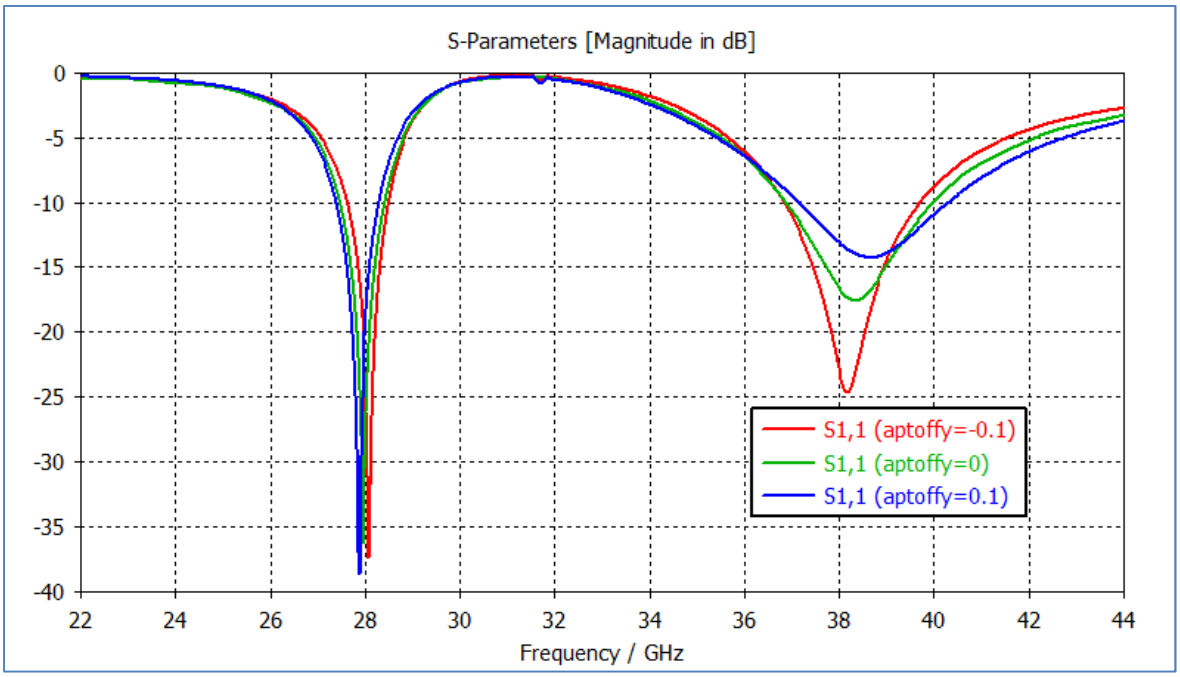

Figure C-8: Parametric Analysis of Aperture Offset from Center (y-axis)

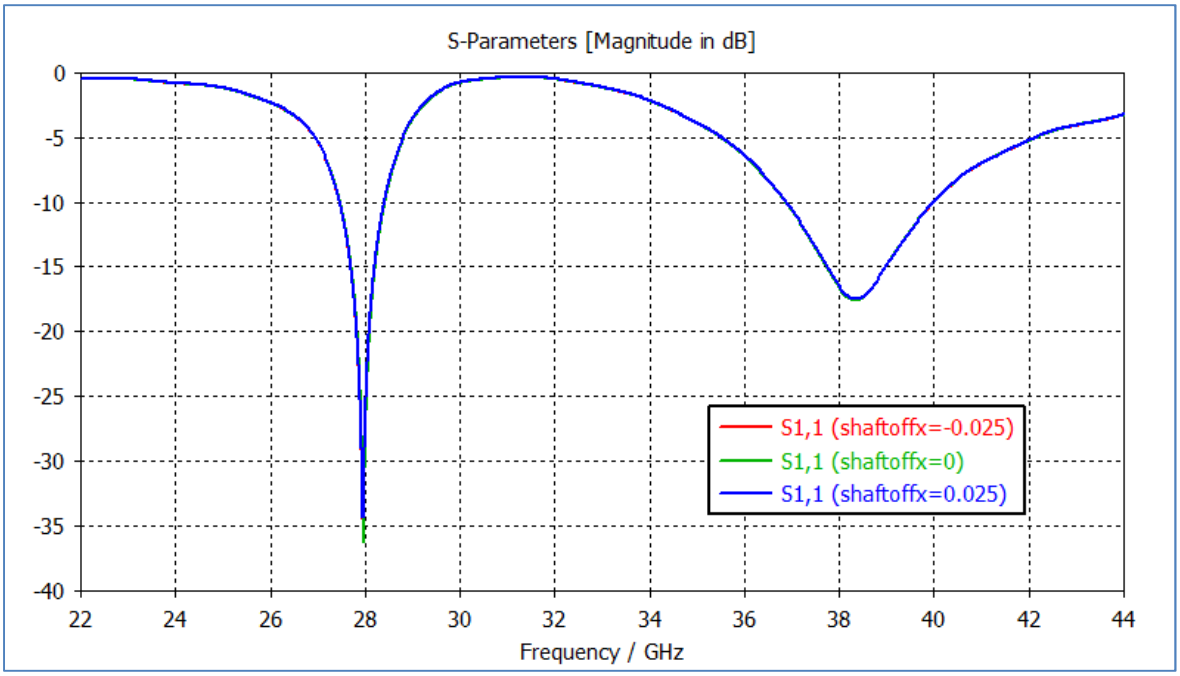

Figure C-9: Parametric Analysis of Slot Offset from Center (x-axis)

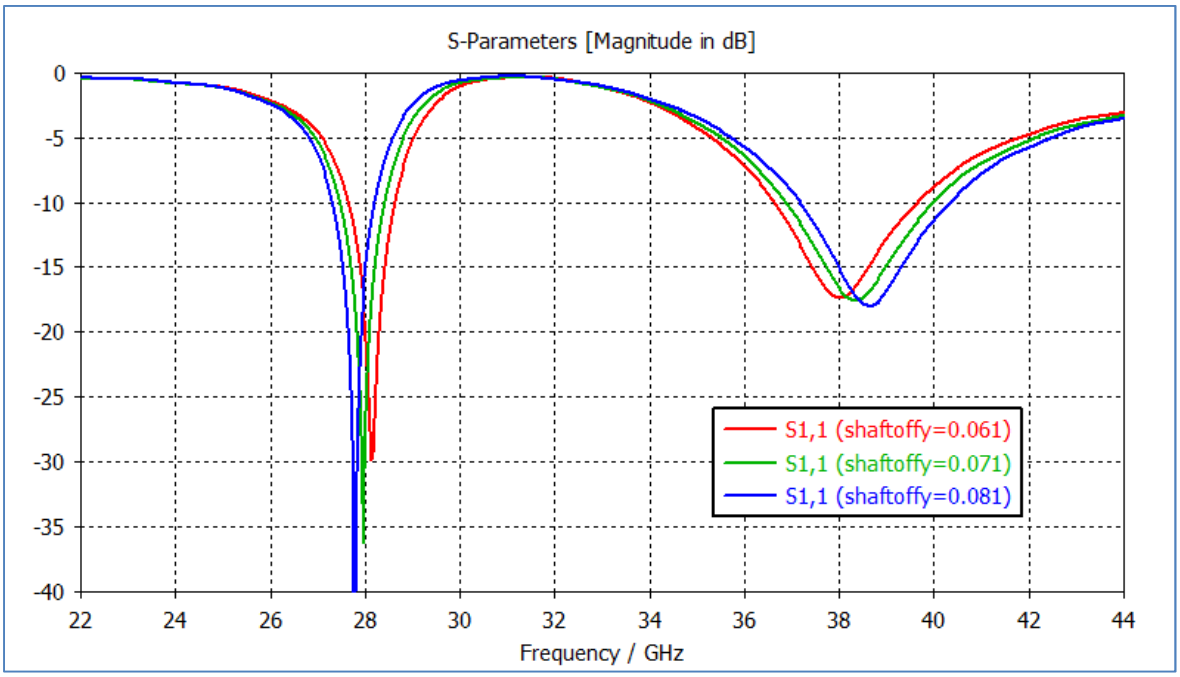

Figure C-10: Parametric Analysis of Slot Offset from Center (y-axis)

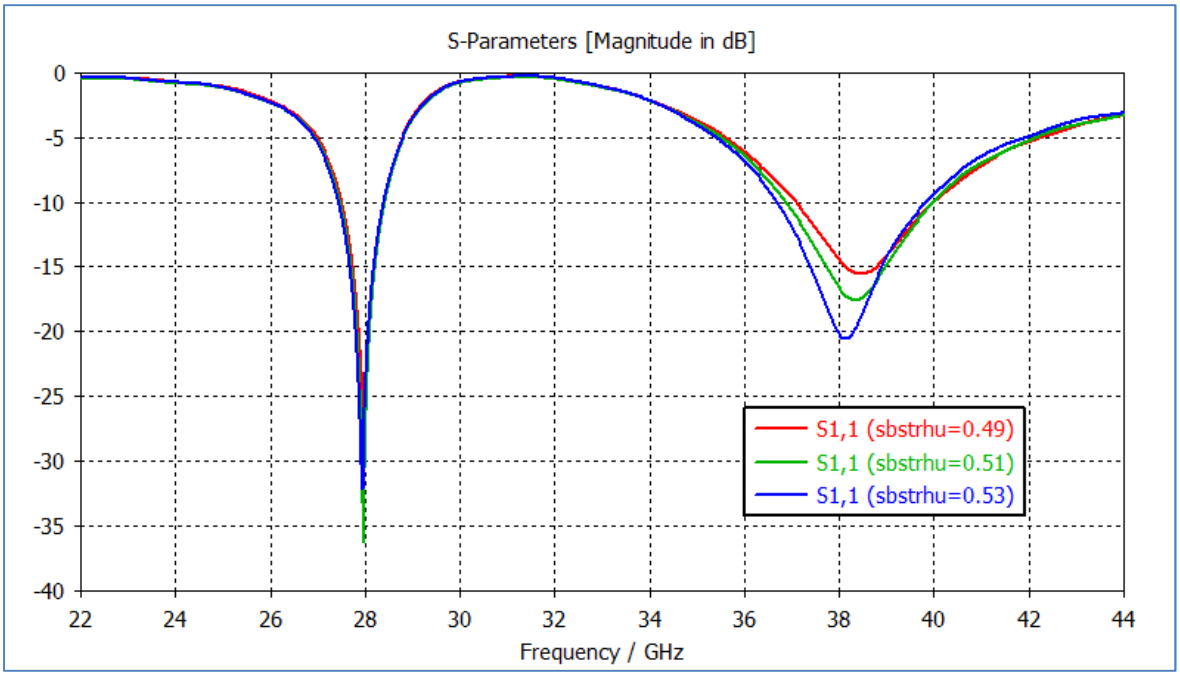

Figure C-11: Parametric Analysis of Upper Substrate Height

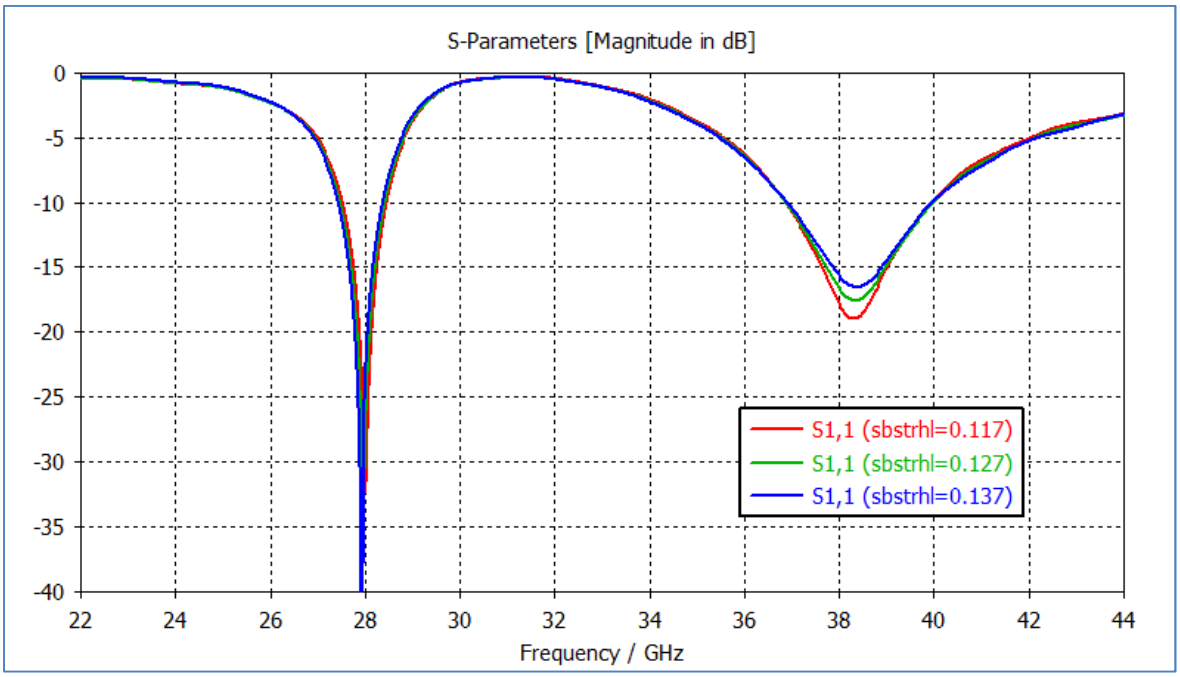

Figure C-12: Parametric Analysis of Lower Substrate Height

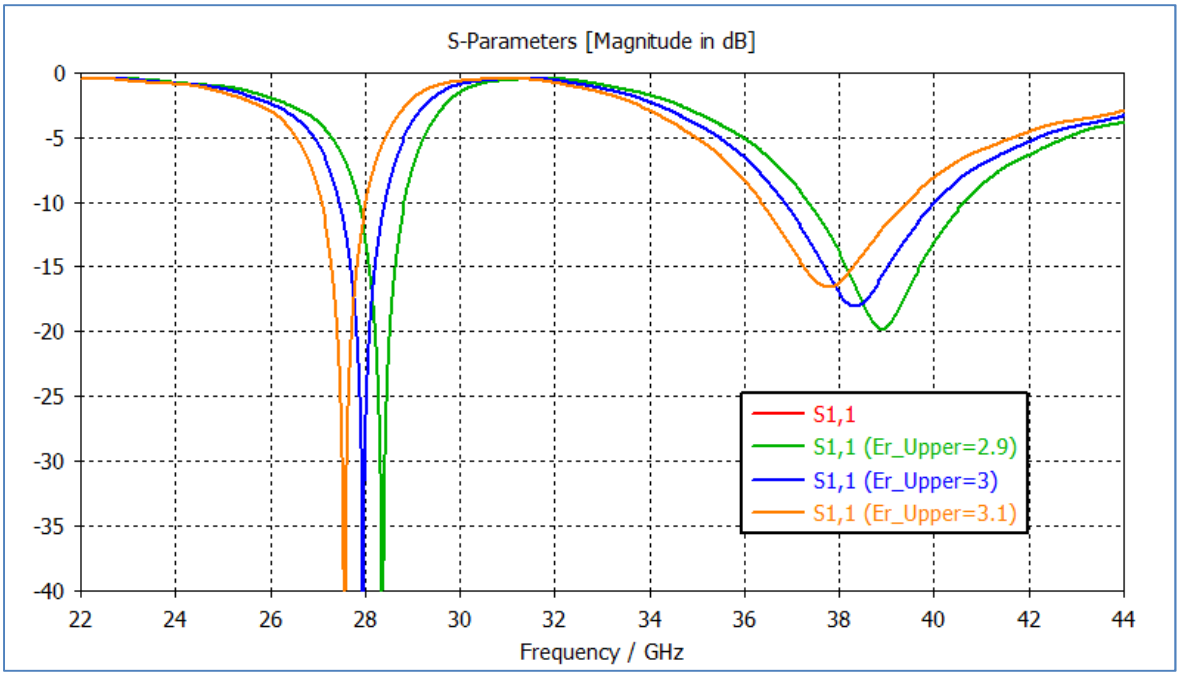

Figure C-13: Parametric Analysis of Upper Substrate Permittivity

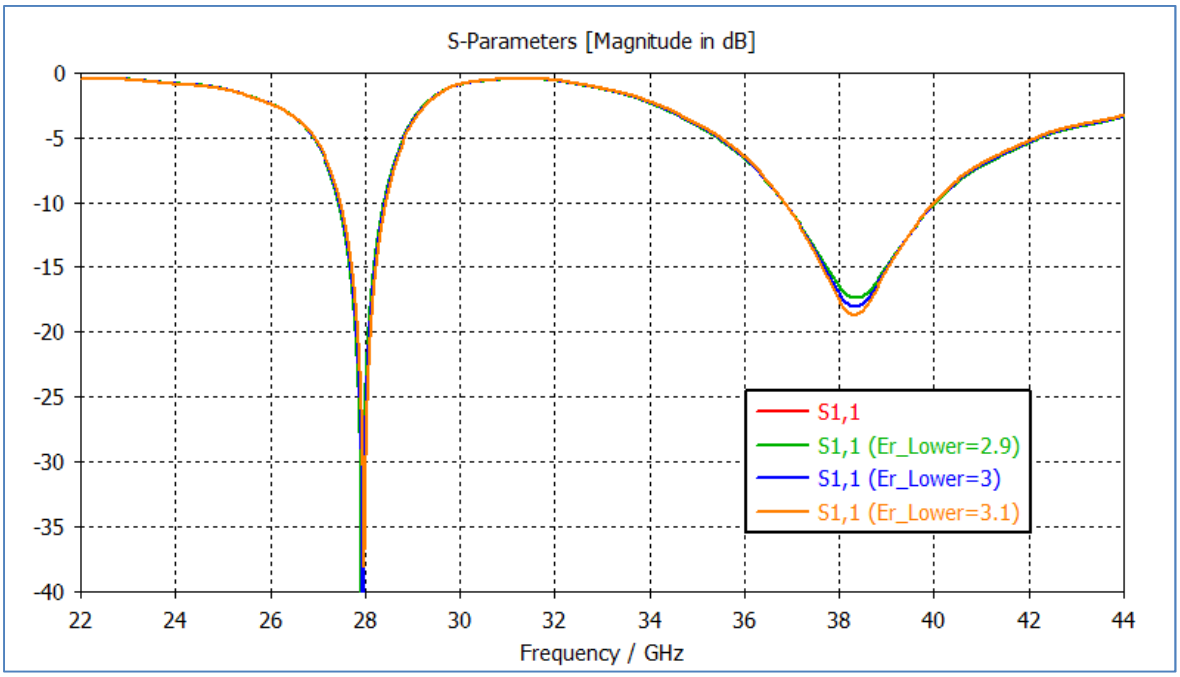

Figure C-14: Parametric Analysis of Lower Substrate Permittivity

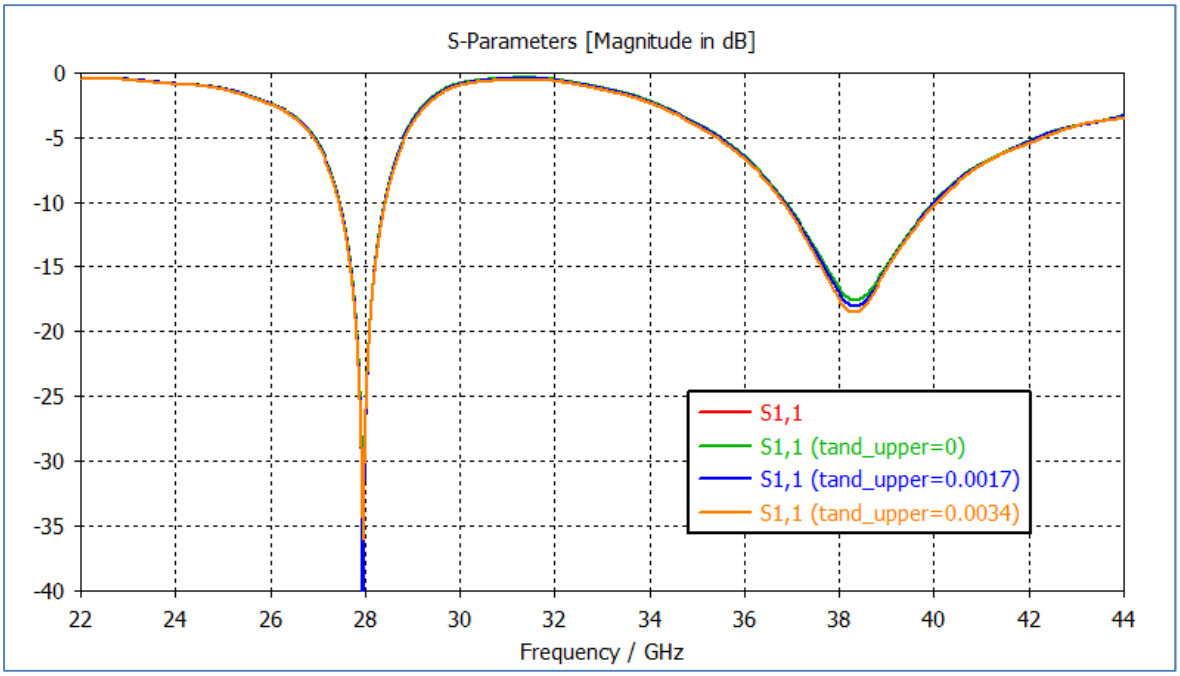

Figure C-15: Parametric Analysis of Upper Substrate Loss Tangent

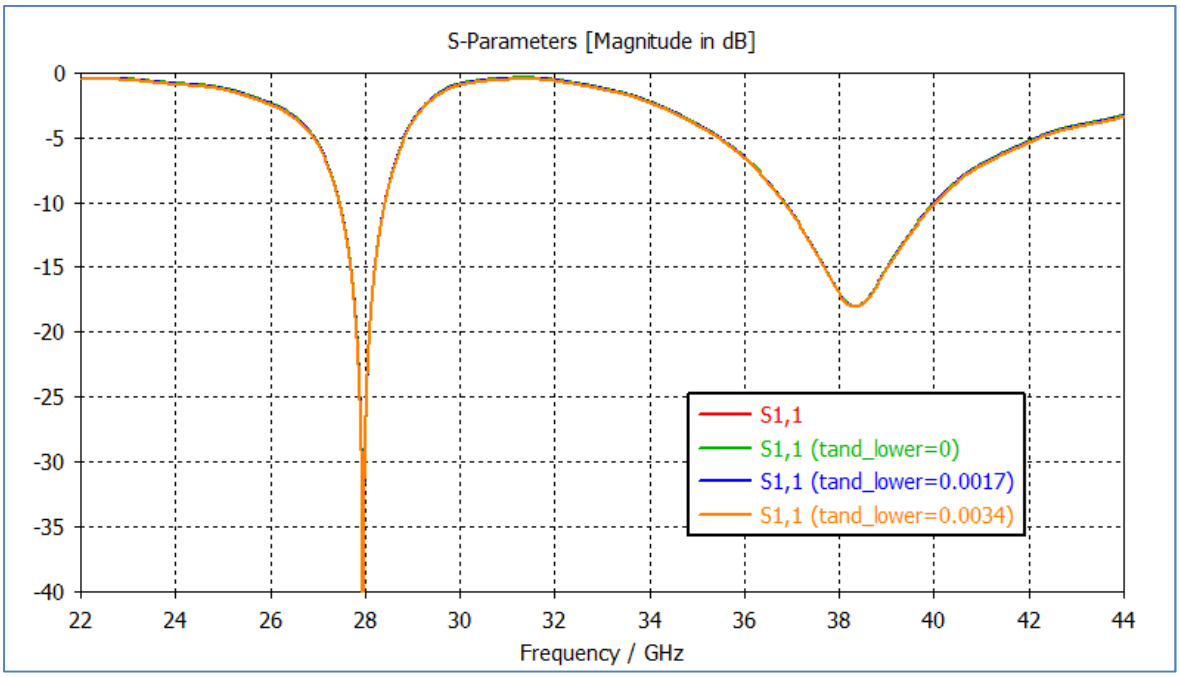

Figure C-16: Parametric Analysis of Lower Substrate Loss Tangent

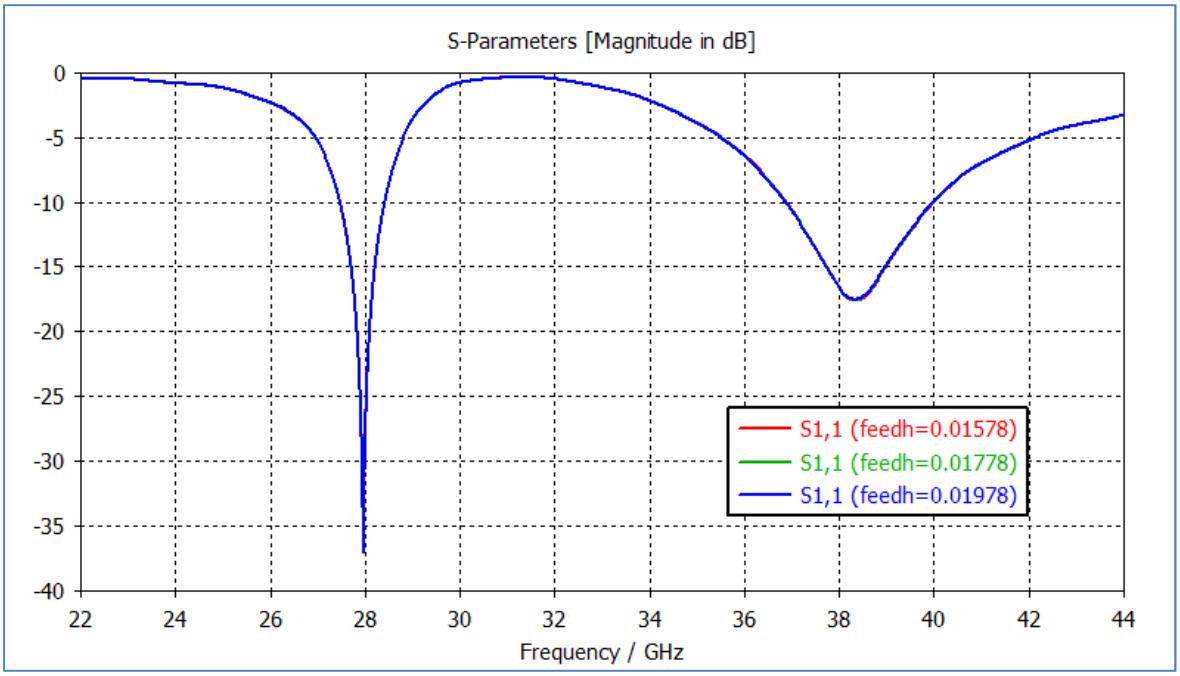

Figure C-17: Parametric Analysis of RF Feed Height

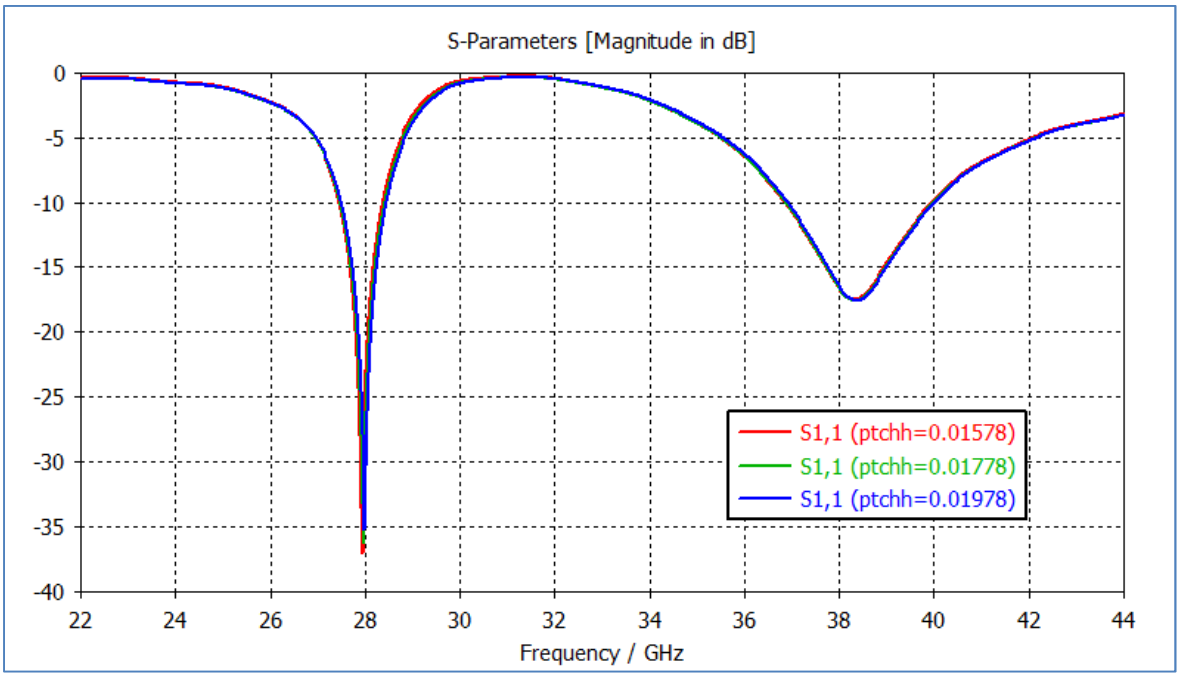

Figure C-18: Parametric Analysis of Patch Height

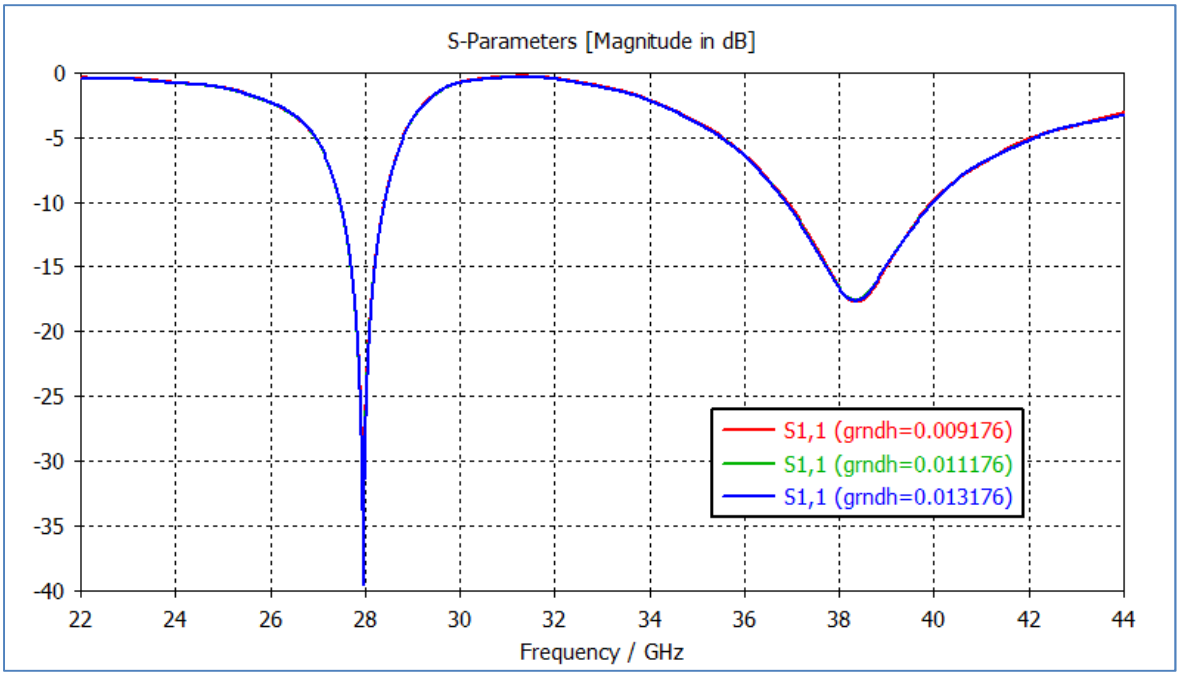

Figure C-19: Parametric Analysis of Ground Height

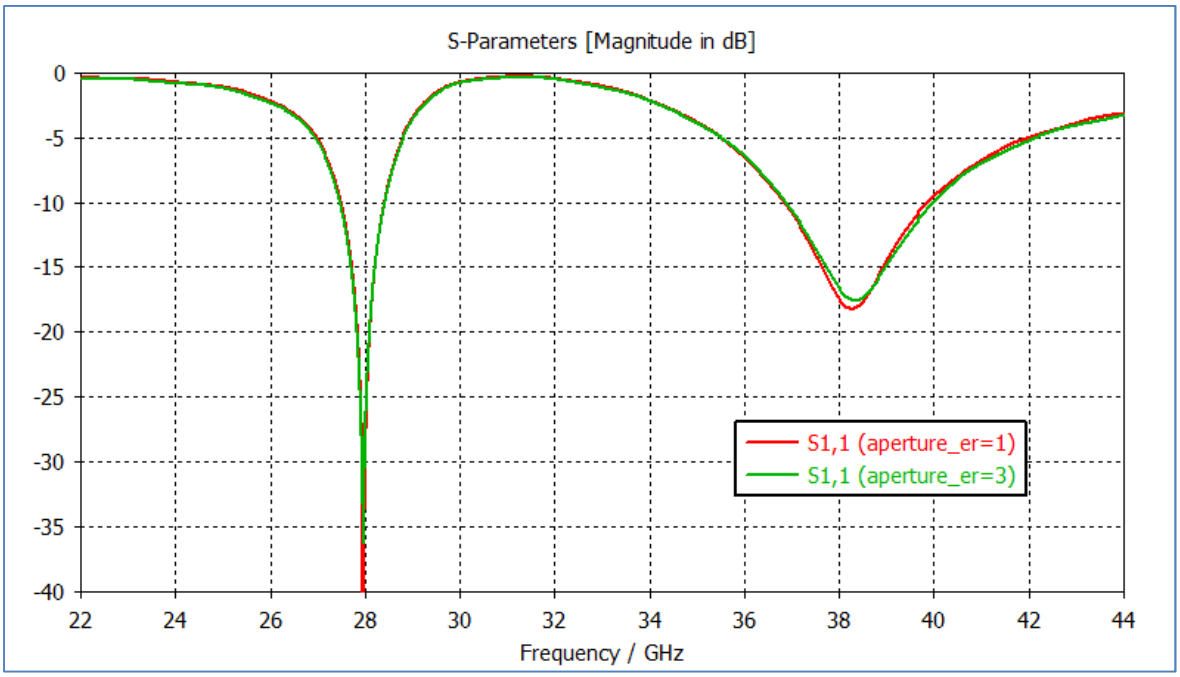

Figure C-20: Parametric Analysis of Aperture Material

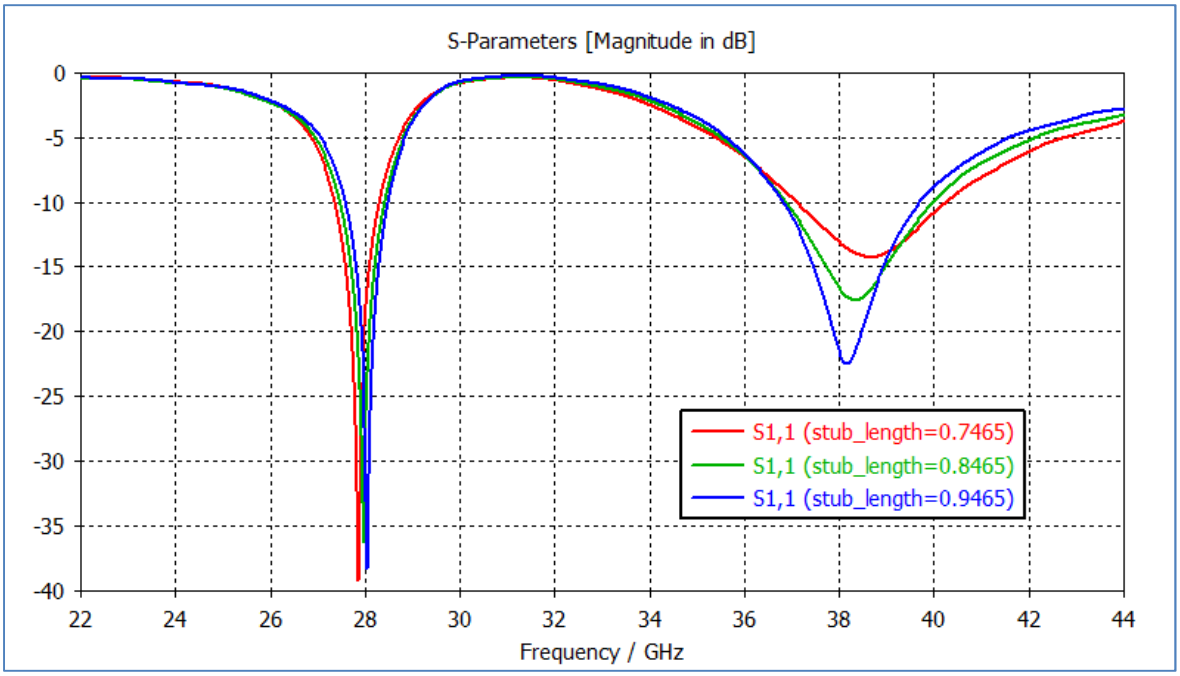

Figure C-21: Parametric Analysis of Stub Length

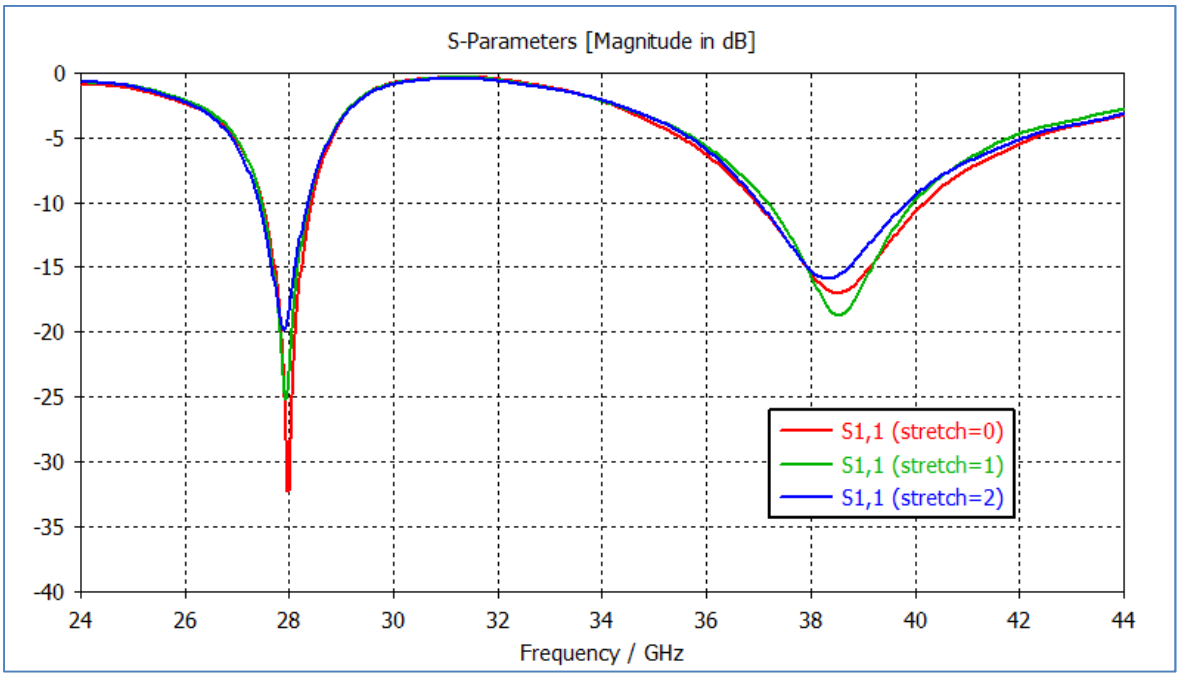

Figure C-22: Parametric Analysis of RF Feed Length

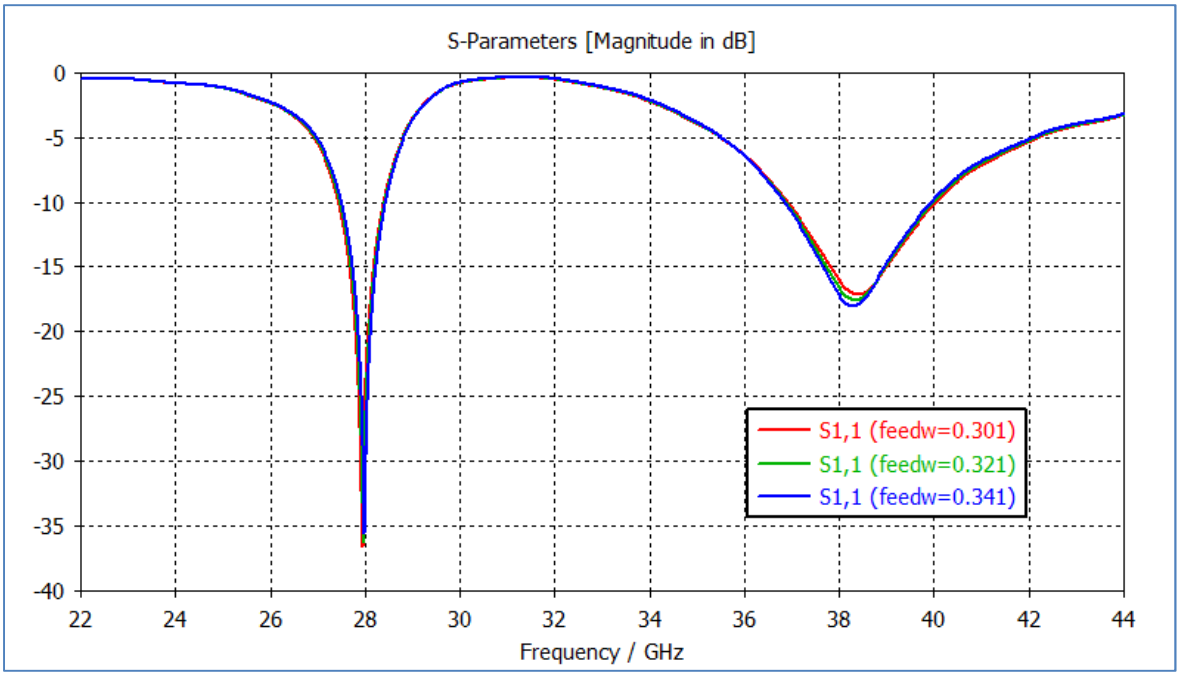

Figure C-23: Parametric Analysis of RF Feed Width

APPENDIX D

ARRAY PATTERNS

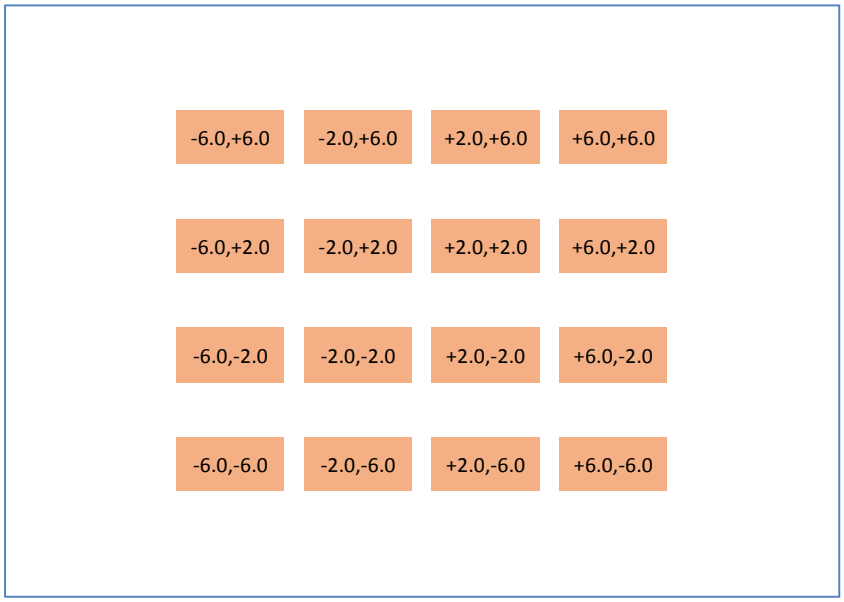

Figure D-1: Square 4x4 Array with 4.0 x 4.0 mm Spacing

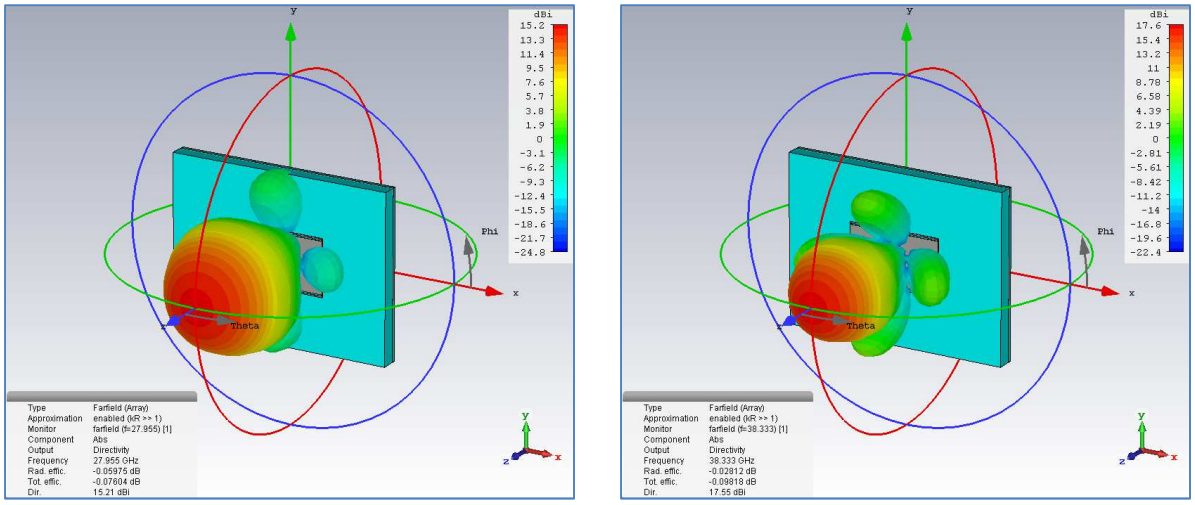

Figure D-2: Square 4x4 Array with 4.0 x 4.0 mm Spacing - Radiation

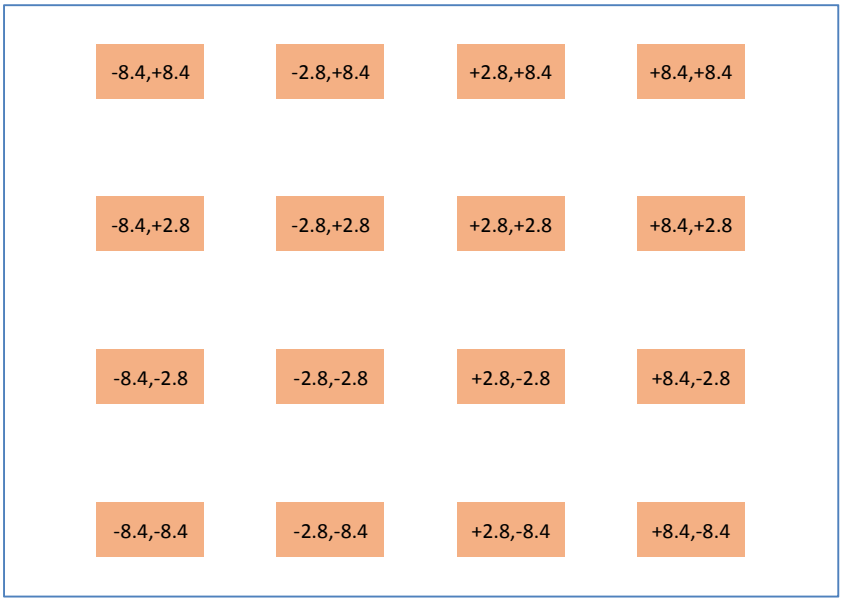

Figure D-3: Square 4x4 Array with 5.6 x 5.6 mm Spacing

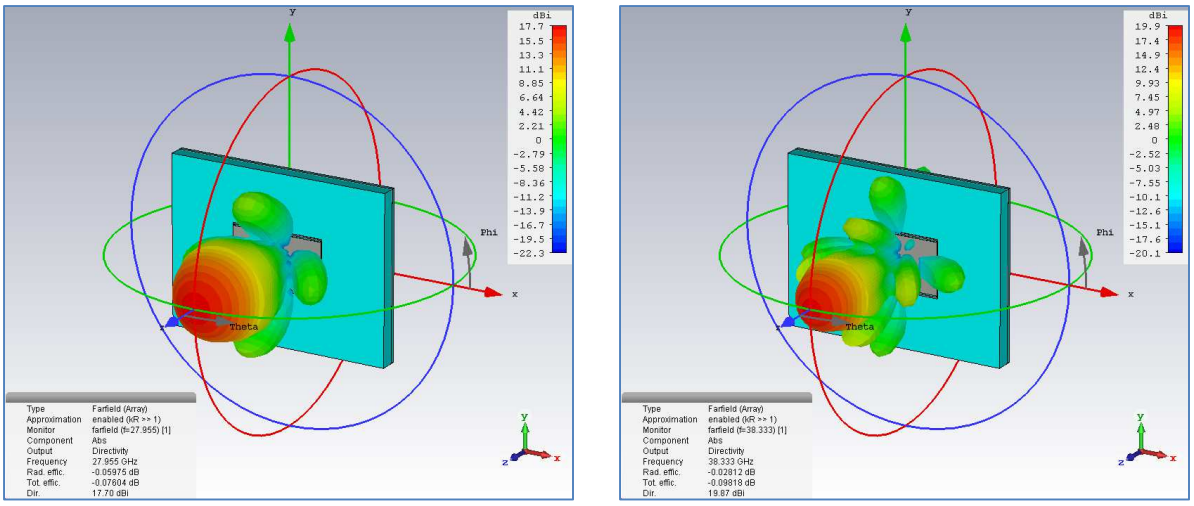

Figure D-4: Square 4x4 Array with 5.6 x 5.6 mm Spacing – Radiation

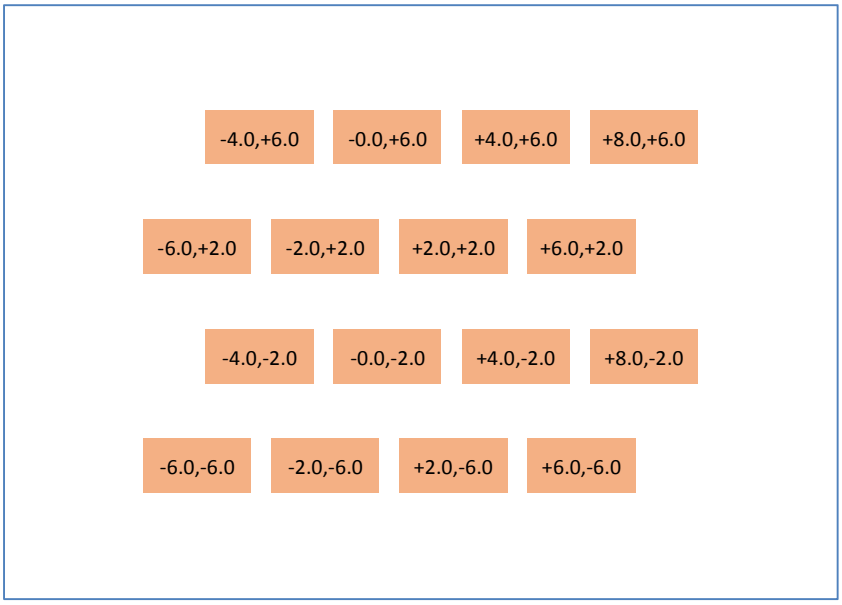

Figure D-5: Offset Square 4x4 Array with 4.0 x 4.0 mm Spacing

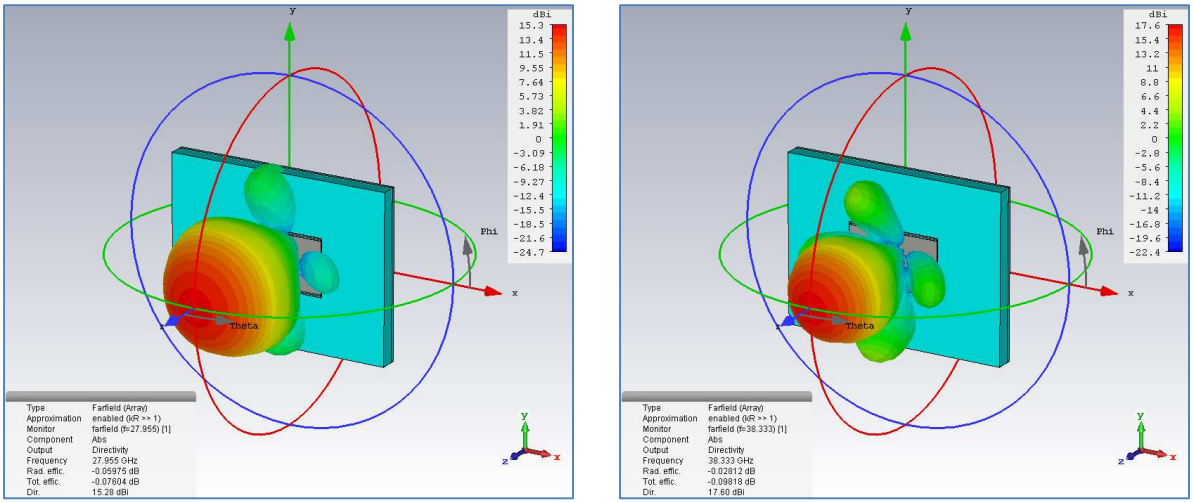

Figure D-6: Offset Square 4x4 Array with 4.0 x 4.0 mm Spacing – Radiation

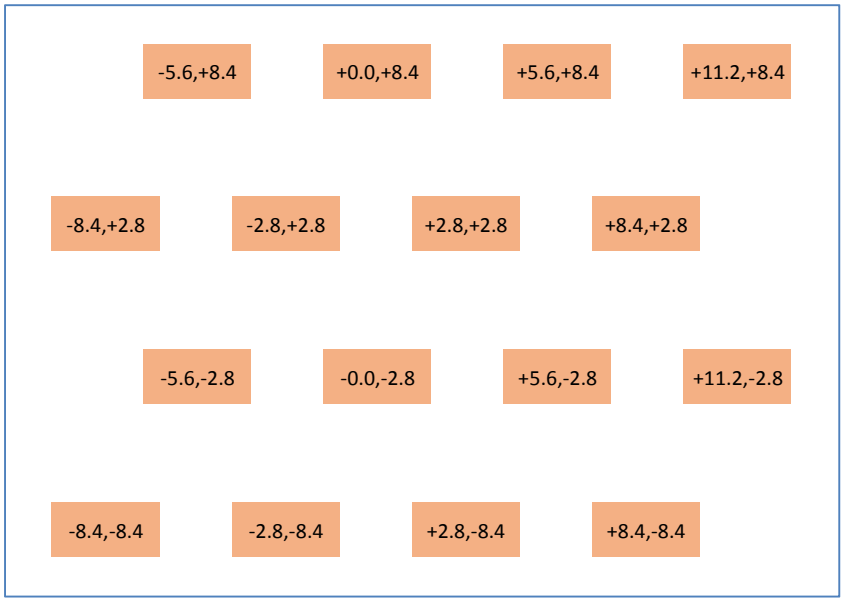

Figure D-7: Offset Square 4x4 Array with 5.6 x 5.6 mm Spacing

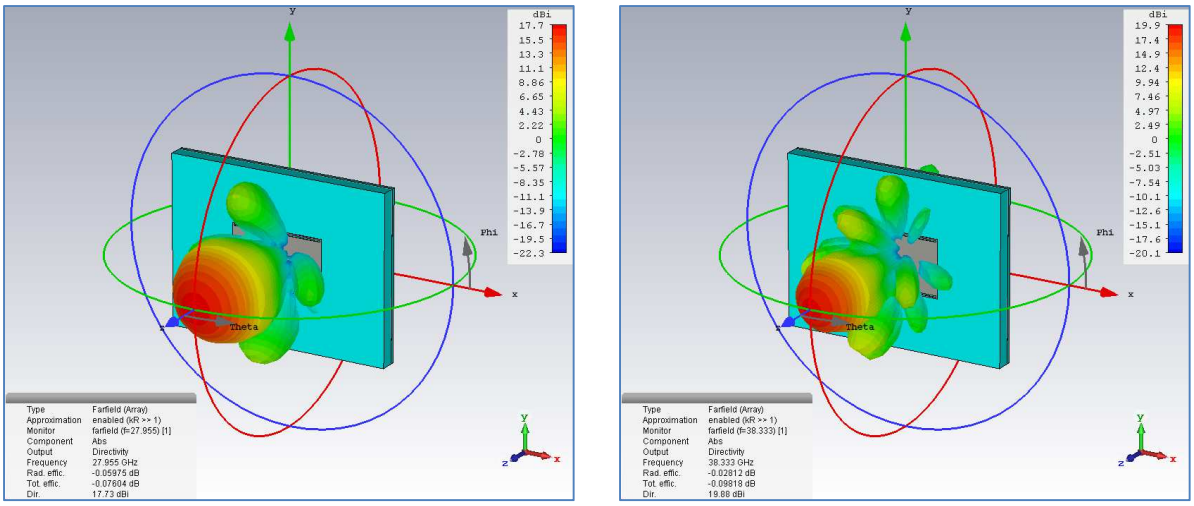

Figure D-8: Offset Square 4x4 Array with 5.6 x 5.6 mm Spacing – Radiation

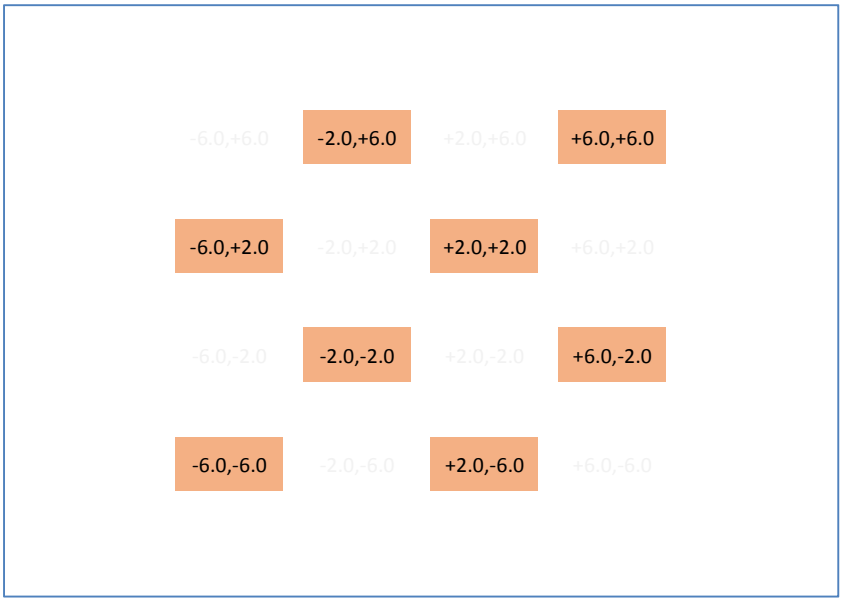

Figure D-9: Checkered Square 4x2 Array with 8.0 x 8.0 mm Spacing

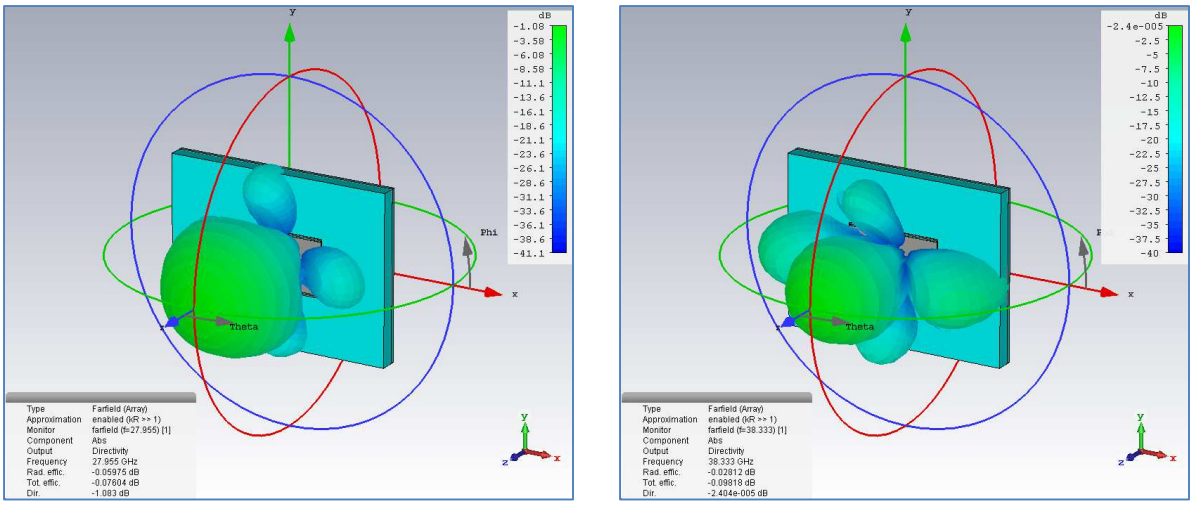

Figure D-10: Checkered Square 4x2 Array with 8.0 x 8.0 mm Spacing – Radiation

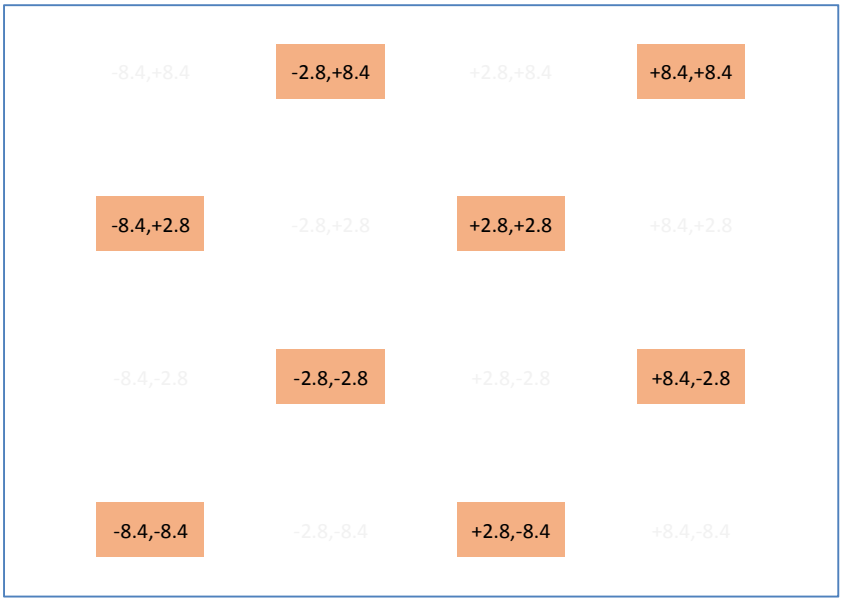

Figure D-11: Checkered Square 4x2 Array with 11.2 x 11.2 mm Spacing

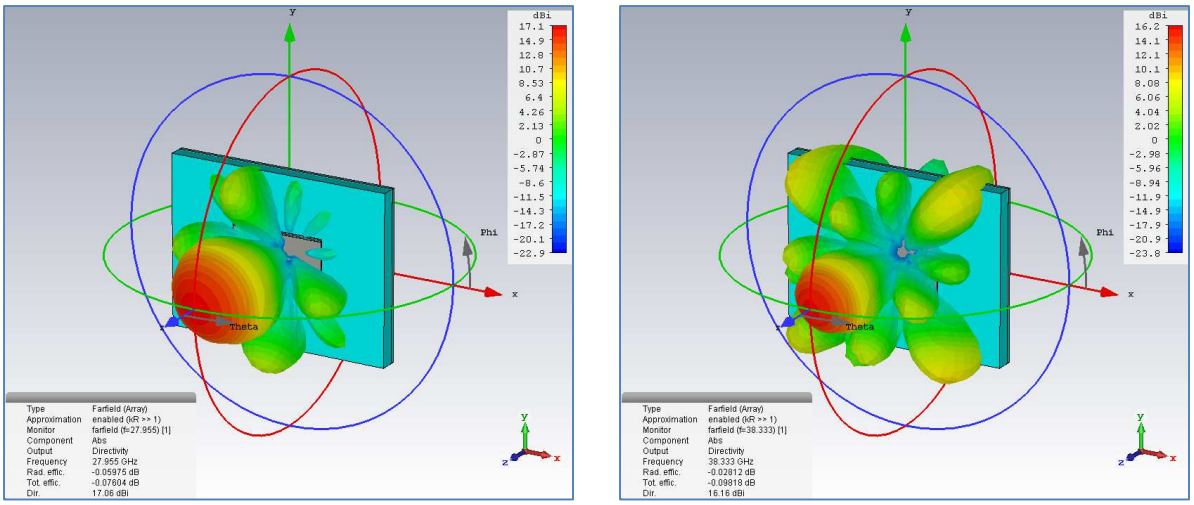

Figure D-12: Checkered Square 4x2 Array with 11.2 x 11.2 mm Spacing – Radiation

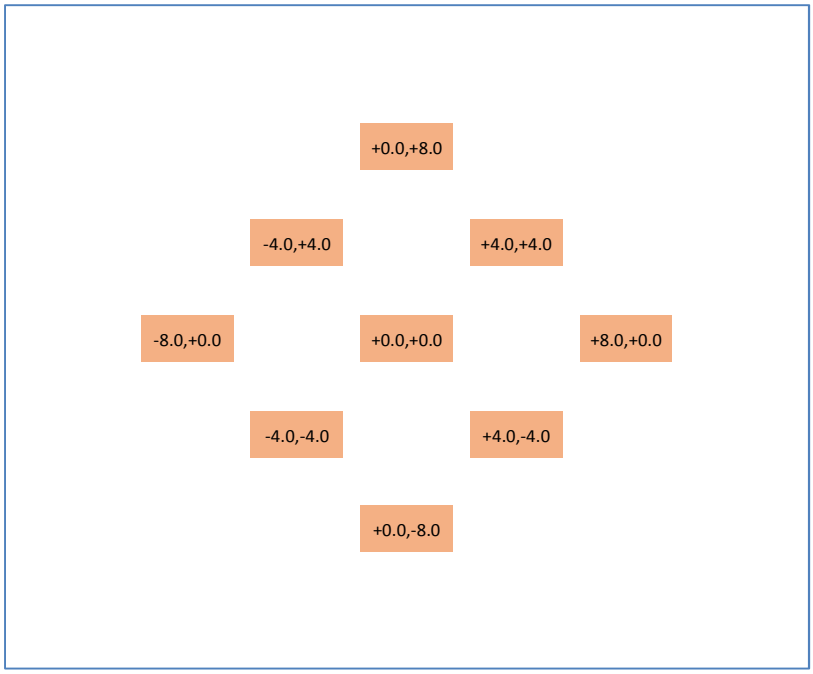

Figure D-13: Checkered Diamond 3x3 Array with 8.0 x 8.0 mm Spacing

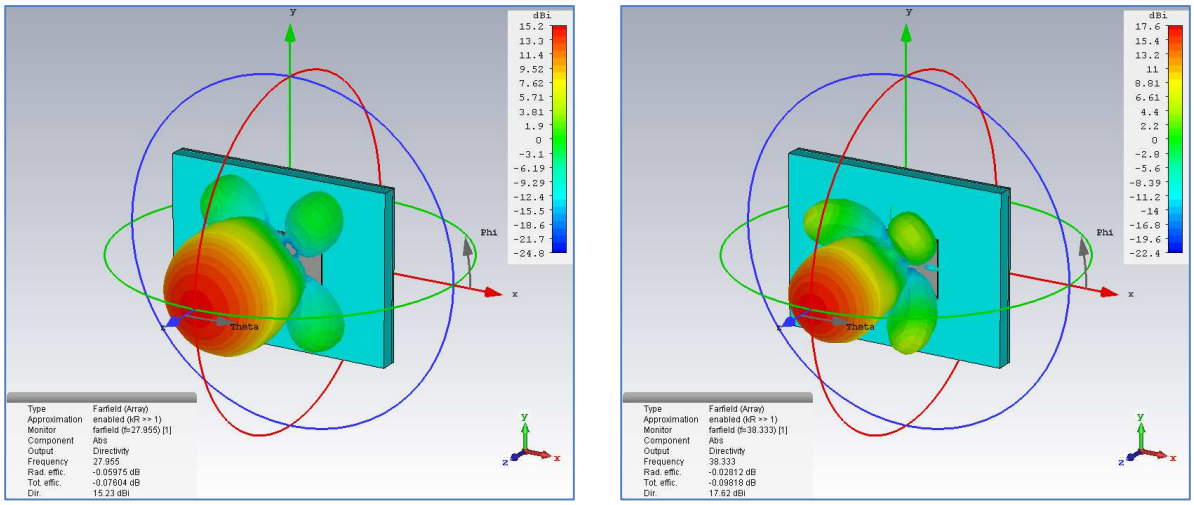

Figure D-14: Checkered Diamond 3x3 Array with 8.0 x 8.0 mm Spacing – Radiation

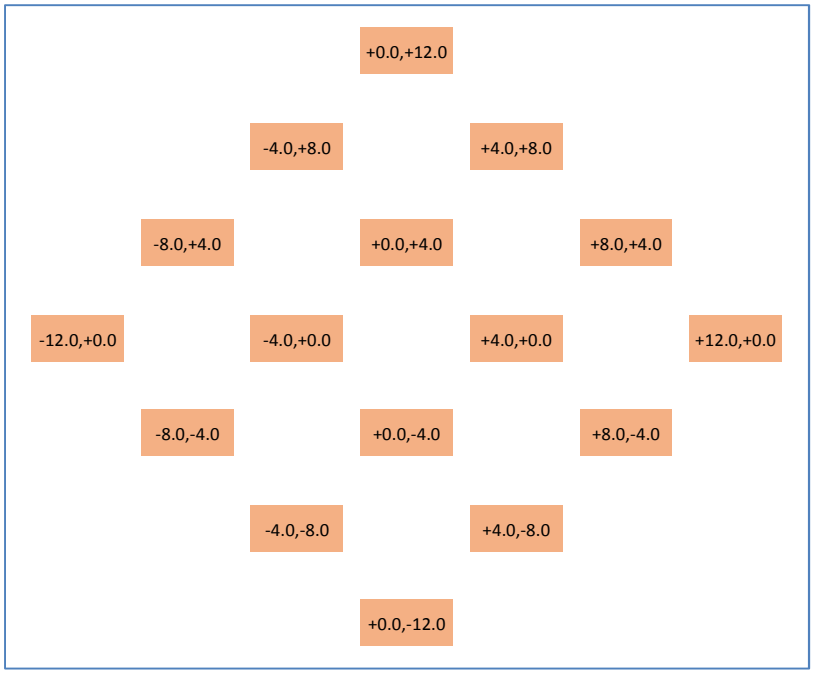

Figure D-15: Checkered Diamond 4x4 Array with 8.0 x 8.0 mm Spacing

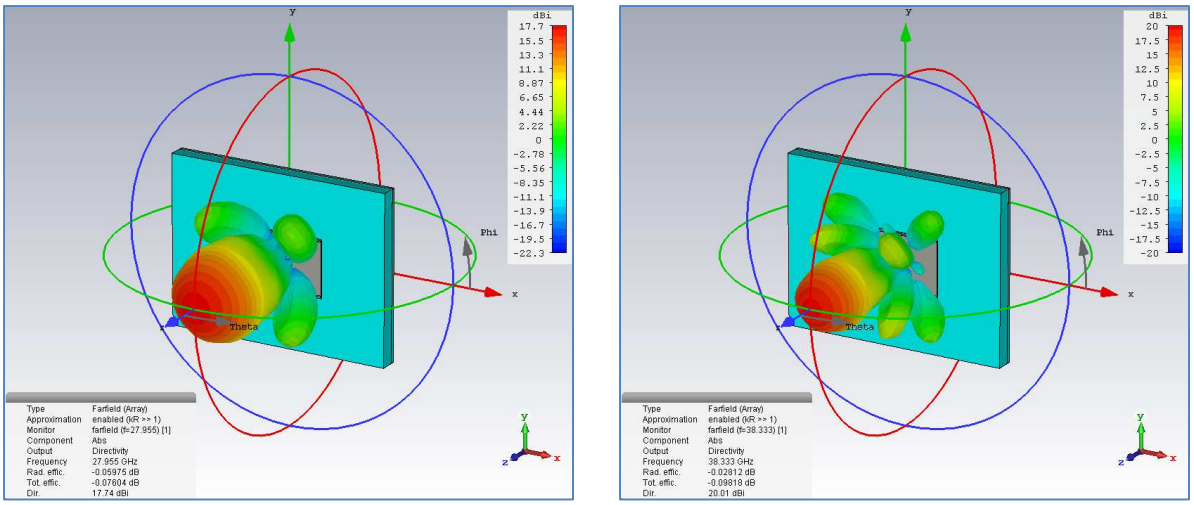

Figure D-16: Checkered Diamond 4x4 Array with 8.0 x 8.0 mm Spacing – Radiation

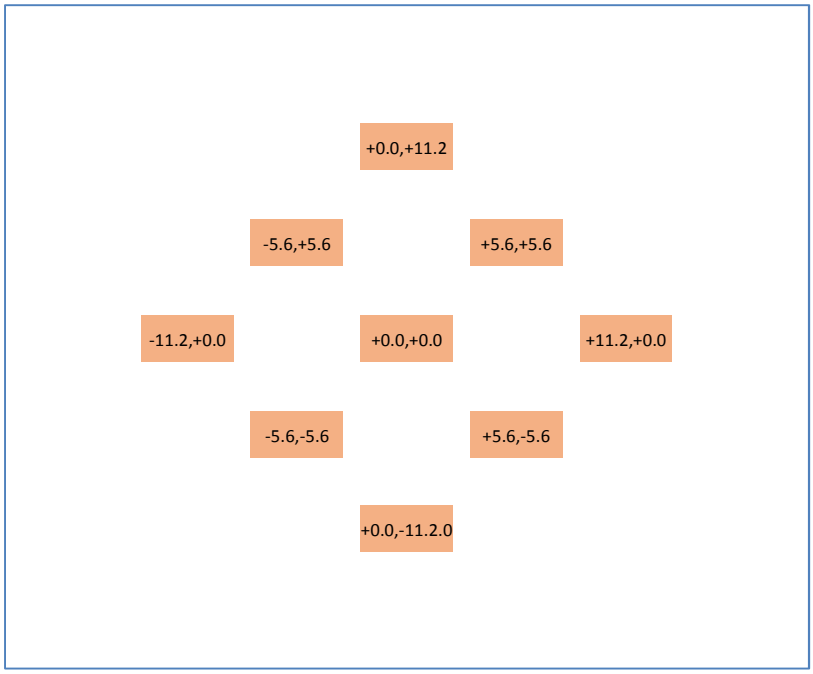

Figure D-17: Checkered Diamond 3x3 Array with 11.2 x 11.2 mm Spacing

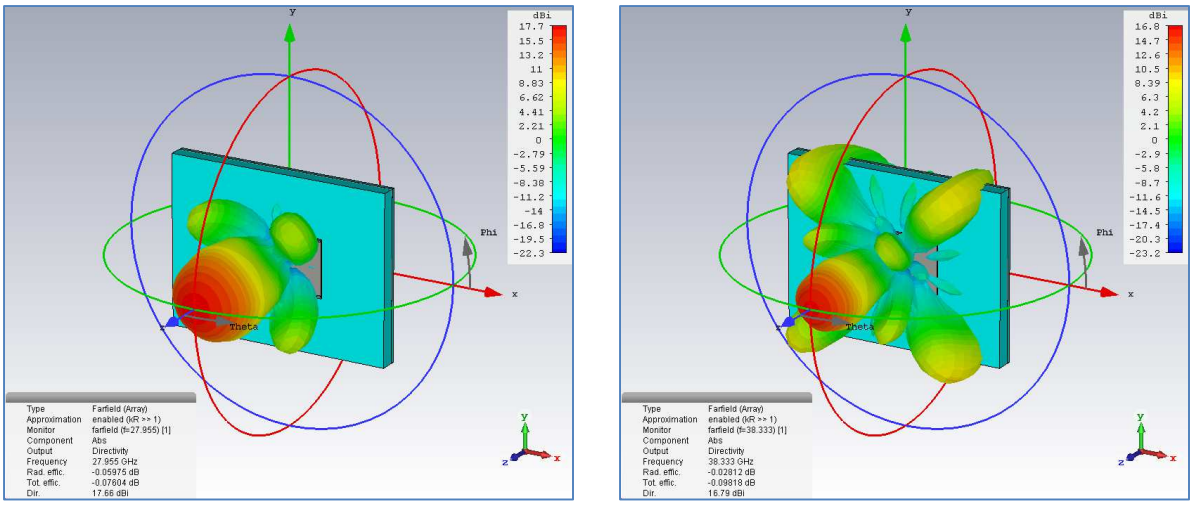

Figure D-18: Checkered Diamond 3x3 Array with 11.2 x 11.2 mm Spacing – Radiation

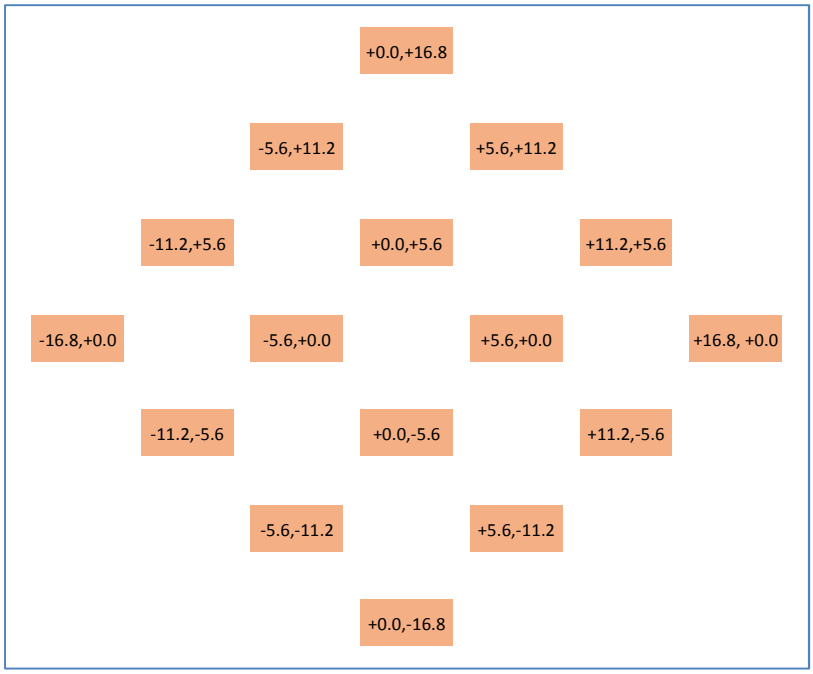

Figure D-19: Checkered Diamond 4x4 Array with 11.2 x 11.2 mm Spacing

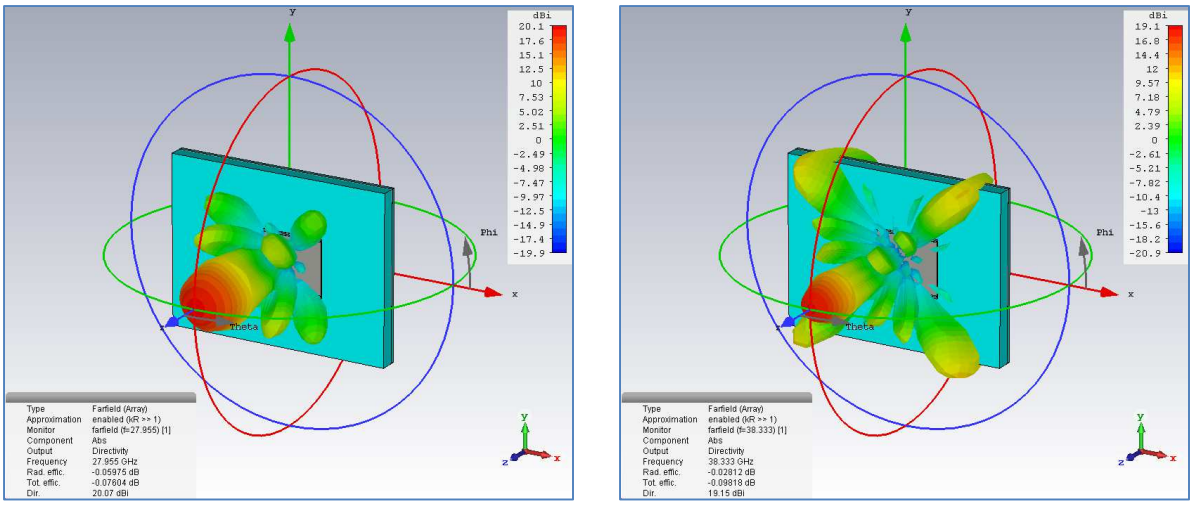

Figure D-20: Checkered Diamond 4x4 Array with 11.2 x 11.2 mm Spacing – Radiation

BIBLIOGRAPHY

[1] "Angenna Magus," Magus (Pty) Ltd, [Online]. Available: http://antennamagus.com.

[2] "NI AWR EDA Software," National Instruments, [Online]. Available: http://www.awrcorp.com.

[3] "CST - Computer Simulation Technology," Dassault Systems, [Online]. Available: http://www.cst.com.

[4] C. A. Balanis, Antenna Theory Analysis and Design, 4th ed., John Wiley & Sons, 2016.

[5] J.-F. Zurcher and F. E. Gardiol, Broadband Patch Antennas, Norwood, MA: Artech House, 1995, p. Chapter 6.

[6] J. T. Bernhard, "A Commemoration of Deschamp's and Sichak's "Microstrip Microwave Antennnas": 50 Years of Development, Divergence, and New Directions," in *Proceedings of the 2003 Antenna Applications Symposium [27th]*, Monticello, September 17-19, 2003.

[7] G. Deschamps and W. Sichak, "Microstrip Microwave Antennas," in *Proceedings of the Third Symposium of the USAF Antenna Research and Development Program*, October 18-22, 1953.

[8] R. Bancroft, Microstrip and Printed Antenna Design, 2nd ed., SciTech Publishing, 2009.

[9] J. Q. Howell, "Microstrip Antennas," *IEEE Transactions on Antennas and Propagation,* vol. 23, pp. 90-93, 1974.

[10] R. E. Munson, "Conformal Microstrip Antennas and Microstrip Phased Arrays," *IEEE Transaction on Antennas and Propagation,* vol. 22, pp. 74-78, 1974.

[11] H. Choo, A. Huntani, L. Trintinalia and H. Ling, "Shape Optimization of Broadband Microstrip Antennas Using Genetic Algorithm," *Electronic Letters,* vol. 36, no. 25, pp. 2057-2058, 7 December 2000.

[12] D. M. Pozar, "Microstrip Antenna Aperture Coupled to a Microstrip Line," *Electronic Letters,* vol. 21, no. 2, pp. 49-50, 17th January 1985.

[13] P. L. Sullivan and D. H. Schaubert, "Analysis of an Aperture Coupled Microstrip Antenna," *IEEE Transactions on Antennas and Propagation,* Vols. AP-34, pp. 997-984, August 1986.

[14] D. M. Pozar, "A Review of Aperture Coupled Microstrip Antennas: History, Operation, Development, and Applications," University of Massachusetts at Amherst, 1996.

[15] S. Maci, G. Biffi Gentili and G. Avitabile, "Single-Layer Dual Frequency Patch Antenna," *Electronic Letters,* vol. 29, no. 16, pp. 1441-1443, 5th August 1993.

[16] M. El Yazidi, M. Himdi and J. P. Daniel, "Aperture Coupled Microstrip Antenna for Dual Frequency Operation," *Electronic Letters,* vol. 29, no. 17, 19 August 1993.

[17] S. Maci, G. Biffi Gentili, P. Piazzesi and C. Salvador, "Dual-Band Slot-Loaded Patch Antenna," *IEE Proceedings - Microwaves, Antennas and Propagation,* Vols. 142, No.3, no. June, pp. 225-230, 1995.

[18] G. J. Moernaut and D. L. Orban, "Wireless Design Online," Orban Microwave, 14 July 2006. [Online]. Available: http://www.wirelessdesignonline.com.

[19] P. J. Bevelacqua, "Antenna Arrays: Performance Limits and Geometry Optimization," Tempe, 2008.

[20] "Copper-Clad Laminates & Prepreg Materials for PCBs," Isola Corp., [Online]. Available: http://www.isola-group.com.

[21] K. F. Lee and W. Chen, Advances in Microstrip and Printed Antennas, John Wiley & Sons, 1997, p. 232.

[22] C. A. Balanis, Advanced Engineering Electromagnetics, 2nd ed., John Wiley & Sons, 2012.

[23] E. O. Hammerstad, "Equations for Microstrip circuit Design," *Proc. Fifth European Microwave Conf.,* pp. 268-272, September 1975.

[24] J. P. Kim, "Optimum Design of an Aperture-Coupled Microstrip Patch Antenna," *Microwave and Optical Technology Letters,* vol. 39, no. 1, pp. 76-78, May 2003.

[25] E. J. Wilkinson, "An N-way Power Divider," *IRE Transactions on Microwave Theory and Techniques,* vol. 8, pp. 116-118, January 1960.

[26] R. Mir, *CAD Design Files for Power Divider,* Irving: Private Communication, 2017.

[27] T. Weiland, T. Martin and I. Munteanu, "A Practical Guide to 3-D Simulation," *IEEE Magazine,* December 2008.

[28] Dassault Systems, *CST Studio Suite High Training Documents Frequencey Core Module,* Irving, 2017.

[29] A. Blanchard, *EERF 6394 Antenna Engineering and Wave Propagation,* Richardson: Lecture at UTD, 2016.

[30] IPC-A-600, Acceptability of Printed Boards, H ed., Bannockburn, Illinois, 2010, p. 86.

[31] J.-P. Seppanen, *Etching Process,* Oulu: Private Communications, 2018.

[32] B. Woods, T. Sickel and K. Brand, "Derivation of a regression model based on Radial Basis Functions for the design of an aperture-coupled rectangular patch anenna," Magus Pty Ltd, Stellenbosch, South Africa.

[33] D. M. Pozar, "A Reciprocity Method of Analysis for Printed Slot and Slot-Coupled Microstrip Antennas," *IEEE Transactions,* Vols. AP-34, no. 12, pp. 1439-1446, December 1986.

[34] K. S. Kibet, "Design and Fabrication of Aperture Coupled Microstrip Patch Antennas With Arbitrarily shaped Apertures," Nairobi-Kenya, October, 2013.

BIOGRAPHICAL SKETCH

Colin Raymond Kearley was born in Schefferville, Quebec, Canada and later grew-up in small towns located in the Rocky Mountains of Western Canada. Colin entered the University of Alberta in September 1992 and graduated with a degree in Electrical Engineering in May 1996. Shortly after obtaining his B.Sc. in E.E., Colin moved to Silicon Valley to work at a start-up company focusing on the development of base stations for North American Digital Cellular. In November 1998 he joined the product development team at Nokia in Irving, Texas, where he still works today. Colin graduated from the Master Program at the University of Texas at Dallas in Spring of 2018.

CURRICULUM VITAE

Colin Raymond Kearley

email: kearleyc@yahoo.com

EDUCATION

Master of Science Degree, Major in Electrical Engineering, University of Texas at Dallas, Richardson, Texas, May 2018.

Bachelor of Science Degree, Major in Electrical Engineering, University of Alberta, Edmonton, Alberta, Canada, 1996.

PROFESSIONAL EXPERIENCE

Nokia Networks, Inc., Irving, Texas, 1998-12 to Present

Provide subject-matter expertise across the entire product development lifecycle for multi-carrier multi-modulation remote radio heads & base stations (2G/3G/4G/5G telco systems). Engaged in various roles over the years including R&D Project Manager, System Product Technical Owner, Section Manager, Delivery Capability Manager, and RF Design Engineer.